2013-12-17

Reflectance and Ultrastructure of the Retinal Nerve Fiber Layer in Normal and Glaucomatous Retinas

Ye Z. Spector
University of Miami, yezhou.sjtu@gmail.com

UNIVERSITY OF MIAMI

REFLECTANCE AND ULTRASTRUCTURE OF THE RETINAL NERVE FIBER LAYER IN NORMAL AND GLAUCOMATOUS RETINAS

By

Ye Spector

A DISSERTATION

Submitted to the Faculty
of the University of Miami
in partial fulfillment of the requirements for
the degree of Doctor of Philosophy

Coral Gables, Florida

December 2013

UNIVERSITY OF MIAMI

A dissertation submitted in partial fulfillment of
the requirements for the degree of
Doctor of Philosophy

REFLECTANCE AND ULTRASTRUCTURE OF THE RETINAL NERVE FIBER LAYER IN NORMAL AND GLAUCOMATOUS RETINAS

Ye Spector

Approved:

_____ Xiang-Run Huang, Ph.D. Research Associate Professor of Ophthalmology	_____ Weizhao Zhao, Ph.D. Associate Professor of Biomedical Engineering
_____ Fabrice Manns, Ph.D. Professor of Biomedical Engineering	_____ Jorge Bohorquez, Ph.D. Assistant Professor of Professional Practise of Biomedical Engineering
_____ Jianhua Wang, Ph.D. Associate Professor of Ophthalmology	_____ M. Brian Blake, Ph.D. Dean of the Graduate School

SPECTOR, YE (Ph.D., Biomedical Engineering)

Reflectance and Ultrastructure of the Retinal Nerve Fiber Layer in Normal and Glaucomatous Retinas. (December 2013)

Abstract of a dissertation at the University of Miami.

Dissertation supervised by Professor Xiang-Run Huang and Weizhao Zhao.
No. of pages in text. (137)

Glaucomatous damage to the RNFL usually precedes detectable visual field loss; clinical assessment of RNFL optical properties has been valuable in diagnosis of glaucoma and other neuropathic diseases. In this dissertation, we aimed to improve the understanding of the changes of RNFL reflectance and its underlying ultrastructure under the development of glaucoma.

We used simultaneous immunohistochemical labeling and both en face and in-depth confocal imaging to study axonal cytoskeletal alteration of F-actin, MTs and NFs across the retina in the context of glaucoma. We have found that alteration of each cytoskeletal components is different from each other, and different degree of RNFL change could happen in the same retina. These findings help to understand selective damage mechanisms of human glaucoma.

We proposed a new method to classify RGCs based on the content of each cytoskeletal component in axons, and investigated the cytoskeletal distribution across the retina. We have discovered axonal subtypes that contain different proportions of cytoskeletal components. This classification method provides

enhanced understanding of selective damage mechanisms in glaucoma and other ocular neuropathic diseases.

RNFL reflectance arises from light scattering by axonal ultrastructures. Structural change of axons should result in change of RNFL reflectance. We used an imaging microreflectometer (IMR) and in vitro retinas to study the reflectance of RNFL at different wavelengths, and related their changes to different degrees of glaucomatous damage. The results provide significant information for non-invasive assessment of ultrastructure or tissue diagnosis.

Currently, measurement of RNFL reflectance is limited to assess RNFL structure. This dissertation also explored a new idea to provide assessment of axonal dynamic activity by measuring the temporal change of RNFL speckle. The results provide a new concept to non-invasively detect functional change in axons, which may precede loss of axonal structure in glaucoma.

This dissertation is dedicated to my son, Oa Chilong Spector, with deepest love.

Acknowledgments

I would never have been able to finish my dissertation without the guidance of my committee members, help from coworkers, and support from my family and husband.

I would like to express my deepest gratitude to my advisor, Dr. Xiang-Run Huang, for her excellent guidance, caring, patience, and providing me with an excellent research atmosphere, with financial support. I would like to thank Dr. Weizhao Zhao and Dr. Fabrice Manns, who guided my research, considerately followed up my research progress to make sure I fulfill all the requirements to be eligible for doctoral degree, and patiently corrected my writing in the dissertation. Special thanks go to Dr. Jorge Bohorquez and Dr. Jianhua Wang for willing to participate in my defense committee and providing precious suggestions in dissertation.

I would like to thank all my lab mates. My research would not have been possible without their helps. I also would like to thank all my friends and office mates who were always there for me and willing to support me.

I also would like to thank my family in China and my in-laws. They were always supporting me and encouraging me with their best wishes.

Finally, I would like to thank my husband, Shawn Spector. He was always there supporting me, cheering me up and stood by me through the good times and bad.

TABLE OF CONTENTS

LIST OF FIGURES

Page

LIST OF TABLES

Page

Chapter 1. Introduction

1.1 Overview

Retinal nerve fiber layer (RNFL) is the innermost layer of the retina of the eye. Many neuropathic diseases damage the RNFL. Optical properties of the RNFL have been widely used in clinical diagnosis of these diseases. For instance, optical coherence tomography (OCT) and confocal scanning laser ophthalmoscopy (cSLO) detect the reflectance of RNFL to measure RNFL thickness; scanning laser polarimetry (SLP) measures RNFL birefringence, an optical property that the refractive index depends on the polarization and propagation direction of the light, to evaluate damage of the RNFL caused by glaucoma, an ocular disease which can cause permanent blindness. At the same time, microstructure of RNFL and its correlation to RNFL optical properties have been investigated in order to better understand the underlying anatomic basis of RNFL optical properties in normal retina. However, large amount of knowledge still remains unknown. For instance, there is lack of knowledge about changes of RNFL optical properties and its underlying ultrastructures under the development of glaucoma and the relationship between their changes.

Our long term goals are: (1) to provide comprehensive and quantitative understanding of the optical properties of RNFL in normal retinas and retinas with glaucomatous damage and (2) to study the anatomic origins underlying the changes, and (3) to translate this knowledge into improvement in clinical assessment of the RNFL for diagnosis of glaucoma. In this dissertation, four specific aims were proposed 1) to examine alteration of axonal actin filaments (F-

actin), microtubules (MTs) and neurofilaments (NFs), and loss of nuclei in retinas with different degrees of glaucomatous damage and study their interrelationship in the context of glaucoma (Chapter II), 2) to provide a new classification method by classifying axons according to their contents of cytoskeletal components, and study topographical distribution of classified axonal subtypes across the retina in normal rat retinas (Chapter III), 3) to study wavelength dependence of RNFL reflectance in retinas with different degrees of glaucomatous damage and investigate the relation between RNFL reflectance and its thickness at early stages of glaucomatous damage (Chapter IV), 4) to investigate dynamic change of speckle phenomenon in RNFL reflectance and explore the possibility of assessing axonal dynamic activity by measuring temporal change of the RNFL reflectance speckle (Chapter V).

In this chapter, anatomy of retinal fiber layer and retinal ganglion cell is introduced (Section 1.2), and reflectance properties of normal RNFL (Section 1.3) is presented. Following those, glaucomatous damage to the retina (Section 1.4) and RNFL reflectance in clinic diagnosis of glaucoma (Section 1.5) are reviewed, and rat models of glaucoma are described (Section 1.6). At last, the goals of our projects for this dissertation and an overview of this dissertation are presented (Section 1.7).

1.2 Retinal Nerve Fiber Layer and Retinal Ganglion Cells

The retina lies at the back of the eye [4], and appears nearly transparent in human. Retina is a layered structure, including inner limiting membrane (ILM), retinal nerve fiber layer (RNFL), retinal ganglion cell layer (RGCL), inner

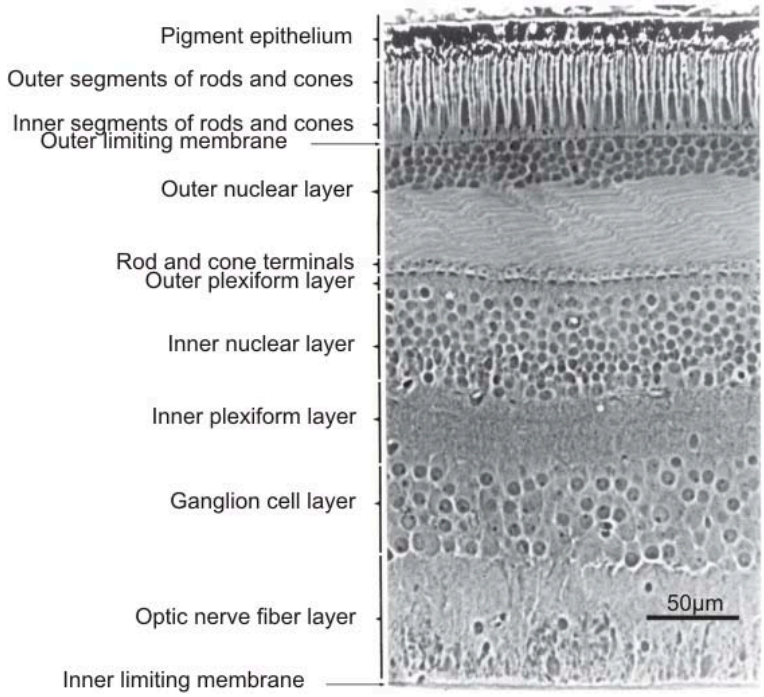

Figure 1.1. Light micrograph of the vertical section through human retina. Reprint from publication: J E Dowling. *Retina, an overview*, 2009 Elsevier Ltd. (Figure 1)

plexiform layer, inner nuclear layer, out plexiform layer, out nuclear layer, external limiting membrane, photoreceptor layer (rods and cones) and retinal pigment epithelium (Figure 1.1). These layers connect to each other via synaptic connection.They work together to detect and convert outside light signals to electric pulses and transmit these pulses via the optic nerve to the brain. At the same time, each layer also absorbs, reflects and scatters light, when viewed from optical perspective. This provides optical techniques access to detect and measure optical properties of damaged structures.

Retinal ganglion cells (RGCs) are the neurons located in the RGCL which is just under the RNFL [5]. They process visual information from photoreceptors and convey them to visual cortex. A RGC is composed of a cell body, highly branched dendrites and an axon, either myelinated or unmyelinated. Axons in human retinas are unmyelinated. Axons are long, membrane-enclosed processes that contain three major cytoskeletal components include F-actin, MTs, and NFs.

In human and rodent retinas, the RNFL, which underlies the retinal surface, consists of unmyelinated axons of retinal ganglion cells. Axons are grouped into bundles which converge into optical nerve head (ONH). The RNFL is thick near the ONH and gets thinner toward the peripheral retina region.

1.3 Reflectance Properties of Normal RNFL

Optically the RNFL is a highly reflective layer [6,7]. Figure 1.2 shows a reflectance image of RNFL with highly reflective bundles and dark blood vessels. RNFL reflectance in normal retinas has the following characteristics:

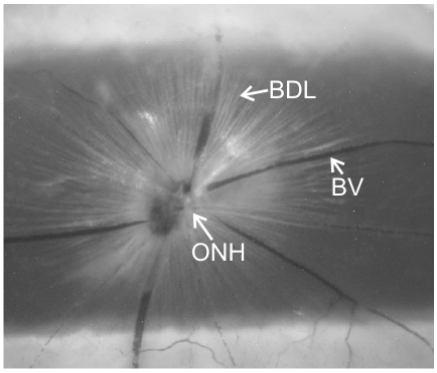

Figure 1.2. Reflectance image of RNFL. Retinal nerve fiber bundles appear as bright stripes against a dark background. Wavelength: 440nm; Image Size: 2.15mm ×2.38mm. BDL: retinal nerve fiber bundles; BV: blood vessel; ONH: optical nerve head.

(1) RNFL reflectance is very directional [7]. The reflectance of a nerve fiber bundle is confined in a conical sheet concentric with the bundle axis. The directionality suggests that RNFL reflectance arises from light-scattering by the cylindrical structures of axons [8].

(2) RNFL reflectance is proportional to its thickness [3]. Proportionality implies that the reflected light arises from the entire volume of a nerve fiber bundle.

(3) RNFL reflectance declines with increasing wavelength. Wavelength dependence implies that different scattering mechanisms underlie RNFL reflectance at different wavelengths [9].

(4) It has been confirmed that MTs are one of the contributors to the RNFL reflectance, yet other scattering components are not clear [10,11] (Fortune et al IOVS 2008;49:ARVO E-Abstract 3761).

Many ocular neuropathic diseases cause damage of the RNFL [12-14] and, hence, change the optical properties of the RNFL. Several optical methods have been developed to aid clinical diagnosis of these diseases by measuring RNFL reflectance [15-17]. To provide quantitative and objective assessment of RNFL by optical methods, the optical properties of RNFL need to be well understood under the condition of ocular diseases.

1.4 Glaucomatous Damage to the Retina

Glaucoma is defined as a group of ocular disorder with multi-factorial etiology united by a clinically characteristic intraocular pressure-associated optic

neuropathy [18]. It is an irreversible process that leads to permanent vision loss if it is not treated.

High intraocular pressure (IOP) is a major risk factor in glaucoma. IOP increases generally due to a decrease in outflow of aqueous humor (AH) which usually circulates into the anterior chamber and exits through trabecular meshwork (TM) into the Schlemm's canal and get into systemic circulation [19]. Increase of IOP results in damage to the optic nerve and axons.

Glaucomatous damage features progressive optic neuropathy with characteristic optic disc (or optical nerve head) and nerve fiber layer damage. Quantification of the size of the cup and its relationship to the size of the optic disc, i.e. the cup/ disc ratio (CDR), examination of the RNFL's diffuse atrophy and evaluation of thinning of the RNFL have been broadly used to differentiate glaucomatous from normal eyes [20-22]. The changes occurring in the structural appearance of the RNFL and ONH usually precede the development of visual field loss [22]. Studies have also demonstrated changes in the axonal cytoskeleton and loss of RGCs in glaucoma [12-14,23-28].

Axonal transport abnormality also has been reported related to glaucomatous optic nerve injury in many studies [29-32] .Reduced or obstructed retrograde and anterograde axonal transports have been demonstrated in experimental glaucoma [29-32]. These reduced or obstructed axonal transports are suspected to be related to neurotrophin deprivation in the pathogenesis of RGC death, or neuroprotective mechanism in glaucoma.

The ONH has been proposed as the pivotal site of RGC injury after elevation of IOP, and be responsible for axonal transport disruption, axonal cytoskeleton damage and axonal regeneration failure[33].

1.5 RNFL Reflectance in Clinic Diagnosis of Glaucoma

Damage of RNFL is usually irreversible; it is therefore important to detect early structural change and thus prevent further deterioration. Several optical techniques have been developed to assess the RNFL by measuring the optical properties of the RNFL. Among them, OCT is the most widely used non-invasive optical technique in clinical diagnosis of glaucoma. It uses near-infrared light to provide direct cross-sectional measurement of the RNFL. In OCT system, an incident light beam is split into two arms, a sample arm and a reference arm. The reflected light from both arms then is combined to form interference pattern. As the sample arm scans through the depth of a tissue, a reflectance profile provides depth information, which is used to derive RNFL thickness. Similarly, cSLO measures the reflectance of RNFL and derives RNFL thickness by scanning the retina point by point by a focused laser beam and catching the reflected light through a small aperture. The small aperture eliminates light scattered from outside the focal plane resulting in a high contrast image of the retina. In-depth reflectance profile provides measurement of RNFL thickness.

In summary, current optical methods measure RNFL reflectance to derive its thickness, which has been widely used in clinical practice and provide objective diagnosis and monitoring of glaucoma.

1.6 Rat Model of Glaucoma

Several animal models have been used to study glaucoma, including monkeys, rodents and other species. Glaucoma could be either induced or spontaneous. Since high IOP is major risk factor for glaucoma, increasing IOP is most often used to produce animal models of glaucoma.

A good animal model of glaucoma is critical for our research studies. It should closely reproduce human disease, and increased IOP should be sustained. In addition, low cost should be taken into consideration that sufficient animals can be used for statistics.

Among these animal models, we have chosen a rat model because of its lower cost and other advantages comparing to other species. For example, monkey are the perfect model for studying glaucoma due to its almost identical retinal and optical nerve anatomy, but they are very expensive and hard to handle. Rats, however, have similar anatomical[34,35] and developmental[36,37] characteristics of the anterior chamber, especially in the aqueous ourflow pathway, with human. They are much easier to maintain in the laboratory and can be used in large numbers[38]. Hence, rats have been widely used in vision research.

In order to increase IOP in rats, there are several choices. For example, intraocular injection of viscoelastic substances could block the trabecular meshwork and result in increased IOP. This method can easily induce high IOP, but the disadvantage is that it has short lasting effect, and IOP spikes. There is another approach of injecting hypertonic saline solution in the episcleral veins to

modify the post-trabecular anatomy. This approach introduces no inflammation, but it needs repeated injections to maintain high IOP and high variability between rats was reported. TM laser photocoagulation is the approach used in our study. The mechanism of this method is that reduction of AH outflow by a transient network of cells and debris as well as disorganization of the TM architecture have been indicated as the cause of increased IOP [39-41]. It has the advantage that blocking of AH outflow occurs in the TM as in humans. But repeated laser treatments to maintain high IOP are required, and it is also possible to have hyphema and corneal opacities. In our study, we have avoided using retinas with hyphema, and we use ointment to keep cornea moisture after laser treatment.

1.7 Goals and Overview of this Dissertation

As mentioned above, RNFL is formed by axons of RGCs and the axons consist of three major cytoskeletal components, F-actin, MTs and NFs. Glaucoma cause damage of axonal cytoskeletons. Changes in the axonal cytoskeleton and loss of retinal ganglion cells (RGCs) are known to occur in retinas with optic nerve injury. Previous reports, however, were limited to study damage mechanisms of one or two cytoskeleton components and often the studies were focused on the cytostructure within the ONH [12,23,27,28]. One of the goals of this dissertation was to provide a comprehensive understanding of axonal cytoskeleton alteration of all three cytoskeletal components in retinas with different degrees of glaucomatous damage, and study their interrelationship in the context of glaucoma. Simultaneous immunohistochemical staining of F-acin,

MTs and NFs were used to study topographic change of the cytoskeleton in the RNFL and structural change patterns around the ONH.

Due to the diversity of ganglion cell properties, RGCs are often classified into different subtypes based on their morphology or functional characteristics (will be discussed in Chapter 3). However, there is little knowledge about organization and variation of the ultrastructures in axons. We have found that axons may or may not contain all three cytoskeletal components; hence axons might be classified into subtypes based on the contents of cytoskeletal components. Another goal of this dissertation was to provide a new classification method by classifying axons according to their contents of cytoskeletal components. Topographical distribution of classified axonal subtypes across the retina was studied in normal rat retinas.

Glaucoma causes damage of the RNFL. RNFL reflectance arises from light scattering by the ultrastructure in axons and is wavelength dependent. Direct assessment of the RNFL was often used in clinical diagnosis of glaucoma. However, some optical methods used in diagnosis of glaucoma such as OCT are not able to detect some subtle RNFL defects [42-47]. One assumption is that RNFL reflectance measured at the wavelength (830 nm) used in OCT is not sensitive to early glaucomatous damage. The third goal of this dissertation was to study wavelength dependence of RNFL reflectance in retinas with different degrees of glaucomatous damage and investigate the relation between RNFL reflectance and its thickness at early stages of glaucomatous damage. Gained

knowledge may improve current optical methods to detect early glaucomatous damage.

Speckle is an interference phenomenon of coherent light scattered by particles in a medium [48,49]. Speckled textures are often observed in biological tissues because they are filled with scattering particles. With high contrast and resolution imaging, RNFL reflectance shows speckle patterns [9]. The axons of retinal ganglion cells are dynamic structures responsible for axonal transport. It is plausible that dynamic activity of axons causes change of RNFL reflectance. One project in this dissertation aimed to investigate dynamic change of speckle phenomenon in RNFL reflectance and explore the possibility of assessing axonal dynamic activity by measuring temporal change of the RNFL reflectance speckle.

The dissertation is structured as follows. Chapter 2 presents the studies of axonal cytoskeleton in glaucomatous retinas, Chapter 3 introduces the classification of axonal subtypes based on cytoskeletal components, Chapter 4 describes RNFL reflectance and spectrum change in glaucomatous retinas, Chapter 5 demonstrates that the reflectance speckle of RNFL reveals axonal activity, and Chapter 6 discusses the significance of these works. The future work is also proposed in Chapter 6.

1.8 Significance

Glaucoma causes irreversible damage on retina. It is important to detect early change of glaucoma to prevent permanent vision loss.

Currently, knowledge about the changes of RNFL reflectance and its underlying ultrastructure under the development of glaucoma is limited. The

study of cytoskletal distortion and RGCs classification will provide enhanced understanding of the damage mechanisms in glaucoma. RNFL thickness derived from RNFL reflectance measured at infra-red wavelength is commonly used in clinical diagnosis of glaucoma. Studying RNFL reflectance spectra in glaucomatous retina will have significant impact on improvement of early and sensitive detection of glaucomatous damage in clinical practice. Furthermore, relating the change of RNFL reflectance and glaucomatous damage should help to develop non-invasive assessment of ultrastructure or tissue diagnosis.

Currently, measurement of RNFL reflectance is limited to assess RNFL structure. The study of temporal change of RNFL speckle may provide assessment of axonal function.

Chapter 2. Axonal Cytoskeleton in Normal and Glaucomatous Retinas

2.1 Background

2.1.1 Axons of Retinal Ganglion Cells and Cytoskeleton

RGCs are neurons located in the retina ganglion cell layer. The structure of a typical neuron is showed in Figure 2. 1 [50]. The soma is the cell body with a large nucleus and other cytoplasmic components. The dendrites are highly branched cellular extensions from the soma. The axon, also called nerve fiber, is a very long projection with axon terminal at the end. Axons ensure conduction of

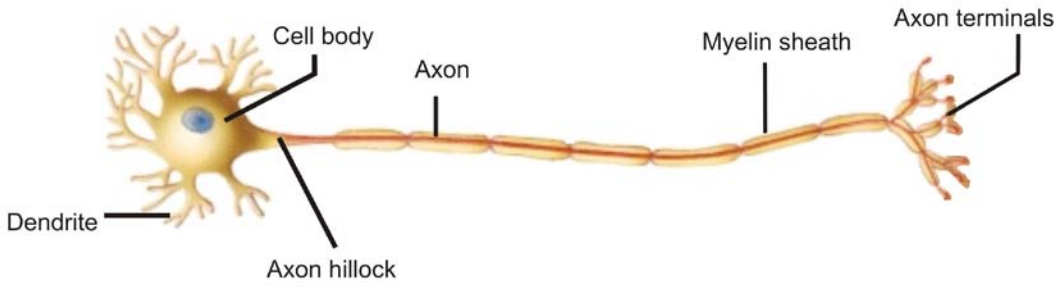

Figure 2.1. Structure of a typical neuron. From Molecular Cell Biology. 4th edition: Figure 21-1.

information from cell body to nerve terminals. Axons may or may not be myelinated with myelin sheath while axons in human and rat retinas are unmyelinated.

The diameter of axons in rat retinas ranges from 0.12 to 2 microns with peak around 0.4 microns [51]. The cytoplasms of axons are filled with cytoskeleton, which helps maintain cell shape, produce locomotion, provide mechanical strength and facilitate the intracellular transport of organelles[52]. The major cytoskeletal components include actin filaments (F-actin), microtubules (MTs), and neurofilaments (NFs) [53]. These components,

individually, and in association with each other, play an important role in axonal function and architecture. F-actin, about 8 nm in diameter and a major component maintaining cytoarchitecture, is assembled into two general types, bundles and networks [54,55]. Bundled F-actin in axons is concentrated in the region of and runs parallel to MTs. It provides a substrate for MT transport and affects the structural organization of MTs [56-58]. MTs are straight, hollow cylinders which have an outer-diameter of about 25 nm. Most MTs activity is involved in motion, provided by protein motors that use energy from ATP to move along the MTs [56]. NFs, about 10 nm in diameter, are the major determinants of the diameters of axons and provide a structural framework in the cell [23,59].

2.1.2 Change of Axonal Cytoskeleton in Glaucoma

Many studies have demonstrated changes in axonal cytoskeleton in glaucoma and other optic nerve diseases. Loss of NFs, the most frequently studied component, is evident as shown in various animal models of optic nerve diseases [12-14,23-25]. A recent study has found both degenerative changes and aberrant growth of NFs in a mouse glaucoma model [26]. Changes in MTs and MT-associated proteins are observed in the RNFL and at the optic nerve head (ONH), with elevation of IOP. Alteration of F-actin distribution often appears in a fan-shaped region and occurs first in the dorsal retina with a rat model of glaucoma [28]. Studies also show that structural change precedes axonal functional and macroscopic change. Balaratnasingam et al. have demonstrated that a change in NF distribution at the optic nerve precedes axonal transport alteration during acute IOP elevation[14]. Fortune et al. have shown that loss of MTs, as assessed by RNFL birefringence, precedes measurable RNFL thinning

after onset of experimental glaucoma (IOVS 2008;49: ARVO E-Abstract 3761). We have recently suggested that RNFL reflectance, which arises from light scattering by the axonal cytostructure, changes before the decrease in RNFL thickness (will be discussed in Chapter 4) (Huang X-R, et al. IOVS 2010;51: ARVO E-Abstract 4808).

2.2 Purpose and Hypothesis

Previous studies by others and us have provided an insightful view of the changes in the axonal cytoskeleton and loss of RGCs. However, they often are limited to studying changes of one or two cytoskeleton components in glaucoma. Glaucoma causes selective damage of the nerve fiber bundles [12-14,24-26,28]. It is, therefore, reasonable to assume that different cytoskeletal components respond differently to elevated IOP. To better understand axonal cytoskeleton alteration in retinas with glaucomatous damage, all three axonal cytoskeletons alteration should be investigated simultaneously.

In this study, our goal was to examine alteration of axonal F-actin, MTs and NFs, and loss of nuclei in retinas with different degrees of glaucomatous damage and study their interrelationship in the context of glaucoma. With this study, we expected to provide a comprehensive understanding of axonal cytoskeletons alteration in retinas with elevated IOP and seek early signs of cytostructural change before loss of RGCs.

2.3 Experimental Materials and Methods

2.3.1 Rat Model of Glaucoma

Female Wistar rats with weight from 250 to 350 g were used. Animals were housed under a 12-hour light–12-hour dark cycle, with standard food and water provided ad libitum. Animals were anesthetized with intraperitoneal ketamine (50 mg/kg) and xylazine (5 mg/kg) and topical proparacaine 1% eye drops. Experimental glaucoma was then induced by translimbal laser photocoagulation of the trabecular meshwork[60] after rats fell into deep sleep. The laser treatment (a diode laser with wavelength of 532 nm, 500-mW power, 0.6-second duration, 50 μm-diameter spot size) was implemented in the left eye of each rat and the contralateral eye was kept untreated serving as control eye. Around 55 to 60 trabecular burns were evenly distributed. A second treatment after a week was applied to those eyes that did not maintain elevated IOP.

We used a rebound tonometer (Tonolab; Tonolab, Espoo, Finland) to monitor the IOP after the animals were deeply anesthetized. The tonometer was held perpendicular to the center of the cornea and ten valid measurements were obtained in both eyes. The mean value of each ten measurements was considered as the IOP of the eye. The IOP in both eyes was measured just before treatment and 1, 3, 5, and 7 days after treatment and then once a week until enucleation or the IOP returned to its baseline level. For each rat, graphs of IOP (IOP in mm Hg versus days after treatment) for treated and fellow eyes were constructed. Cumulative IOP (cIOP), the area between the two curves in units of mm Hg-days, was calculated.

All experiments adhere to the ARVO Statement for the Use of Animals in Ophthalmic and Vision Research. The protocol for the use of animals is approved by the Animal Care and Use Committee of the University of Miami.

2.3.2 Tissue Preparation and Immunohistochemistry

After the treated eyes were exposed to elevated IOP for a certain period (at least 2 weeks), both eyes of each animal were removed and prepared for immunohistochemical study. Tissue preparation followed previously developed procedures [9,11]. Briefly, the animal was euthanatized right after both eyes of an anesthetized animal were removed. For each eye, an eye cup of 5 mm diameter with around 1mm optic nerve attached was excised and placed in a dish of warm (33–35°C) oxygenated physiologic solution. After it was dissected from the retinal pigment epithelium and choroid, the retina was placed on a membrane with the photoreceptor side against the membrane, fixed in 4% paraformaldehyde for 30 minutes at room temperature, and rinsed thoroughly in phosphate-buffered saline (PBS). The tissue was then removed from the membrane for further immunohistochemical staining with optical nerve removed.

Orientation of retinas was documented by first marking the caudal side of the eye in situ with a skin marker and then, after dissection, cutting a notch into the eye cup and retinal edge at the marked position.

The cytoskeleton components of axons were studied by simultaneously labeling a whole-mounted retina with phalloidin to stain F-actin, anti-β-tubulin monoclonal antibody to mark the MTs, and anti-neurofilament antibody to label the NFs. The nuclei in the inner retina were also identified by 4′,6-diamidino-2-phenylindole (DAPI) fluorescent counterstain. The tissue was permeabilized in

PBS containing 0.8% TritonX-100 for 1 hour followed by incubation in blocking serum (5% goat serum and 0.8% TritonX-100) for 1 hour at room temperature. The tissue was transferred into a primary antibody solution (1:500, rabbit anti-neurofilament 200 kDa Sigma) and incubated at room temperature for 2 hours then at 4°C for overnight. After the tissue was washed in PBS (three changes of 10 minutes each), it was incubated in a mixed solution of the secondary antibody (1:250, AlexaFluor 647 goat anti-rabbit IgG; Invitrogen, Carlsbad, CA) and anti-β-tubulin antibody (1:100, Cy3 conjugated; Sigma-Aldrich, St. Louis, MO) for 4 hours at room temperature. After it was washed again in PBS, the tissue was transferred into a solution of phalloidin (1:100, AlexaFluor 488 phalloidin; Invitrogen) for 1 hour at room temperature. After a rinse in PBS, it was incubated in DAPI (FluoroPure grade; Invitrogen- Molecular Probes, Eugene, OR) for 30 minutes in subdued lighting. The stained retina was rinsed again and mounted on a glass slide with an antifade mounting medium (Vectashield; Vector Laboratories, Inc., Burlingame, CA). The retina was stored at 4°C for confocal microscopy imaging.

2.3.3 Confocal Laser Scanning Imaging

A confocal laser scanning microscope (Leica TCS SP5, Leica Microsystems, Bannockburn, IL) was used to provide en face images of whole-mounted fluorescently stained retinas. A 40x oil objective provided en face images of the tissue with a full field of view of 386 μm × 386 μm and a resolution limited to the sampling density of 0.76 μm/pixel. To cover all bundles merging into the ONH, at least a 3 × 3 tiled array of images was taken that covered a retinal area of 1.16 mm × 1.16 mm with the ONH at the center. For each array position, en face

images were collected at evenly spaced positions in depth (1 μm apart in tissue) starting from the RNFL surface through the retina to a depth at least including the ganglion cell layer. The retina was then reconstructed in 3-D, and cross sectional (CS) images were synthesized from the reconstruction with customized software. The depth of an en face image was defined as the distance between this image and an image with the first recognizable RNFL located at the image center. The depth of individual bundles could vary across an image due to tilt of the tissue. To view cytoskeleton detail in regions of interest, we also collected images with a 63x oil objective with a full field of view of 246 μm x 246 μm and a resolution limited to the sampling density of 0.24 μm/pixel. If not otherwise stated, images displayed and used for data analysis in this chapter were taken with the 40x oil objective.

The tissue was scanned sequentially by separate scanning lasers with wavelengths of 405nm, 488nm, 543nm and 643nm. Four detectors were used to detect the emission light from excited sample. The detection pinhole which eliminates out-of-focus light was set to default value 61.0 μm for 40x objective and 95.6 μm for 63x objective. Note that the pinholes were set to approximately the size of one airy to insure a balance between the signal-to-noise ratio and sectional thickness. The size of the Airy diffraction is determined by the resolving power of an objective. The diameter of the Airy disc for the Leica Confocal System is given by $d_{Airy} = 1.22 * \lambda_{exc} * M * 3.6 / NA_{obj}$ with λ_{exc} as the mean value of excitation wavelengths of the four channels, M as the magnification factor and NA_{obj} as numerical aperture (NA) of the objective lens. The NA is 1.25 and 1.4

for 40x objective and 63x objective, respectively. Lateral resolution for a pinhole set to near 1 airy can be calculated by following formulae, which represents the Rayleigh criterion: $r_{lateral} = 0.51 * \lambda_{exc} / NA_{obj}$, where n is the refractive index of the immersion medium [61]. For example, in theory the optical lateral resolution for a 488-nm excitation light is 0.199 μm when using a 40x oil objective lens, and 0.178 μm when using a 63x oil objective lens. Axial resolution of a Confocal System can be calculated by $r_{axial} = 0.88 \frac{\lambda_{exc}}{n - \sqrt{n^2 - NA_{obj}{}^2}}$. The optical axial resolution for a 488-nm excitation light is 0.648 μm with a 40x oil objective lens, and 0.455 μm with a 63x oil objective lens. Decreasing the diameter of the pinhole increases axial resolution.

In the experiments, the sampling size was set to 512 x 512 pixels for 40x objective and 1024 x 1024 pixels for 63x objective to fulfill Nyquist criterion, which leads to a lateral to 0.76 μm for a 40x objective, and 0.24 μm for a 63x objective in en face images. The scan speed was 400 Hz. The detector gain was adjusted for each channel to display nerve fiber bundles at approximately full dynamic range without inducing spectral bleed-through between channels. The offset of all channels were set to zero to keep low intensity information.

2.3.4 Quantitative Analysis of RNFL Texture

In our early study of F-actin distribution in glaucomatous retinas the texture of the fluorescence labeled F-actin had been observed to be altered by elevation of IOP[28]. Currently there was no method to objectively and quantitatively describe the appearance of cytoskeletal distribution in the RNFL. In this study,

we developed a quantitative method to study the texture of axonal cytoskeleton within the RNFL. The method was based on statistical properties of the intensity histogram[62,63].

Let Z be a variable indicating intensity in a region, p(Z) the histogram of the intensity levels within the region, and L the number of possible intensity levels, then $U = \sum_{l=0}^{L-1} p^2(Z_l)$ is a measure of the uniformity of intensity in the region. If the intensity in a region has variance σ^2, $R = 1 - 1/(1+\sigma^2)$ measures the relative smoothness of the intensity. The higher *U* value indicates better uniformity while the lower *R* value represents better smoothness. Thus, in regions with constant intensity, *U* is the maximum value, and *R* is 0. In this study, *U* and *R* were used to quantify the cytoskeleton structural distortion at early stages of glaucomatous damage.

2.3.5 Selection of Bundles for Texture Analysis

For each retina, a circle with radius of 300 μm was defined in en face image centered at ONH. CS image of the RNFL was obtained along the circle from reconstructed 3-D images of the retina (Figure 2.2). To analyze texture of cytoskeleton within each bundle, rectangular boxes were defined on the cross section of the nerve fiber bundles (Figure 2.2B). Boxes were located two to three pixels below the RNFL surface to avoid stain artifacts on the tissue surface that occasionally occurred, especially in the NF images.

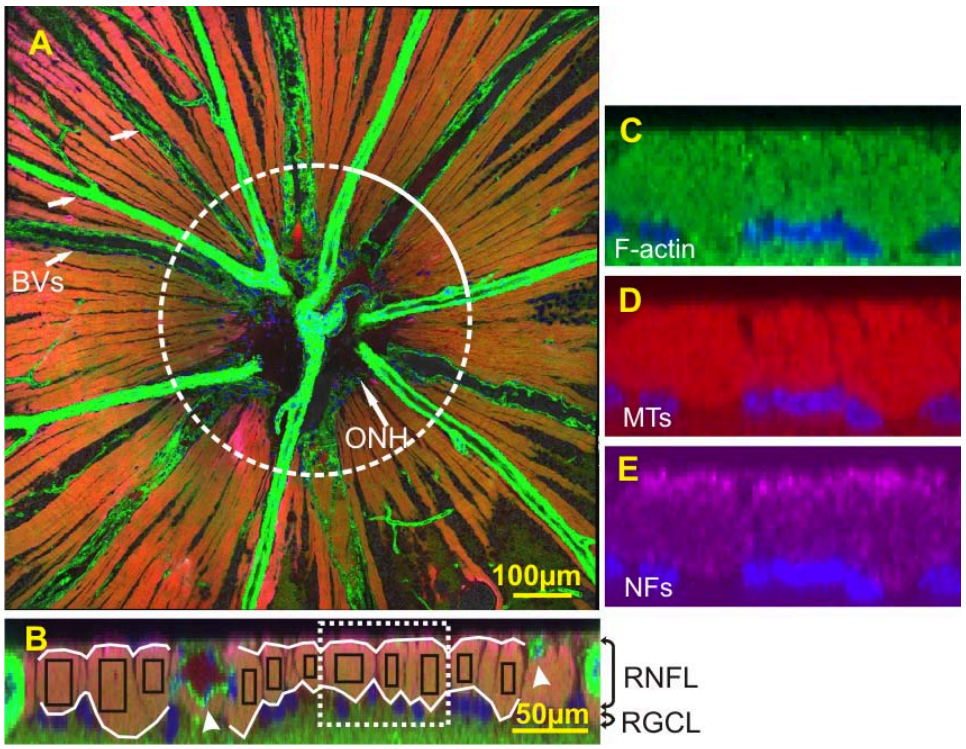

Figure 2.2 En face and cross sectional image of a normal retina with F-actin, MTs, NFs and nuclei stained. (A) en face image of a whole mounted retina by merging fluoresecence stained F-actin, MTs, and NFs. (B) cross sectional image obtained along solid line in (A). Nuclei stained as blue. Image scale: length-depth ratio = 1: 2.25 (C-E) Magnified view of region outlined with dashed lines in (B). BVs: blood vessels; ONH: optical nerve head; RNFL: retinal nerve fiber layer; RGCL: retinal ganglion cell layer.

To calculate the thickness of each bundle and the average thickness of selected RNFL sectors, upper and lower boundaries of the RNFL were manually defined. The upper boundary was defined by drawing a curve embracing intensely stained F-actin on the surface of the retina; the lower boundary was defined by a curve embracing intensely stained F-actin just above the single layer of RGC. The boundaries excluded large blood vessels identified by strong phalloidin staining. Bundles were selected by drawing boxes within the RNFL. The thickness of each selected bundle was determined as the area between upper and lower boundaries divided by box width (Figure 2.2B). The average

thickness of selected RNFL sector was calculated as average thickness of all the bundles in this sector. For normal retinas, the mean and range of RNFL thicknesses were then determined. For treated retinas, to be comparable with the normal RNFL, only the RNFL sectors whose average RNFL thickness was within the range of the normal thickness, were selected and used in texture analysis. Bundles with capillaries, identified by strong phalloidin staining, were not selected. The texture parameters and were calculated for each defined box.

For each normal retina, 11 to 13 bundles approximately evenly distributed around the ONH were selected along the circle. In the treated retinas, any bundle with a thickness within the normal range was identified. There were six treated retinas with seven to nine selected bundles for texture analysis. Other four retinas had at least 12 bundles identified, and eight bundles were randomly chosen. The average of selected bundles for each retina was used for data and statistical analysis.

2.3.6 Quantification of Nucleus Density

During our preliminary study of change of cytoskeleton in glaucomatous retina, we found that nuclei often appeared in the RNFL in glaucomatous retinas, which is unusual in normal retinas. Thus, we developed a method to analyze and quantify the nucleus density in normal and glaucomatous retinas.

Nucleus density was studied in RNFL sectors where texture was analyzed. The densities were calculated for the RNFL and the retinal ganglion cell layer (RGCL) which lies just below the RNFL (Figure 2.2B). The numbers of nuclei in the RNFL and RGCL, respectively, were manually counted and the horizontal length of the RNFL sectors was measured. (Figure 2.2B) Linear density of nuclei

(nuclei per mm) in each layer was then calculated as the ratio of the number of nuclei and the sector length. Total linear density in both layers was also calculated.

2.3.7 Statistical Analysis

The statistical analysis of bundle thickness, texture parameters, and nuclear density between normal retinas and glaucomatous retinas were studied by using an analysis of variance approach (two-way unbalanced ANOVA). The significance level was set at $P < 0.05$. Statistical tests were performed in commercial software (MatLab Statistics Toolbox; Matlab Version 2009b; The MathWorks, Inc., Natick, MA). Image reconstruction and data analysis were implemented with customized programs written in the software.

2.4 Results

2.4.1 IOP of Treated Retinas

Ten Wistar rats were used in this study to examine axonal cytoskeleton in normal and glaucomatous retinas. The baseline IOP before treatment was not significantly different, with 10.2 ± 0.6 and 10.0 ± 0.6 mmHg for control and treated eyes, respectively. The IOP of all treated eyes remained elevated for at least 2 weeks. Table 2.1 summarizes the IOP of treated eyes and the duration of animal survival after the first laser treatment.

Table 2.1. Summary of the Treated Retinas

Rat	IOPbaseline (mmHg)	cIOP (mmHg-days)	IOPpeak (mmHg)	Duration (wk)
1	10	68	40	2.5
2	10	76	39	3.5
3	10	97	31	2.5
4	9	110	42	3
5	9	117	33	3
6	10	120	46	3
7	10	121	43	3.5
8	11	142	38	3
9	11	201	54	2
10	10	261	52	3
Mean ± SD	10.0 ± 0.6	131 ± 59	42 ± 7	3.0 ± 0.3

cIOP: cumulative IOP

2.4.2 Nerve Fiber Bundles and Axonal Cytoskeleton in Normal Retinas

In normal retinas, retinal nerve fiber bundles were identified as bright stripes in en face images by fluorescence-labeled F-actin, MTs, and NFs (Figures 2.3A–C). Each labeled structure demonstrated tightly packed axonal bundles that converged into the ONH. With the 40x objective the stain of each cytoskeleton

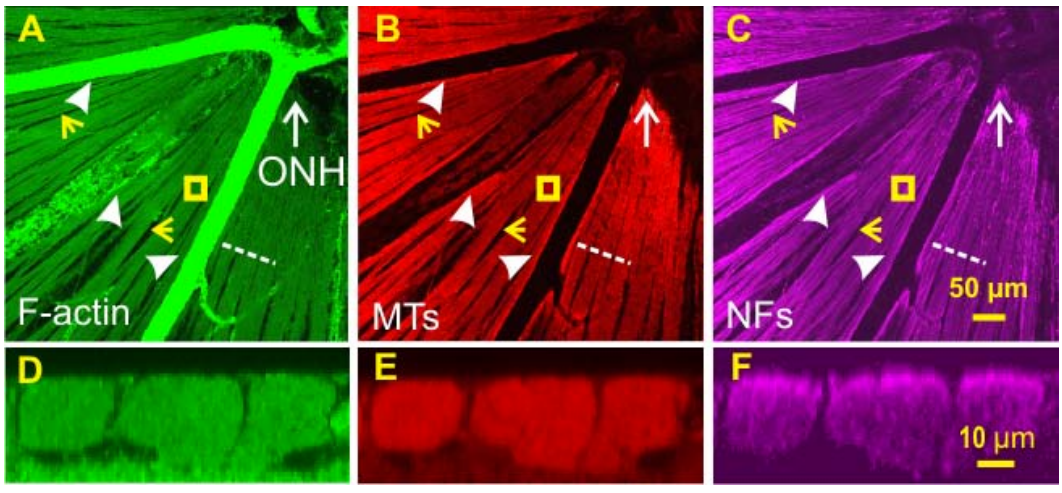

Figure 2.3. Nerve fiber bundles in normal retina. (A-C) En face images of F-actin, MTs and NFs. Bundles were identified as bright stripes with uniform stain. White arrow heads: blood vessels. (D-F) Cross sectional images along dashed lines in (A-C). Bundles were separated by gaps (yellow arrows)

component appeared strong and approximately uniform within the bundles. Blood

vessels were distinguished from bundles by strong phalloidin staining or as hollow structures (white arrow heads). DAPI counterstained nuclei appeared in blood vessels or RGCL (not shown).

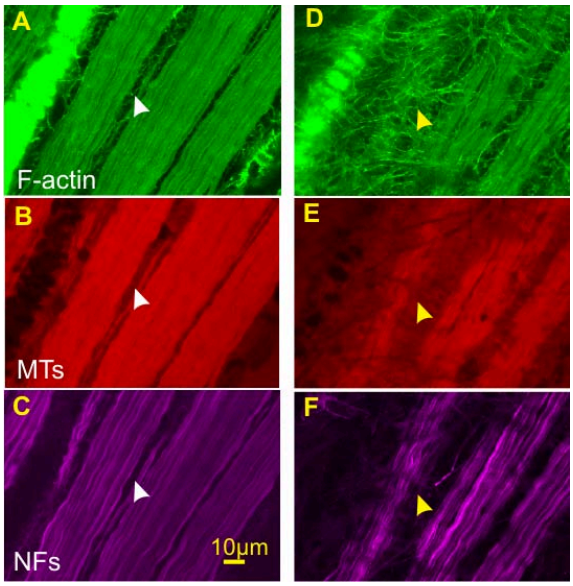

Figure2. 4. F-actin network in the retina. Diffusely distributed F-actin between bundles (A-C, at the depth 5 μm) and near the retinal surface (D-F, at the depth 2 μm). gaps between the bundles were devoid of MT and NF staining (white arrow heads).

Figure 2.4 shows that the gap between bundles was devoid of MT and NF staining, which made the bundle boundaries sharp and clear, however diffusely distributed F-actin was found between the bundles (white arrow heads in Fig 2.4. A-C; images were taken at depth of 5 μm), which demonstrates the network type of F-actin in the retina. F-actin network also appeared on the RNFL surface, while no such network was found in the corresponding MT- and NF-labeled images (yellow arrow heads in Fig 2.4. D-F; images were taken at depth of 2 μm). Note that the left region surface is higher than right side region due to tilt of the tissue.

Cross sectional images of nerve fiber bundles showed uniform stain of each cytoskeleton. The bundles boundaries were clear and gaps between bundles were easily seen. The main stems of blood vessels usually run parallel to bundles with branches traversing the retina in en face images, thus bundles embedded with blood vessels are often seen in CS images (white arrow heads in Figure 2.2B). Although CS images showed that phalloidin and anti-β-tubulin staining also labeled deep retinal layers, bundles, lying just under the retinal surface, were well separated from deeper layers by a single layer of nuclei which were counterstained with DAPI (Figure 2.2B). In normal retina, the RNFL lacked nuclei, except for areas around blood vessels.

2.4.3 Change of Nerve Fiber Bundles and Cytoskeletons at Different Stage of Glaucoma

The progressive distortion of RNFL bundles was observed in retinas with elevated IOP. We arbitrary graded these glaucomatous changes to three stages according to the distortion features: distortion of axonal cytostructures without change in the RNFL thickness (Figure 2.5), thinning of the RNFL (Figure 2.6) and total loss of the nerve fiber bundles (Figure 2.7).

At an early stage of glaucomatous damage, bundles appeared almost normal looking (Figure 2.5). The bundle boundaries were clear in both en face and CS images. In CS images, most of the nuclei were still located under the RNFL. The thickness of the RNFL appeared in the normal range. However, the strands of F-actin started to condense, most likely at the boundaries (white arrow head in Figure 2.5A). No apparent change of MTs and NFs were found at this stage of damage. Quantitative analysis of these structures' texture will be presented later.

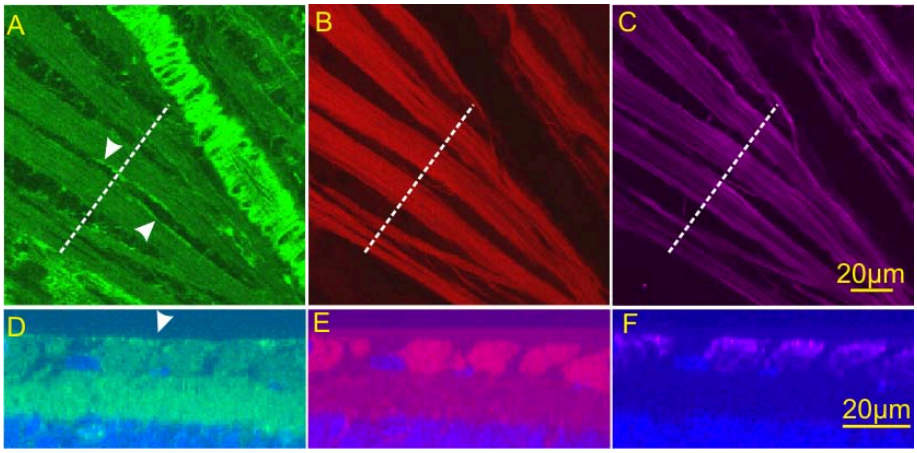

Figure 2.5 Axonal cytostructures at early stages of glaucoma. (A-C) en face image of bundles at early stage of glaucoma shows condensed F-actin staining along the bundle boundaries (white arrow heads). Howerver, the MTs and NFs stain were still strong and uniform. (D-F) Cross section image of the bundles along dashed line in (A-C) with DAPI counterstain. Most of the nuclei were still located under the RNFL. Average RNFL thickness = 16 μm; distance to ONH = 450 μm; length: depth ratio in D-F = 1:1; cIOP: 68 mmHg-days; peak IOP: 40 mmHg.

In retinal regions with more advanced damage, as shown in Figure 2.6, cytoskeletal components were distorted with less oriented structural organization. Bundle boundaries of F-actin were hardly discernible with sporadic staining, while the boundaries of MTs and NFs were still visible. However networks between bundles started to appear in the NF stained images. The thickness of the RNFL

decreased significantly. Both en face and CS images show that nuclei, which were barely seen in normal RNFL, started to appear in the RNFL.

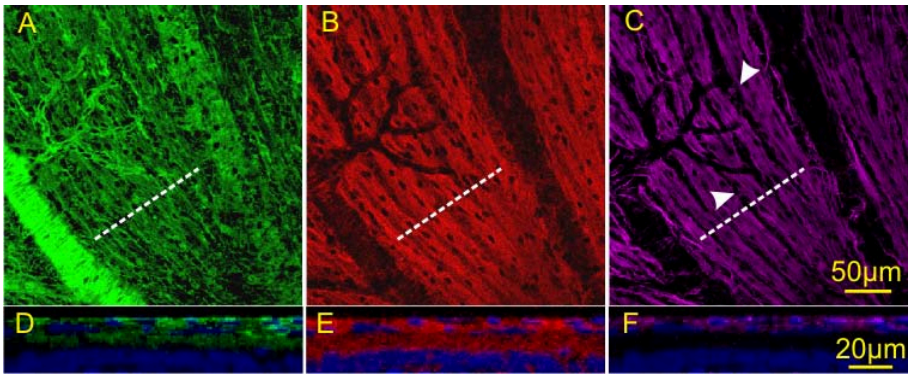

Figure 2.6 Axonal cytoskeleton in mildly damaged RNFL bundles. (A-C) en face image of bundles mildly distorted. Bundle bundaries of F-actin were hardly discernible, while boudaries of MTs and NFs were still visible. Network between bundles were showing in NFs image (white arrow head in C).(D-F) Cross sectional image of the bundles along dashed line in (A-C) with DAPI counterstain. The thickness of RNFL decreased significantly. Average thickness = 9 μm; distance to ONH = 435 μm; length: depth ratio in D-F = 1:1; cIOP: 201 mmHg-days; peak IOP: 54 mmHg.

In severely damaged retinal regions, as shown in Figure 2.7, there were no discernible bundles. F-actin was diffusely distributed and there were barely

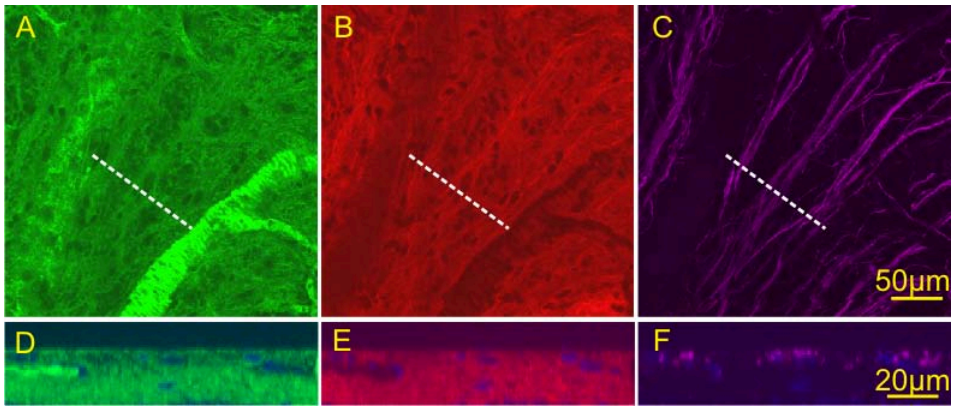

Figure 2.7 Severely damaged RNFL bundles. (A-C) en face image of bundles severely distorted. There were no discernible bundles in F-acin and MTs, but there were few strands of NFs. (D-F) Cross sectional images of the bundles along dashed line in (A-C) with DAPI counterstain. The RNFL almost disappeared. Average RNFL thickness = 3 μm; distance to ONH = 375 μm; length: depth in D-F = 1:1; cIOP: 261 mmHg-days; peak IOP: 52mmHg.

discernible MTs. However, there may be still few strands of NFs along bundle direction, which made that there were about 2 or 3 μm of bundle thickness.

Note that the distances to ONH in Figure 2.5, Figure 2.6 and Figure 2.7 were comparable (~400 μm), and the average RNFL thickness in these images were 16μm, 9μm and 3μm, respectively.

2.4.4 Damage Patterns of Nerve Fiber Bundles and Cytoskeletons in Glaucomatous Retina

Distortion of cytoskeleton was not uniform across the retina. Rather damages of nerve fiber bundles were locally distributed. As shown in Figure 2.8, the bundles in the upper right have condensed F-actin strands, which indicate an early stage of glaucomatous damage. Besides, aberrant strands across the bundles were developed both in the F-actin and NF images. However, the bundles in the lower left region were approximately uniformly stained and appeared smooth and normal looking.

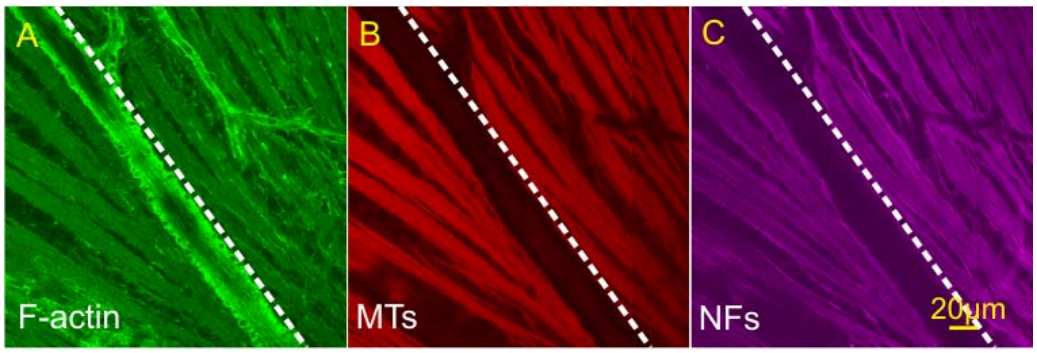

Figure 2.8 Locally distributed glaucomatous damage. Bundles in the upper right show condensation of F-actin, an early sign of glaucomatous damage, whereas the bundles in the lower left region are normal looking with approximately uniform staining of F-actin, MTs and NFs. cIOP: 68 mmHg-days; peak IOP: 40mmHg.

The pattern of structural distortion varied through the depth of the RNFL. The images in Figure 2.9 show structural change with depth of nerve fiber bundles. The images in Figures 2.9A–C were taken at 1 μm below the RNFL

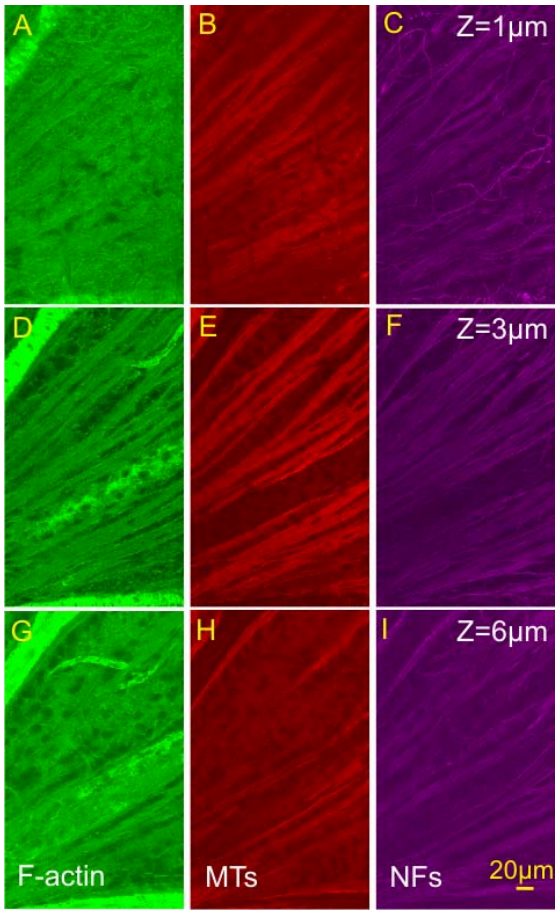

Figure 2.9 Pattern of structural distortion varied through the depth of the RNFL. (A-C) at depth of 1 μm, strands of F-actin were barely seen, aberrant strands were seen in NFs. (D-F) at depth of 3 μm, the bundle courses of all components were clear. (G-I) at depth of 6 μm, most of the distorted bundles started to disappear except NFs. cIOP: 142 mmHg-days; peak IOP: 38mmHg.

surface. The strands of F-actin seem almost disappeared. Aberrant strands across the bundles were developed in the NF images. At a depth of 3 μm (Figures 2.9D–F), the bundle courses of all components were clear, running approximately parallel to the normal ones. The diffusely distributed F-actin between bundles were still present, the crossover strands of NF networks

disappeared at this depth. At a depth of 6 μm from the RNFL surface (Figures 2.9G–I), most of the distorted bundles started to disappear in F-actin and MTs, however there were still strands of NFs present at this depth.

The pattern of structural alteration could be different for different cytoskeleton components as well, which has been shown in Figure 2.5-2.9. Like presented previously, at the early stage of glaucomatous damage, the strands of F-actin in the bundle may start to condense, whereas the bundles of MTs and NFs were still looking normal (Figure 2.5 and Figure 2.8). In Figures 2.9A–C, network and irregular staining of F-actin occurred on retina, and the bundle traces identified by F-actin staining seem almost disappeared. However, there were still discernible bundle traces in MTs and NFs, although there were aberrant strands across NFs image. In Figure 2.7 and Figures 2.9 G-I, there were no apparent strands of F-actin and MTs, while strands of NFs still existed.

2.4.5 Cytoskeletal Texture and Disorganization at Early Stages of Glaucoma

Distortion of the axonal cytoskeleton could occur before thinning of the RNFL. To quantify early cytostructural change within the cross section of bundles, we performed texture analysis on bundles selected in RNFL regions where no apparent thinning occurred. Table 2.2 summarizes the global means and standard deviations for the texture parameters and , as well as the P-value associated with the treatment effect. The average thickness of the selected bundles in the control and treated retinas was similar. For F-actin stain, there was a significant treatment effect for both uniformity and smoothness. For MT stain, there was a significant difference associated with treatment for uniformity

but not for smoothness. In contrast, both texture parameters of the NF stain were not different in the control and treated eyes. The ANOVA model consistently showed statistically significant differences across the different animals.

Table 2.2. Summary of Texture Analysis of Cytoskeletal Components

Bundles	Thickness (μm)	Uniformity (U)			Smoothness(R) (scaled by 1000)		
		F-actin	MTs	NFs	F-actin	MTs	NFs
Control(n=120)*	16 ± 4	0.14 ± 0.05	0.12 ± 0.06	0.28 ± 0.11	0.15 ± 0.12	0.22 ± 0.22	0.20 ± 0.18
Treated(n=80)	17 ± 3	0.12 ± 0.05	0.11 ± 0.05	0.23 ± 0.12	0.34 ± 0.37	0.24 ± 0.32	0.21 ± 0.25
P	0.8	0.003	0.03	0.38	< 0.001	0.47	0.10

* n, number of bundles analyzed.

2.4.6 Change of Nucleus Distribution in the RNFL

Elevated IOP also caused increase of nuclei in the RNFL. In normal retinas, nuclei with DAPI counterstain in the RNFL were mostly distributed between bundles and around or within blood vessels. However, in the treated retinas, abundant nuclei were found in the RNFL and embedded within the bundles (Figure 2.6-2.7).

Moreover, increased nuclei were found in the regions without apparent thinning of the RNFL thickness. Table 2.3 summarizes the nuclear densities in the RNFL and RGCL and the total nuclear density. The densities were measured from the same RNFL sectors which were used in the texture analysis. In normal retinas, the nuclei in RGCL took up 89% of the total amount of nuclei in RNFL and RGCL, whereas the percentage dropped to 53% in treated retinas. Thus it turned out that the density in the RNFL of the treated retinas was significantly higher than that in the normal RNFL and the density in the RGCL of the treated

retinas was significantly lower than that in normal RGCL. However, in both normal and treated retinas, the nuclear density was significantly lower in the RNFL than in the RGCL. Interestingly, the total nuclear density of the treated retinas was found to be significantly higher than that in the control.

Table 2.3. Linear Density of Nuclei in the RNFL and RGCL

Linear Density	RNFL+RGCL	RNFL	RGCL	P (RNFL vs. RGCL)
Control	46 ± 5	5 ± 2	41 ± 5	< 0.001
Treated	53 ± 5	22 ± 4	31± 3	0.01
P (control vs. treated)	0.01	< 0.001	< 0.001	

2.5 Discussion and Conclusion

Axonal F-actin, MTs and NFs closely associate with each other to maintain the rigid architecture of axons. Many studies have been conducted to investigate topographic change of the cytoskeleton in the RNFL and demonstrated patterns of structural change around the ONH in response to various insults [12,14,24,26,64](Villegas-Perez MP, et al. IOVS 2005; 46:ARVO E-Abstract 1234). However, their studies were limited to the damage mechanisms in one or two cytoskeleton components. In this study, we used simultaneous immunohistochemical labeling and confocal imaging to comprehensively investigate the distribution of all the three cytoskeletal components in normal retinas and retinas with different degrees of glaucomatous damage, and the loss of nuclei at early stages of glaucoma.

In normal retina, F-actin, MTs, and NFs were all intensely and uniformly stained with immunofluorescence, indicating that normal RNFL is rich in each of these cytoskeleton components and that these cytostructures are approximately uniformly distributed within bundles.

F-actin is the key component responsible for maintaining cell shape. In addition to bundled F-actin along the course of axons, diffusely distributed actin filaments between bundles and an actin network on the RNFL surface (Figure 2.4) were found in normal retina. No corresponding MTs and/or NFs networks were found. The network beneath the RNFL surface has been proven to be the meshwork of membrane-associated proteins that supports and strengthens the plasma membrane[65]. However the finding of actin filament between bundles was never presented before. One speculation is that they are another form of actin: monomeric globules called G-actin which is free from the chain of polymeric filaments F-actin. .

In retinas with elevated IOP the distribution of axonal cytoskeleton was altered and nuclear density changed in RNFL and RGCL. Features of these cytoskeletal changes include (1) different distortion patterns for different cytoskeleton components; (2) for each component the pattern of alteration varied through the depth of the RNFL and also depended on the stage of tissue damage; (3) alteration of the axonal cytoskeleton could occur before thinning of the RNFL; and (4) F-actin may be the most sensitive and vulnerable structure in its response to elevated IOP.

In early stages of axonal damage, irregular staining of F-actin appeared within the bundles (Figures 2.5A, Figure 2.8A). Interestingly, the intensely stained F-actin strands were often located near bundle boundaries. Formation of condensed F-actin near the bundle boundaries during exposure to elevated IOP may suggest a differential response to stress [66,67], or an early response to

stress on the retina to strengthen the axonal architecture [68]. It could also be an early indication of apoptotic death of ganglion cell axons, as disorganization of F-actin has been related to cell apoptosis [69,70]. We may speculate that under states of elevated IOP, axonal F-actin tries to strengthen cytoarchitecture by developing actin networks between bundles, on bundle surfaces, and even within bundles, and on failure of mechanical protection of axons a cascade of structural degeneration affects all cytoskeleton components due to their interdependent nature [55-58].

Detailed features of structural change of each component are different, which may provide an insight into their damage mechanisms during the development of glaucoma. Mildly damaged retinas showed reduction of orderly distributed strands of F-actin, MTs, and NFs in the RNFL. Irregular staining along strands of all cytoskeleton was found within the bundles. Furthermore, aberrant NFs developed near the RNFL surface (Figure 2.9C). In severely damaged nerve fiber bundles, bundled F-actin and MTs were hardly identifiable or did not exist at all, while clear strands of NFs still ran along the bundle direction (Figure 2.7). This result may suggest that NFs are the cytoskeletal component most tolerant of glaucomatous damage, at least at late stages of the disease. The result indicates that each cytoskeletal component plays a different role in maintenance of axonal architecture and function [71] and therefore responds differently to axonal injury.

Patterns of cytoskeletal alteration varied through the depth of the RNFL (Figure 2.9). A possible explanation of this feature is that stress, induced by

elevated IOP and experienced by the cytoskeleton, varies with depth in the RNFL, resulting in differential responses [67].

Numerous studies have demonstrated that the amount of optic nerve damage is linearly correlated with the cIOP exposure, and pIOP as well. Damage also depends on the maximal IOP difference between the glaucoma and control eyes[60] (Johnson EC, et al. IOVS 1999; 38:ARVO Abstract 3547). In this study, the overall change of cytoskeletons was also related to peak IOP (pIOP) and cumulative IOP (cIOP) (not shown in Results).However, as demonstrated in Figure 2.8, normal looking bundles and bundles with different degrees of damage occurred in the same retina. Hence, there is no simple relationship between RNFL damage and elevation of IOP. Variability of cytoskeletal response to glaucomatous damage is consistent with the variability of RGC loss found in glaucomatous eyes [72]. Localized damage may result from variable RGC distribution across the retina [72-75].

In this study, we also developed the texture analysis method to quantify structural change in bundle cross sections before thinning of RNFL. In bundles without apparent thickness change, both of the textural parameters, uniformity and smoothness of F-actin staining were significantly different from that in the fellow control eyes, suggesting alteration of F-actin distribution within bundles of treated retina. Uniformity of MT staining was also changed significantly, whereas none of the parameters was shown to be changed with the NF stain. These findings further confirmed that axonal F-actin is the most sensitive cytoskeletal component responding to elevation of IOP. Cytostructual change precedes

thinning of RNFL, one of its explanation is that invasion of microglia may contribute to the retention of RNFL thickness since many studies have shown microglia responding to elevation of IOP by increasing expression in the RNFL [68](Wheat JL, et al. IOVS 2010;51:ARVO E-Abstract 2104).

Morphologic and topographic change of RGCs is most often studied in optic nerve diseases. RGC apoptosis and loss of RGCs are evident as shown by many studies with different glaucoma models [25,68,76-78]. In this study, we used DAPI counterstain to identify nuclei in retinal regions, where no apparent change of the RNFL thickness occurred. We found that nuclear density in the RGCL significantly decreased in treated retinas. This result could be interpreted as loss of nuclei in the RGCL. However, the nuclear density in the corresponding RNFL, just above the RGCL, greatly increased. Furthermore, total nuclear density in the RNFL and RGCL was significantly higher in the treated retinas. It was estimated that approximately 50% of cells in the RGCL are displaced amacrine cells [79]. Because we did not directly quantify RGCs, we cannot determine how many, if any, RGCs were displaced to the RNFL. Microglia are highly reactive and mobile cells which play as the first and main force of active immune defense when experienced glaucomatous damage [80]. One explanation for the increase in nuclei could be that the microglia participates in phagocytosis of degenerating RGCs. Further study must overcome the staining limitations and specifically identify change in RGCs and other nuclei in response to glaucomatous damage.

In this project, we used a 40x objective to study the distribution of axonal cytoskeleton. Within nerve fiber bundles, the cytoskeleton appeared as thin, long strands running along the bundles. To further appreciate the cytoskeletal components within bundles, we used a higher power objective with higher resolution and sampling limits to observe each cytostructure. Figure 2.10 shows

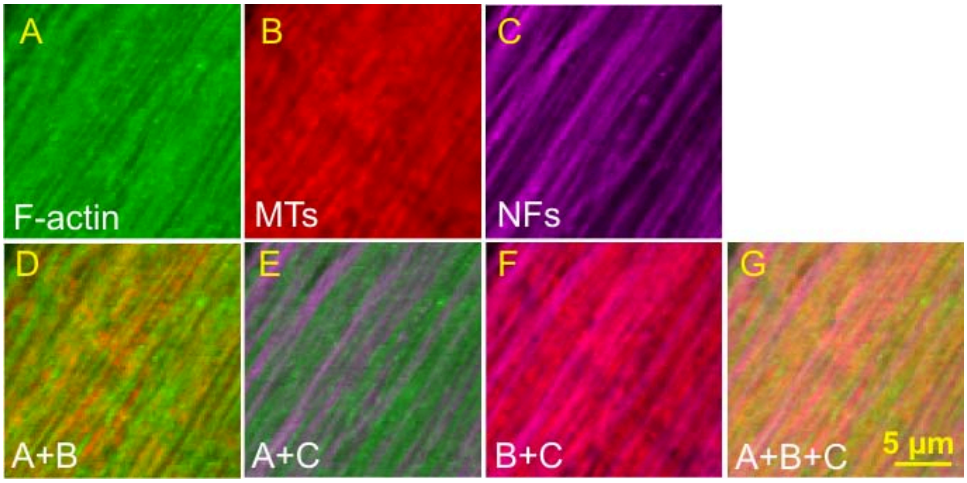

Figure 2.10. En face images of axonal F-actin, MTs and NFs taken with a 63x oil objective. A magnified view of the bundle region outlined in Figure 2.3. (A – C): Strands of F-actin, MTs and NFs of the same nerve fiber bundle. (D – G): Emerged images showing interleaved cytoskeletal strands: (D-F) emerged images of (A) and (B), (A) and (C), (B) and (C); (G) emerged image of (A-C).

a magnified view of the bundle region outlined in Figure 2. 3, taken with a 63x oil-immersion objective. They show dense, striated staining of F-actin, MTs, and NFs strands within bundles. The size of strands ranged from 0.2 µm to 1.5 µm. Moreover, strands with intensely stained F-actin, MTs and NFs may or may not colocalize with each other as shown in the merged images of Figures 2.10D – G. For example, Figure 2.10E shows several intensely stained F-actin and NF strands that were interleaved within a bundle. Colocalization and alternation of the structures most likely reflect the interdependence of these components in both functional and structural organization [55-58].

Considering that the width of alternating strands was within the range of axonal diameters[51], the strands may represent axons rich in any of these cytoskeleton components. Hence, we speculated that axons may or may not contain all three cytoskeletal components and axons might be classified into subtypes based on the contents of cytoskeletal components. Advanced study about classification of axonal subtypes based on cytoskeletal components will be presented in the next chapter.

2.6 Summary

In this project, we developed a staining method for simultaneously labeling F-actin, MTs, NFs and nuclei, and used both en face and in-depth confocal scanning to study axonal cytoskeletal alteration of F-actin, MTs and NFs across the retina, and loss of nuclei in the context of glaucoma. The multiple fluorescence staining method provides simultaneous revealing of distributions of different structural components, making it a powerful tool for studying responses of different cytoskeleton components to axonal injury under the same circumstance. We used whole-mounted retinas to provide a full view of nerve fiber bundle distribution around the ONH, which allows detection of local changes in axonal cytoskeleton across the retina. The confocal imaging method provided both topographic and in-depth view of structural distribution and enhanced the assessment of cytoskeletal change across the retina and at different depths of RNFL. In addition, we developed a method to quantify cytoskeletal texture. This method may provide guidance for studying a comprehensive neuron change in glaucomatous retinas.

With developed methods, it was found that in normal retina all cytoskeletal components were intensely and uniformly stained, indicating that normal RNFL is rich in each of these cytoskeleton components. Insulted by elevated IOP, cytoskeleton was distorted and the detailed features of structural change were different for each component. This result indicates that each cytoskeletal component responds differently to axonal injury. Patterns of cytoskeletal alteration varied through the depth of the RNFL. This suggests that stress, induced by elevated IOP and experienced by the cytoskeleton, varies with depth in the RNFL. It was also found that degrees of RNFL change varied from distortion of axonal cytostructures without change in the RNFL thickness to thinning of the RNFL and total loss of the nerve fiber bundles under the development of glaucoma. Moreover, these characteristic changes could occur in the same retina, a feature that is similar to damage in human glaucomatous retinas. Hence the findings obtained from this project provide a further understanding of damage mechanisms of human glaucoma.

The contribution of Ye Spector to this study was as follows:

- Developed simultaneous fluorescence staining of F-actin, MTs, NFs and nuclei;
- Developed the procedure to do tile scan for confocal images.

Chapter 3. Classification of Axonal Subtypes Based on Cytoskeletal Components

3.1 Background

3.1.1 RGC's Classifications

RGCs are often classified into different subtypes according to their morphology, including RGCs' soma size, dendritical branching patterns, or axonal myelination [81-86]. For example, RGCs in the primate retina are subdivided into six subtypes and further grouped into two general types based on the morphology of their dendritic trees (Figure 3.1) [4,87-90]. RGCs can also

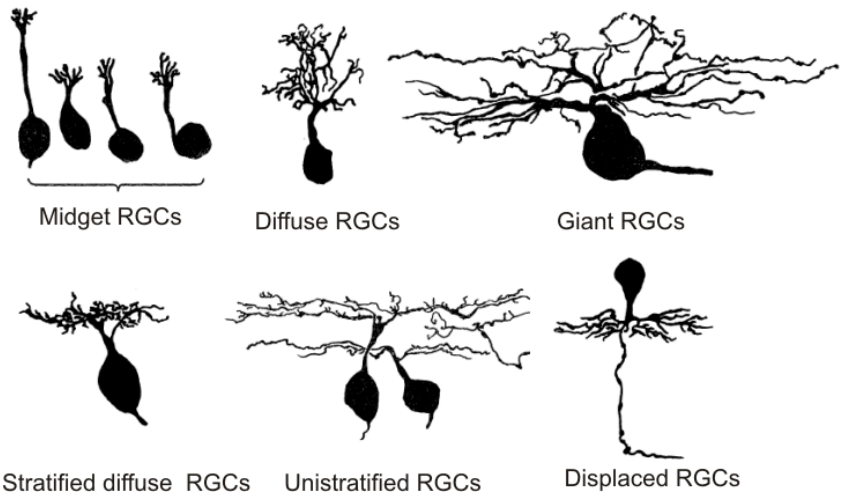

Figure 3.1. Classifications of RGCs according to the morphology of dendritic trees. Redprint from Boycott and Dowling (Figure 80-83) and Polyak (Figure 69,70,87).

be classified into subtypes based on physiological functions. For instance, RGCs could be classified according to their response to light [81-83,91,92]. Some types of RGCs may be good motion detectors, whereas others are sensitive to the orientation of the stimulus. According to their receptive field, RGCs could also be classified into ON-center, OFF-center neurons. Besides that, they could be classified based on the propagation speed of electrical impulses along axons.

3.1.2 Contents of MTs and NFs in Axons

Axons of RGCs contain three major types of protein filaments: actin filaments (F-actin), microtubules (MTs), and neurofilaments (NFs). Like previously stated, these cytoskeletal components, individually and in association with each other, play an important role in axonal function and architecture (cites).

The Electron Microscopy (EM) images with immunochemical staining of MTs and NFs demonstrate that the contents of the two cytoskeletal components differ among axons [93,94]. As illustrated in Figure 3.2, MTs appear as heavily stained dots, and NFs are relatively smaller, lightly stained dots. Studies also

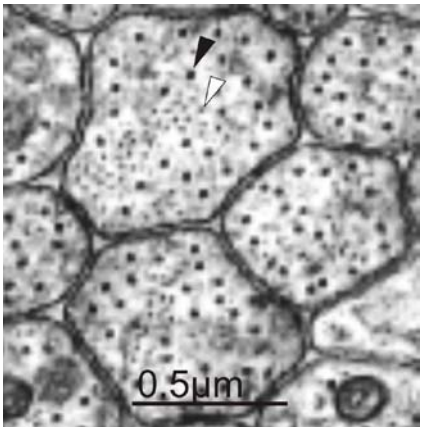

Figure 3.2. Cross-sectional electron microscopy image of normal rat axons with MTs and NFs immunochemical staining. The numbers of MTs (dark arrow) and NFs (white arrow) vary among axons. Black arrow head: MTs; White arrow head: NFs.

have shown that the relative numbers of MTs and NFs change with axonal caliber [93,94]. In nonmyelinated axons of rat sciatic nerves, the ratio of the number of MTs and NFs in an axon changes with axon diameter. For instance, for fibers with axon area of 0.46-0.92μm^2, the ratio of MTs and NFs is 1.6±0.95, but it is 0.59±0.32 for axon area of 0.92-2.25 μm^2. In other words, MTs are more numerous than NFs in small axons while lager axons contain more NFs than

MTs. This finding suggests that MTs are a dominant component in small axons whereas NFs are dominant in larger axons.

EM provides identification of individual cytoskeletal components in axons and allows quantitative measurements of each component within axons. However, EM provides a limited number of axons to be examined. Also, it is difficult to locate analyzed axons in the retina, limiting a whole view of cytoskeletal distribution across the retina. In this study, we used immunohistochemical staining and confocal imaging to classify subtypes of axons based on the contents of F-actin, MTs and NFs within axons. Because whole-mounted retinas were used, the distributions of axonal subtypes across the retina were investigated in normal rat retinas.

3.2 Purpose and Hypothesis

Due to the diversity of ganglion cell properties, RGCs are often classified into different subtypes based on their morphology or functional characteristics. However, little is known about organization and variation of the ultrastructures in axons. We have found that axons may or may not contain all three cytoskeletal components, therefore, we hypothesized that the content of each cytoskeletal component differed among axons and axons could be classified into different subtypes based on the contents of these components. We used simultaneous immunochemical staining of F-actin, MTs and NFs and high resolution confocal imaging to identify these components within axons and study the distribution of classified axonal subtypes across normal rat retinas.

3.3 Experimental Materials and Methods

3.3.1 Confocal Laser Scanning Imaging

Tissue preparation and immunohistochemical staining followed the developed procedures described in Chapter 2.

As demonstrated in Figure 2.10, Chapter 2, images taken with a 63x oil objective show dense, striated staining of F-actin, MTs, and NFs strands running along bundles. Moreover, intensely stained strands may or may not colocalize with each other, which was hard to tell in mages taken with a 40x objective. In this project a 63x oil objective was used. It provided a full field of view of 246 μm x 246 μm and a resolution of 0.24 μm/pixel. For each retina, four regions, dorsal, rostral, ventral and caudal retina, around the optic nerve head (ONH) were imaged with each region scanned by 2 x 3 or 3 x 2 tiled arrays. For a subset of retinas, a peripheral retinal region with a distance to the ONH center of approximate 1.25 mm was also scanned. For each array position, en face images were collected at evenly spaced positions in depth (1 μm apart in tissue) starting from the retinal nerve fiber layer (RNFL) surface through the retina to a depth at least including the RGC layer.

To identify the locations of bundles imaged by a 63x objective in a whole mounted retina, a 10x objective and a 40x oil objective were also used to take en face images at the middle depth of the RNFL. A tiled array of images with a 10x objective was taken to provide a full field view of the whole mounted retina. A tiled array of images with a 40x objective, covering a retinal area of at least 1.2 mm^2 with the ONH at the center, provided a clear view of bundles and blood vessels around the ONH. En face images taken with 10x, 40x and 63x objectives

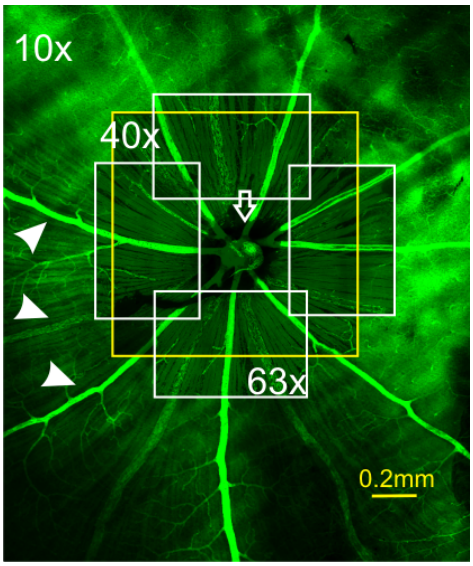

Figure 3.3. Registration of 10x, 40x and 63x objective images on phalloidin stained F-actin. Bundles and blood vessels from each image were well matched. For better review, 40x image was outlined by a yellow rectangle, 63x images were outlined by four white rectangles. White arrow heads: blood vessels; white hollow arrow: ONH.

were registered by matching bundles and blood vessels shown in images (Figure 3.3). The registered images were then used to identify bundle and axon locations in the retina.

3.3.2 Selection of Bundle Locations

Axonal subtypes were studied across the retina (Figure 3.4). To study the distribution of axonal subtypes along bundles, bundles were selected in the central retina at distances of 0.25 mm, 0.35 mm and 0.45 mm (corresponding to a 4.3° vision field) from the ONH center and in the peripheral retina at distances ranging from 1.0 mm to 1.5 mm (corresponding to a 14.1° vision field). To determine subtype distribution around the ONH, bundles were chosen from four quadrants: dorsal, rostral, ventral, and casual retina.

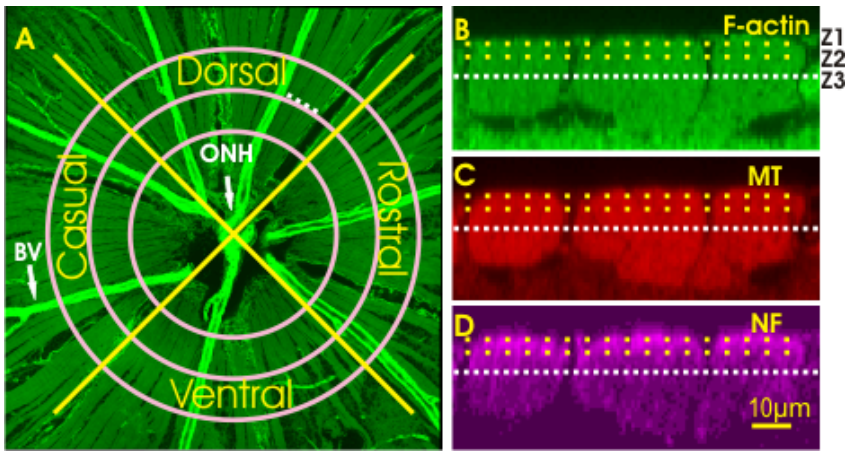

Figure 3.4. Selection of bundle locations for studying axonal subtypes. En face confocal image of a normal rat retina with phalloidin stain of F-actin. Bundles show as bright stripes radiating from the ONH. Blood vessels (BV) appear as over-expressed phalloidin. Axonal subtypes were studied at radii of 0.25 mm, 0.35 mm and 0.45 mm and in four quadrants. Image size: 1.2 mm x 1.2 mm; image taken with a 40x objective.

3.3.3 Classification of Axonal Subtypes

Axonal subtypes were determined in en face images taken at depth of 2 - 3 μm and 4 – 6 μm under RNFL surface as demonstrated in Figures 3.4 B-D. With a 63x oil objective, F-actin, MTs and NFs were identified as thin strands running along bundles (Figures 3.5A – C). To determine the relative contents of each cytoskeletal component across axons, three parallel lines, 1μm apart, across cytoskeletal strands were defined within a selected nerve fiber bundle (Figures 3.5A – C). The intensity profiles along the parallel lines were obtained for each component. An average of these three intensity profiles was then used to describe the intensity distribution of a cytoskeletal component across axons (dotted lines in Figures 3.5D – F).

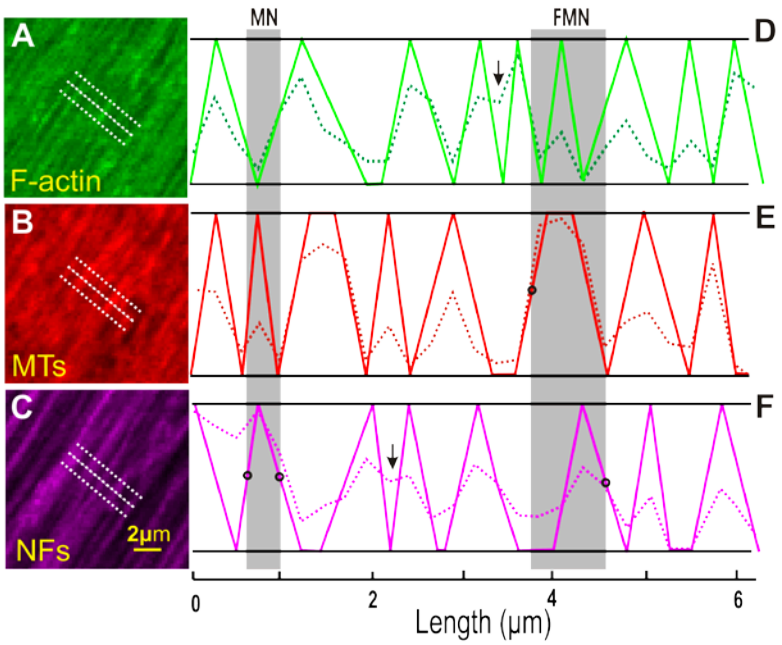

Figure 3.5. Classification of axonal subtypes. (A-C) En face images of F-actin, MTs and NFs of the same nerve fiber bundle (image taken with a 63x oil objective). (D-F) Dotted lines: average intensity profiles along the dashed lines in (A-C); arrows: ambiguous intensity peaks; solid lines: converted sawtooth binary curves (see details in the text); grey areas: windows used to identify subtypes of axons; dots: points at half height of sawtooth.

The intensity profile of a cytoskeletal component showed the relative contents of this component in the axons that were intercepted by a line. To simplify classification of axonal subtypes, an intensity profile was converted into a sawtooth binary curve with 1s for strong stain and 0s for weak stain (solid lines in Figures 3.5D – F). Note that along a binary curve the 0s, which corresponding to the gaps between strands in an en face image, could indicate either low content of a cytoskeletal component or lack of this specific component. For ambiguous intensity peaks (arrows in Figure 3.5D and 3.5F), they were visually examined in the corresponding en face images and determined as either separated strands or a single strand.

To determine an axon, a window with an adjustable width was moved along the sawtooth curves of F-actin, MTs and NFs. As illustrated in Figures 3.5D – F, the left side of the gray window was defined when it crossed at least one middle point of the upward side of sawtooth without containing any downward sides that had more than a half height of sawtooth; similarly, the right side of the window was defined when it crossed at least one middle point of the downward side of sawtooth without containing any upward sides that had more than a half height of sawtooth. The width of a window varied from 0.24 μm to 2 μm with the low value equal to the confocal imaging resolution and the high value determined by the reported axonal sizes found in rat RNFL[51].

Subtypes of axons were then determined by intensely stained components. For instance, axons with intensely stained MTs and NFs (1s for MT and NF) but weak or no stain of F-actin (0s for F-actin) were classified as MN subtypes; axons with intensely stained F-actin, MTs and NFs (1s for all three) were classified as FMN subtypes (grey areas in Figures 3.5D – F). A linear density of each subtype was calculated as the number of the subtype found along a line divided by the line length. Unless stated otherwise, an average value of the densities measured at the depth of 2 - 3 μm and 4 – 6 μm under the RNFL surface will be presented in the Results.

3.3.4 Determination of Strand Size, Axon Size and Bundle Size

The strand size of a cytoskeletal component was defined as the full width at half maximum of sawtooth. An axon size was defined as the width of a window described above.

For the purpose of studying the relationship between subtype densities and bundle area and between subtype densities and bundle thickness, the thickness of bundles was measured from cross sectional images of the retina, which was derived from reconstruction of 3-D images. The bundle size was proximately estimated by multiplying bundle width with its thickness.

3.3.5 Repeatability and Reproducibility Test

To determine repeatability and reproducibility of classification of axonal subtypes, two subjects were trained with the developed methods and then independently classified axonal subtypes of the same selected bundles. Both subjects repeated classification of the same bundles at least two weeks later.

3.3.6 Statistical Analysis

For topographic distribution analysis, all the data were fitted in mixed linear models with location around the ONH as factors and distances to the ONH included as a covariate. Each rat number was also included as a random effect. Paired measurements were compared with paired T-test for means. The significance level was set at $P < 0.05$.

Averaged values are reported as mean ± standard of error of the mean (s.e.m.).

3.4 Results

3.4.1 Cytoskeletal Strands in Retinal Nerve Fiber Bundles

Similar to the en face images taken with the 40x objective, as demonstrated in (Section 2.4.2), en face images taken with a 63x objective also showed that retinal nerve bundles present as bright stripes and cytoskeleton appeared as thin, long strands running along the bundles.

In the central retina, the sizes of F-actin, MT and NF strands, 0.45 ± 0.04 μm, 0.46 ± 0.04 μm and 0.49 ± 0.04 μm respectively, were not significantly different ($p > 0.5$). Similar results were found in the peripheral retina (R = 1.0 – 1.5 mm). The strand size is comparable with axonal size (0.12 to 2 μm), therefore, the strands of cytoskeletal components represent axons within retinal nerve fiber bundles.

Strands with intensely stained F-actin, MTs and NFs may or may not colocalize with each other. To identify the contents of F-actin, MTs and NFs strands within the same axon, the intensity profiles along a line intercepting the strands were plotted (Figure 3.6). Along an intensity profile, peaks corresponded to strands with brighter stain while valleys corresponded to weaker stain or no stain of a cytoskeletal component. For the same axon, it contained one or more intensely stained cytoskeletal components. The gray bars in Figure 3.6 demonstrate axons that contained all intensely stained cytoskeletal components

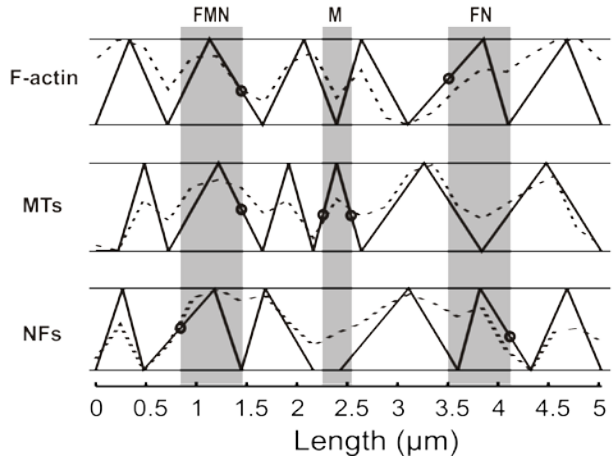

Figure 3.6. Contents of cytoskeletal components across axons. Dashed curves: average intensity profiles along the lines defined in Figure 4A-C; solid lines; converted binary profiles; gray bars: examples of axonal subtypes (details in the text); and dots: defined boundaries of axons. Intensity values were arbitrary.

(FMN subtype), MTs only (M subtype), and intensely stained F-actin and NFs strands (FN subtype).

3.4.2 Axonal Subtypes across the Retina

By using converted intensity profiles, axons were classified into seven subtypes: FMN, FM, FN, MN subtypes, in which at least two or three cytoskeletal components were intensely stained, and F, M, and N subtypes, in which only one cytoskeletal component was relatively intensely stained within an axon.

Sixty bundles in eight retinas were studied around the ONH with bundle areas selected near the ONH at the distances of 0.25, 0.35 and 0.45 mm from the ONH center in this study. Total of 2238 axons in the 60 bundles was classified. For each selected nerve fiber bundle, at least 15 axons were analyzed. Subtypes were classified in en face images taken at depth of 2 – 3 μm and 4 – 6 μm under the RNFL surface. The paired t-test did not find significant difference between the linear densities measured at the two depths ($p > 0.1$). Hence, average of the linear densities at different depths was used in this study. Figure

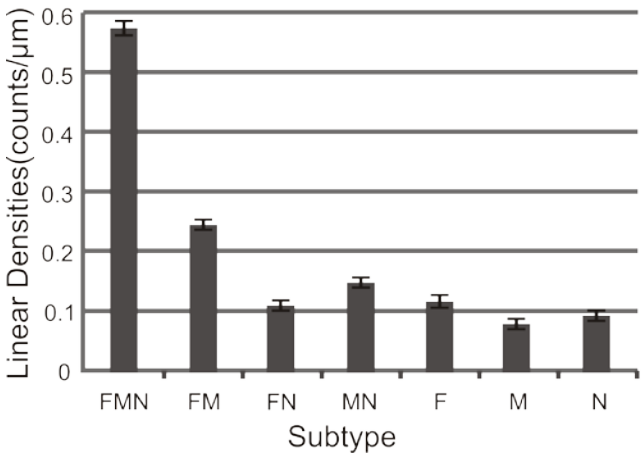

Figure 3.7. Axonal subtypes in normal rat central retinas. Bar: Linear densities of axonal subtypes (mean± s.e.m.).

3.7 summaries the linear densities of classified axonal subtypes. The densities combined all measurements from different distances and quadrants of the central retina. In the central retina around the ONH, subtype FMN, which contained all intensely stained components, was the most abundant subtype, which took up 42% of the total counted axons. Subtype FM with both intensely stained F-actin and MT was the second most abundant subtype, which took up 18% of the counted axons. Total of 79% axons contained at least two intensely stained components. Subtype with one cytoskeletal component intensely stained took up 8% (F subtype), 6% (M subtype) and 7% (N subtype), respectively, of the total counted axons in near ONH region.

3.4.3 Distribution of Axonal Subtypes around the ONH and along Bundles

To study the distribution of each subtype around the ONH, the data displayed in Figure 3.7 are regrouped by combining measurements taken at different radii. For each quadrant, at least 14 bundles were included. Figure 3.8 shows the distribution of each subtype around the ONH. The densities of all

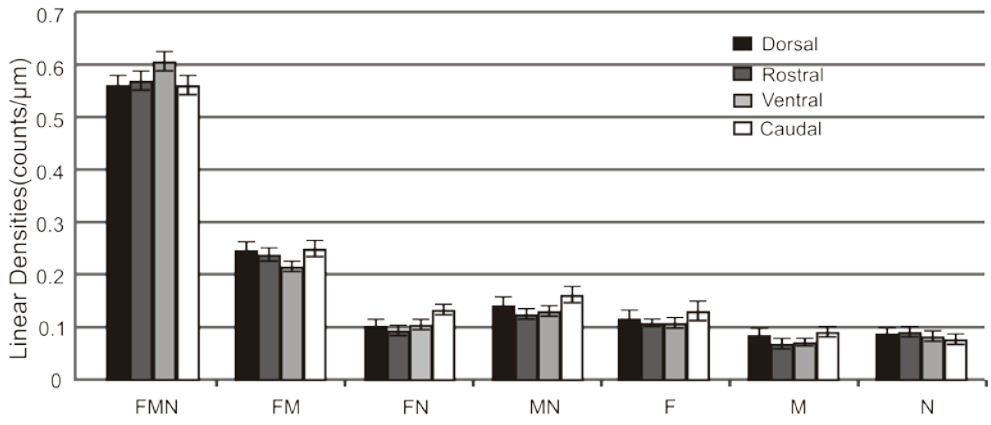

Figure 3.8. Axonal subtypes distribution around the ONH in normal rat retinas (mean ± s.e.m).

subtypes did not changed significantly across the retinal quadrants in the central retina ($p > 0.05$).

To study distributions of axonal subtypes along bundles, the data in Figure 3.7 was regrouped by combining the measurements from all retinal quadrants. At least 29 bundles were included in each radius. As shown in Figure 3.9A, there was no significant change of the linear density at distances ranging from 0.25 mm to 0.45 mm ($p > 0.11$).

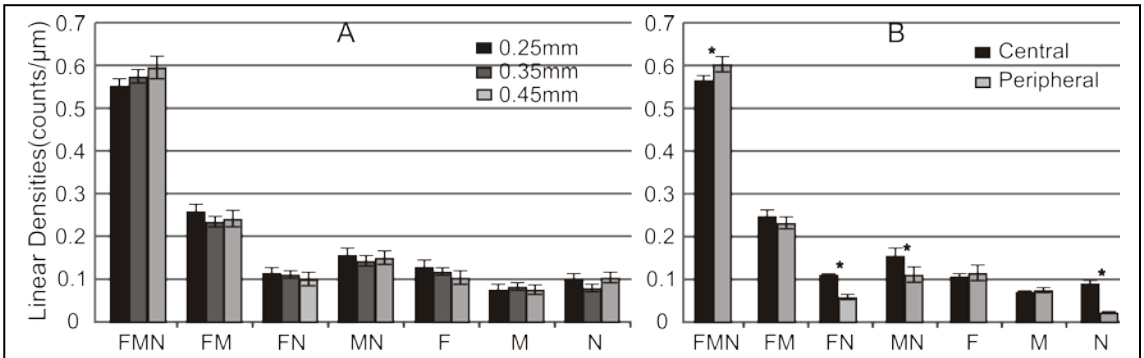

Figure 3.9. Axonal subtypes distribution along bundles (mean ± s.e.m). (A) Axonal subtype densities along bundles in the central retina. (B) Axonal subtype densities in the central and peripheral retinas. * indicates statistically difference of measured linear densities with paired t-test.

To compare subtype distribution in the central and peripheral retinas, 48 bundles in the same eight retinas were also studied with bundles selected at the distances of 1.0 mm to 1.5 mm from the ONH center. Figure 3.9B shows that the linear densities of the subtypes which had low or no contents of NFs, that is, subtypes FM, F and M, were not significantly different between the central and peripheral retinas. However, the linear density of subtype FMN was significantly higher in the peripheral region ($p = 0.03$) while the linear densities of subtypes FN, MN and N were significantly lower in the peripheral region ($p < 0.005$). The

linear density of all subtypes that contained FN strands was found significantly higher in the central retina.

3.4.4 Relationship between Axonal Subtype and Size

Figure 3.10 shows the relationship between the axonal subtype and size. Axonal size was highly significantly different by subtype with the size of subtype

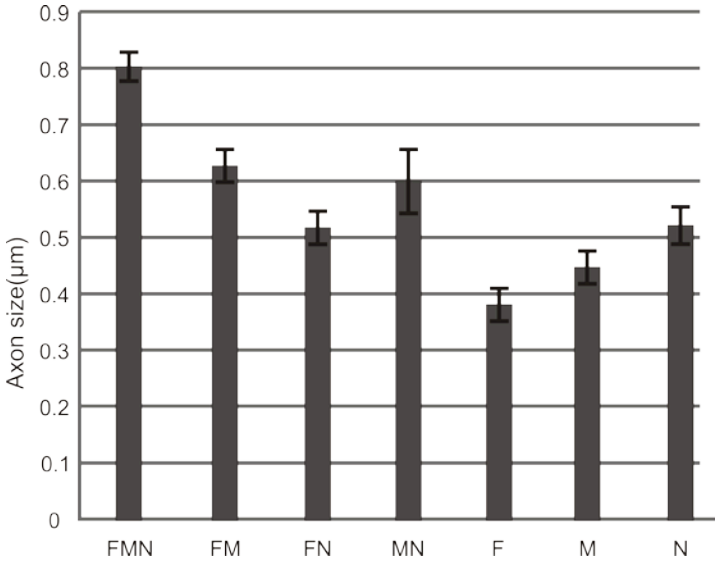

Figure 3.10. Axonal sizes of subtypes (mean ± s.e.m).

FMN significantly higher than all other subtypes ($p<0.005$). Among the axons with two intensely stained components, the comparison between each other shows no significant difference except the axon size of subtype FM is significantly higher than the one of subtype FN ($p<0.05$). Similarly, among the axons with one intensely stained component, the comparison between each other shows no significant difference except the axon size of subtype F is significantly less than the one of subtype N ($p<0.05$).

No significance was found between the sizes of each axonal subtype in the central and the peripheral retinas ($p > 0.11$).

3.4.5 The Relationship between Subtypes Densities and Bundle Area

Different sizes of bundles were selected at random radii and in random quadrant of retinas. The relationships between subtype densities and bundle area and thickness were also investigated. The results show that the linear density of each subtype didn't apparently vary with either bundle size or bundle thickness. Figure 3.11 shows that the linear density of FMN subtype doesn't change with bundle thickness.

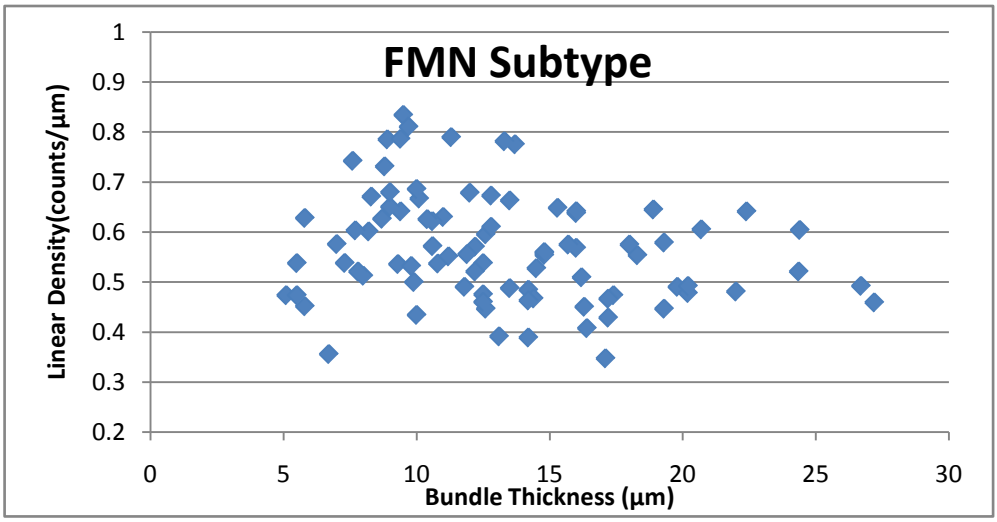

Figure 3.11. The linear density of FMN subtype doesn't change with bundle thickness.

3.4.6 Repeatability and Reproducibility of Classification of Axonal Subtypes

Twenty-seven bundles at six retinas were used to determine repeatability and reproducibility of classification of axonal subtypes. Linear densities of each subtype measured by two subjects are not significantly different. No significant difference was found for the densities measured at different times by the same subject ($p > 0.2$).

3.5 Conclusion and Discussion

F-actin, MTs and NFs closely associate with each other to maintain the rigid architecture and provide function aid of axons [23,52,54-59,95-97]. EM images, however, demonstrate that the content of each cytoskeletal component differs among axons [94,98-100], as illustrated in Figure 3.2. Studies also demonstrated that the relative content of MTs and NFs varies with axonal calibers [93,94].

With high resolution confocal imaging, strands of F-actin, MTs and NFs were found running along nerve fiber bundles [27,73,101](Villegas-Perez MP, et al. IOVS 2005; 46:ARVO E-Abstract 1234). The strand sizes were within the range of axonal size. Note that confocal imaging does not identify a single cytoskeletal component as imaged by EM. The strand of a component in confocal images represents a number of this component clustering together within an axon. In normal rat retinas, an axon may or may not contain all strands of F-actin, MTs and NFs (Figure 2.10 and Figure 3.5D – F). This study developed a method that used an intensity profile of fluorescent staining to identify axons that contained F-actin, MTs and/or NFs strands. We found that not all axons contained strands of F-actin, MTs and NFs, that is, the subtype of FMN is not the only subtype of axon. However, FMN subtype was the most abundant subtype axons in normal rat retinas. About 79% axons contained at least two or more cytoskeletal strands, indicating that most of axons require at least two dominant cytoskeletal components. The space between strands, represented by a low value of fluorescent intensity, may not suggest non-content of a cytoskeletal component; rather a subtype with one component, for instance the subtype F,

may contain MTs and NFs but with very low contents comparing with their contents in the neighboring axons.

NFs are assemblies of three protein subunits, NF-L, NF-M, and NF-H [102]. In this study staining of NFs identified NF-H only. Because the three protein units are usually associated together [102,103], staining all three subunits of NFs may result in similar results found in this study.

In this study linear densities of subtypes were used to quantitatively describe the distributions of axonal subtypes across the retina. The linear density of each subtype was not significantly different around the ONH. The result suggests that there is no preferential distribution of any axonal subtype around the ONH in normal rat retinas. However, studies by others find that the topographic distribution of RGCs varies substantially across the retina and among animals as well [72-75]. The uniform distribution of axonal subtypes found in this study could be due to averaging the linear densities across different retinas.

By comparing the central and peripheral retinas, the density of FMN subtype was significantly higher in the peripheral region, while the densities of any other subtypes that contained NF strands decreased significantly in the same region. Yet, the density of total NF strands was significantly higher in the central retina than in the peripheral retinas. The result suggests that the density of NF strands change with the bundle distance from the ONH; rather the change of combination of NF strands with F-actin and MT strands doesn't go in the same direction with the combination of NF strands with F-actin or MT strands along the

bundle. Difference of a subtype's density in central and peripheral retinas may suggest that axonal architecture and function are different in these regions [72-75,98]. The study also found that the size of axons associated with classified subtypes, which is consistent with the evidence that the axonal size can serve as a reasonable parameter to distinguish different classes of RGCs [104,105]. The current study focused on the development of a new classification method. Future studies should investigate the association between axonal subtypes and functions and understand the relationship between axonal subtypes and RGC subtypes classified by other methods [81-86,91,98,106-109].

RGCs have not been classified based on the contents of axonal cytoskeletal components. The classification method developed in this study will provide a new means to investigate selective damage of axons in many ocular neuropathic diseases, including glaucoma [12-14,25,26,28,110]. Preferential distortion of cytoskeletal components happens in the optic nerve with early glaucomatous damage[12,14]. In the central retina, distortion of axonal F-actin occurs prior to change of MTs and NFs[110]. These findings suggest that each cytoskeletal component responds differently to disease damage. Classification of axons based on the contents of cytoskeletal components will provide an enhanced understanding of damage mechanisms of axons in glaucoma and other ocular neuropathic diseases.

3.6 Summary

In this study, we proposed a new method to classify RGCs based on the content of each cytoskeletal component in axons. We used immunochemical

staining of F-actin, MTs and NFs and high resolution confocal imaging to identify these components within axons and study the distribution of classified axonal subtypes across normal rat retinas. The simultaneous staining of F-actin, MTs and NFs reveals the contents of each cytoskeleton in an axon at the same time, allowing the identification of each component in the same axon. The use of cLSM overcomes the limitation of EM to examine large amount of axons and to locate analyzed axons in the retina, results in the possibility to investigate the cytoskeletal distribution across the retina. Linear densities of subtypes were used to quantify these distributions.

With the developed methods, we found that FMN subtype was the most abundant subtype axons in normal rat retinas, and almost 80% of the axons contained at least two or more cytoskeletal strands. There is no preferential distribution of any axonal subtype around the ONH in normal rat retinas; however axons with NF intensely stained change with the bundle distance from the ONH. Different distribution may suggest differences of axonal architecture and function. The study also found that the size of axons associated with classified subtypes, showing supplementary evidence that the axonal size can serve as a reasonable parameter to distinguish different classes of RGCs.

Previous studies have shown that each cytoskeletal component responds differently to disease damage. Classification of axons based on the contents of cytoskeletal components will provide an enhanced understanding of damage mechanisms of axons in glaucoma and other ocular neuropathic diseases.

The contribution of Ye Spector to this study was as follows:

- Developed a new idea of classifying axons into different subtypes; based on contents of cytoskeletal components;
- Designed the method of converting intensity profiles to binary curves;
- Developed the method of using moving window to identify axonal subtypes

Chapter 4. RNFL Reflectance and Spectrum in Glaucomatous Retinas

4.1 Background

Glaucoma damages the RNFL, which occurs prior to detectable vision field loss. Optical methods, such as, OCT and SLP, have been developed to measure RNFL thickness, which is derived from the optical properties of the RNFL. These methods provide quantitative and objective assessment of the RNFL. However, many clinical studies show that RNFL thickness measurement is not sensitive enough to detect early glaucomatous damage. There must be knowledge gap between RNFL optical properties and damage mechanisms of glaucoma. To improve our understanding of RNFL optical properties under the glaucomatous development, this study investigated changes of RNFL reflectance and spectrum in retinas with glaucomatous damage.

4.1.1 Directional Reflectance of RNFL

RNFL reflectance arises from light scattering by parallel cylindrical structures in axons [1,3,111]. Light scattering by cylinders has a special property that the light must be confined to a conical sheet concentric with the axis of the cylinder [112,113]. The unique geometry of light scattering by a cylinder is shown in Figure 4.1.

Let the incident angle be the angle between the incident ray and a plane perpendicular to the cylinder. The scattered light is confined to a cone coaxial with the cylinder [111-113] . The apex angle of the cone is twice the angle between the cylinder axis and the incident ray. The scattering angle was defined as the angle between incident and scattering planes, where the incident plane

contained the incident ray and the cylinder, and the scattering plane contained the reflected ray and the cylinder. Forward scattering is at 0°, and backscattering is at 180°.

A single cylinder or an array of perfectly parallel cylinders scatters a ray of light into an infinitesimally thin conical sheet. Misalignment of cylinders in a

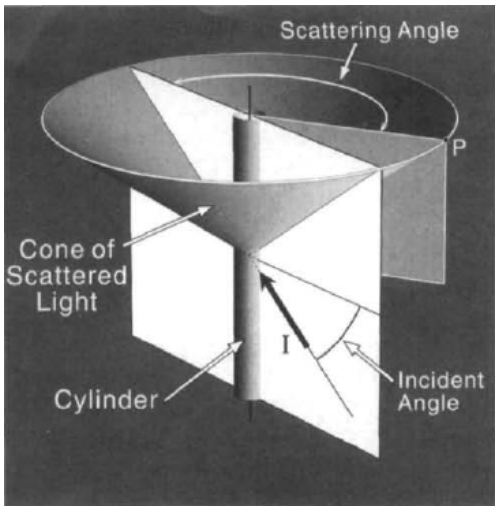

Figure 4.1. Geometry of light scattering by a cylinder. The light scattered by a cylinder from an incident ray (I) is confined to a conical sheet coaxial with the cylinder axis. The apex angle of the cone is twice the angle between the cylinder axis and the incident ray. The incident angle is specified as the angle between the incident ray and a plane perpendicular to the cylinder. The scattering angle of a ray passing through a point (P) on the cone is specified as the angle between two planes that intersect at the cylinder axis, the plane containing the incident ray and the plane containing P. The diagram depicts a scattering angle of 150°. Image reprinted from Robert W. Knighton and Xiang-Run Huang (1999) (Figure 2) [1,3]

scattering array will broaden the scattered sheet, and, in addition, the finite apertures of the light source and camera will spread the measured cone around its actual location [111].

The geometry of Figure 4.1 also works in reverse; an incident ray that lies in the cone and passes through point "P" will be scattered to an observer looking in the direction "I" with the same intensity as the illustrated geometry. To achieve a stable image (i.e., a constant relationship between the camera and the retina),

the reversed geometry was used in the experiments reported here, i.e. the incident angle was adjusted to look for near maximum (on-peak) reflectance measurement of RNFL while the position of camera and the bundle (array of parallel cylinders) were fixed.

4.1.2 RNFL Reflectance Spectrum In Normal Retina

RNFL reflectance is wavelength dependent in normal retinas. In normal retinas, RNFL reflectance is high at short wavelengths and decrease with increasing wavelength (Figure 4.2) [1]. The spectra can be described by a two-

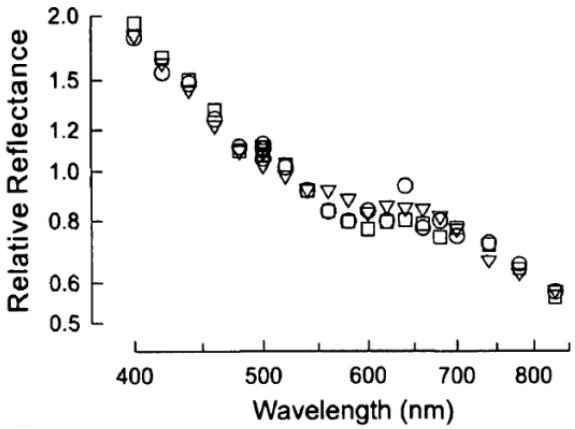

Figure 4.2. Spectral reflectance of the RNFL. Reprint from Drs. Knighton and Huang [1] (1999, Figure 5B).

mechanism cylindrical scattering model. The model suggests that both thin and thick cylindrical structures may contribute to RNFL reflectance with thin cylinders contribute more to the scattering at short wavelengths and thick cylinders dominate the scattering at long wavelengths [1].

RNFL reflectance is also proportional to its thickness. The proportional relation between reflectance and thickness suggests that the reflected light arises from the entire volume of a nerve fiber bundle [3].

4.2 Purpose and Hypothesis

RNFL reflectance arises from light scattering of axons. Glaucoma damages axons of RGCs. Hence it should result in change of RNFL reflectance. Furthermore, RNFL reflectance arises from different cylinders and glaucoma causes selective damage of axonal ultrastructure [14,26,28,33,77,114]. It is plausible that change of RNFL reflectance under glaucomatous damage is wavelength dependent. The goals of this study were to measure the RNFL reflectance spectra with different degrees of glaucomatous damage and investigate the relation between the RNFL reflectance and thickness at early stages of glaucoma.

4.3 Experimental Materials and Methods

4.3.1 Tissue Preparation

Tissue preparation followed the developed procedures described in Chapter II. After a retina was dissected from the retinal pigment epithelium and choroid, it was draped across a slit on a black membrane with the photoreceptor side against the membrane. A second thinner membrane with a slit matched to the black membrane was put on the RNFL surface to gently stretch the retina and eliminate wrinkle. The above procedure was performed with intense white illumination, which thoroughly bleached the visual pigment in the photoreceptors and ensured that the reflectance in this layer remained constant. The mounted retina was placed in a chamber perfused with an oxygenated warm physiological solution to keep the tissue alive.

4.3.2 *Multispectral Imaging Microreflectometer*

An imaging microreflectometer (IMR) was used in this study to measure the reflectance of RNFL. The optical design of IMR is described as follows (Figure 4. 3). The retina mounted in a chamber is illuminated by a quasi-chromatic light

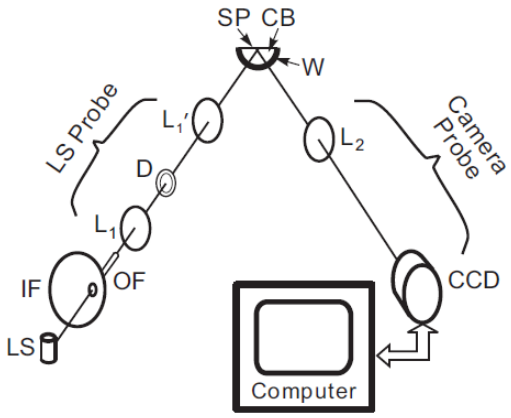

Figure 4.3. Schematic diagram of the multispectral imaging microreflectometer. LS, light source; IF, interference filter; OF, optic fiber; D, diaphragm; L1, L1', and L2, lens; SP, specimen; CB, specimen chamber; W, spherical window; CCD, charge-coupled device. The optical axes of light source and camera intersected at the center of the spherical window. Image reprinted from Xiang-Run Huang, Robert W. Knighton, et al. (2006) (Figure 1)[2]

source that uses a tungsten-halogen lamp and interference filters (10-nm full width at half maximum). Filters are available for wavelengths ranging from 400 nm to 830 nm. The retina is imaged by a camera consisting of an objective lens (f-number = 3.6) and a cooled charge-coupled device (CCD) which provides a digital resolution of 2.2 μm/pixel in an aqueous medium and a full field of view of 2.3 x 2.3mm on the retina. The optical axes of the camera and light source (LS) coincide with radii of a spherical coordinate system centered on the retina. The camera can be moved in azimuth on the equator of the system, and the light source can be adjusted both in azimuth and elevation.

The calibration of IMR system is important to make sure the precision of reflectance measurement. The calibration procedure was described in Appendix.

4.3.3 *Measurement of RNFL Reflectance*

Images of RNFL were collected by the CCD camera at wavelength ranging from 400 to 830nm. Exposure duration of the CCD was selected to ensure that no saturation occurred in any images at any wavelength (Table 4.1). Note that the light source intensity was also attenuated with neutral density filters as necessary to achieve desired exposure time for each wavelength. Black images, taken with the same exposure duration but with the light source off, were subtracted from each image to compensate for the dark current and bias level of the CCD. The resulting pixel values in each image were directly proportional to reflectance intensity. To calculate relative reflectance of the RNFL, image reflectance intensities were also calibrated to reflectance measured on a diffuse white reflector, which has a known reflectance coefficient calibrated by the manufacture (6080 White Reflectance Coating; Eastman Kodak Company, Rochester, NY). Pixel values of retinal images were converted to relative reflectance Rλ by

$$R_\lambda = \gamma_\lambda \frac{P}{P_\omega}\frac{T_\omega}{T} \qquad (4.1)$$

where γ_λ is a known reflectance coefficient of the white reflector at wavelength λ; P and P_ω are pixel values of the tissue and white reflector, respectively; and T and T_ω are their corresponding exposure durations. In our studies, the relative reflectance is simply called reflectance, unless stated otherwise. To compensate possible tissue shift during measurements, an entire set of images was registered by horizontal and vertical translation.

Table 4.1 Exposure duration for Each Wavelength

Wavelength(nm)	400-440	460-680	700-830
Exposure(seconds)	10	2	1

4.3.4 Selection of Bundles

To measure bundle reflectance at different radii of the retinas, bundle areas were selected at distances of approximately 0.22 mm, 0.33 mm, and 0.44 mm (r_a, r_b, and r_c) from the center of the ONH, which was defined as the convergence point of nerve fiber bundles with the ONH (Figure 4.4). For each retina, two to three bundles were analyzed. Bundles from the same retina were separated by at least one major blood vessel to avoid repeat sampling of similar bundles in one retina.

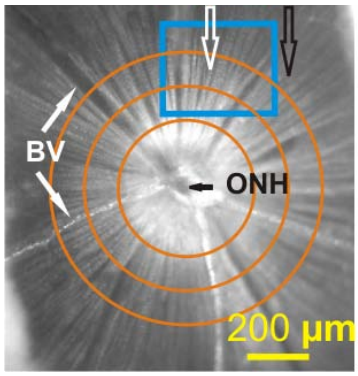

Figure 4.4. RNFL reflectance image of a normal retina. Bundle reflectance were measured at three radii of the retina (orange circles). White hollow arrow: on-peak measurement; black hollow arrow: off-peak measurement. BV: blood vessels; ONH: optical nerve head.

RNFL reflectance and its spectral pattern depend on measurement geometry. The bundles that were measured at on-peak or near-peak reflectance were selected for further data analysis (Figure 4.4). The incident and scattering angles for the measured bundle area were also calculated based on the geometry of light-scattering from a cylinder (described in section 4.1). In the experiments, the incident and scattering angles were estimated from the

orientation of a bundle's projection in an image and the positions of the light source and camera in the laboratory coordinate system. To ensure the comparability, only those bundle areas with incident and scattering angles varying within ±10° and ±15°, respectively, around their mean values were used for data comparison.

Both normal and glaucomatous retinas were used in this study.

4.3.5 Calculation of RNFL Reflectance and Comparison of Spectral Pattern

Reflectance measured on bundle areas included light reflected from the RNFL and its underneath tissue. It is reasonable to assume that the tissue underneath the RNFL is anatomically similar to the nearby gaps between bundles (Figure 4.5). The RNFL caused little attenuation to an incident beam due to weak scattering, thus we assumed that the reflectance from underneath tissue was approximately the same as that from nearby gap areas between bundles. To

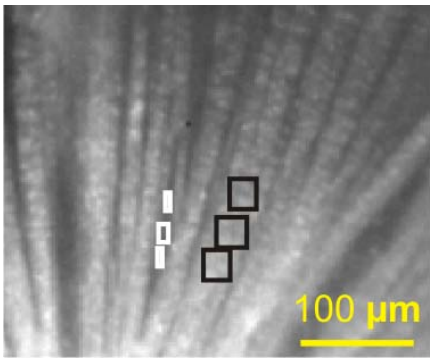

Figure 4.5. Calculation of RNFL reflectance. This is the enlarged image of the blue box in Figure 4.4. The reflectance (R) of the defined bundle areas (thick boxes) includes the reflectance of the bundle alone (R_{bundle}) and its underneath tissue ($R_{background}$). The reflectance of bundle alone is calculated as $R_{bundle} = R - R_{background}$, where $R_{background}$ is estimated from the average of nearby gap areas (thin boxes). Image taken at 660nm.

estimate the reflectance from RNFL alone, areas were chosen both on bundles and on nearby gaps between bundles. The reflectance of bundle alone could be calculated as the total reflectance measured on the bundle areas subtracts the average reflectance of gap areas (Figure 4.5) [9].

The RNFL reflectance depends on wavelength (Figure 4.2). To compare the pattern of RNFL reflectance spectra, the mean reflectance at wavelengths of 400 to 440 nm ($R_{400-440}$), 500 to 560 nm ($R_{500-560}$), and 740 to 830 nm ($R_{740-830}$) were calculated respectively. Reflectance ratios, calculated as relative reflectance at short and long wavelengths $\rho_s = R_{400-440} / R_{500-560}$ and $\rho_l = R_{740-830} / R_{500-560}$, respectively, were used to quantitatively compare reflectance spectra.

4.3.6 Evaluation of Axonal Cytoskeleton Damage

After reflectance measurement, retinas were fixed and processed for immunohistologic evaluation of axonal cytoskeleton. The immunohistologic staining and confocal microscopic imaging followed the developed procedure described in Chapter II.

In glaucomatous retinas, the appearance of bundles was arbitrary graded as normal appearance (G1), distortion of F-actin (G2), and distortion of all cytoskeletal components (G3) as described in Chapter II. G1 has the following characteristics: bundles appeared almost normal looking on en face images, strands of F-actin may start to condense; CS images showed the thickness was still in the normal range, however the texture was less condensed. In G2 stage, cytoskeletal components were distorted with less oriented structural organization viewed on en face images. Bundle boundaries of F-actin were hardly discernible.

The bundle thickness decreased significantly, and both en face and CS images showed that nuclei appeared in the RNFL. In G3 stage, there were discernible bundles. CS images showed there maybe 2 or 3 μm bundle thickness left.

4.3.7 Measurement of RNFL Thickness

To relate measured optical properties of the RNFL to its axonal cytostructure, the location of each nerve fiber bundle measured optically was identified in the corresponding confocal images. Briefly, the en face confocal image of a retina (Figure 4.6A) was registered onto the optical image of the same retina (Figure 4.6B) by matching the blood vessel patterns. The bundle areas that

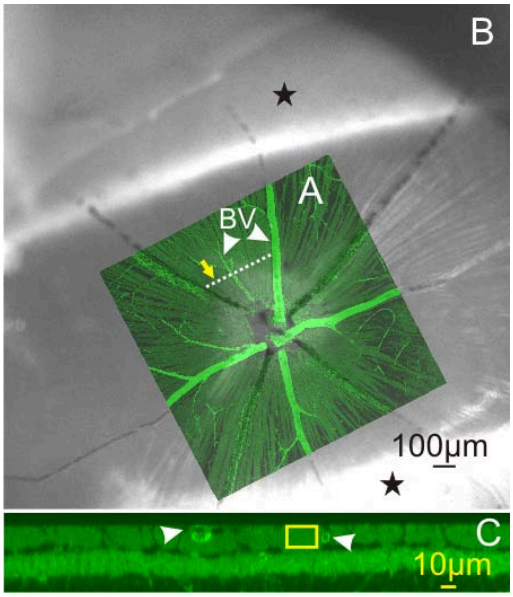

Figure 4.6. Image registration and measurement of RNFL thickness. (A) En face confocal image of a normal retina (40x objective). Bright stripes are retinal nerve fiber bundles with fluorescent stain of F-acin. The image is registered to the reflectance image of the retina in (B). Yellow arrow: a bundle area selected for data analysis. Dashed line: defined to derive a cross-sectional image across the selected bundle. (B) Reflectance image obtained at 440 nm. Black stars: Top mounting membrane for holding retina across the slit. (C) Cross-sectional image along the dashed line in (A). Bundle thickness was measured as the area between upper and lower boundaries divided by box width (yellow box). Arrow heads and BV: blood vessels.

were originally defined in the optical image were then marked in the confocal

image. The measurement of bundle thickness followed the procedure in Chapter II. A line across the area and perpendicular to the bundle was defined, and the cross-sectional image along the line was obtained from a reconstructed 3-D confocal image. Similar to the procedure described in Section 2.3.5, the thickness of the selected nerve fiber bundle was determined as the area between upper and lower boundaries divided by box width (Figure 4.6C).

To study the relationship between RNFL reflectance and thickness, linear regression was used to fit a scatter plot of bundle reflectance and thickness. The regression used a straight line $y = mx + b$, where y is reflectance, x is thickness in micrometers, the slope m is the proportionality constant between reflectance and thickness in units of reflectance per micrometer, and b is the y intercept representing a constant reflectance added to all points.

4.3.8 Data Analysis

Reconstruction of 3-D confocal image and measurements of RNFL reflectance and thickness were implemented with customized software (programmed in MatLab; The MathWorks, Inc. Natick, MA). Image registration was implemented in image-management software (CorelDraw Version 11; Corel Corporation, Ottawa, ON, Canada).

Reflectance ratios, ρ_s and ρ_l, between normal and treated groups, and bundle thickness were compared with a linear mixed-model analysis accounting for the correlation between multiple measurements made on the same retina and post hoc least-significant-difference tests. Incident angle and scattering angles were compared in an unequal variance t-test. The influence of treatment group

and bundle location on the proportionality constant, ρ_s, ρ_l was studied with the analysis of covariance formulation of the general linear model, which included tests of proportionality constant and group interactions (SPSS/PASW Statistics 18; IBM Corporation, Somers NY). The significance level was set at $P < 0.05$.

4.4 Results

Forty-one Wistar rats were treated unilaterally. The mean IOP increased from 11 ± 0.5 to 41 ± 8 mm Hg. The IOP of all treated eyes remained elevated for about 2 weeks. The cumulative IOP ranged from 87 to 311 mm Hg days with the mean of 152 ± 61 mm Hg days. Fifty-two bundles of 30 control retinas (OD) and 131 bundles of 41 treated retinas (OS) were examined for spectrum. The average incident angles were 16° ± 7° for both control and treated retinas; and the average scattering angles were 161° ± 11° and 162° ± 12° for control and treated retinas, respectively.

To analyze the change of relation between reflectance and thickness in early glaucomatous change, bundles were excluded if any cytoskeletal components appeared distorted in the confocal images. Bundles were measured in 11 control and 10 treated retinas to study the relation between the RNFL reflectance and thickness at early stages of glaucoma. Bundle thickness (mean ± SD) at each radius was compared between the control and treated retinas. There was no difference between the control and treated retinas ($P = 0.89$). However, in both control and treated groups r_a was significantly thicker than both r_b and r_c ($P < 0.001$), but r_b and r_c were not different from each other ($P = 0.10$). The incident and scattering angles were not different between the groups ($P > 0.6$),

with the average incident angles of 18° ± 6° and 19° ± 6° for control and treated retinas, respectively, and average scattering angles of 170° ± 6° for both groups.

4.4.1 RNFL Reflectance and Spectrum in Normal Retina

In the reflectance images of normal retinas, nerve fiber bundles appeared as bright stripes against a darker background (Figure 4.4, 4.5). Bundles were often separated by gaps between bundles. In this study, the reflectance of gaps was used to estimate the reflectance of the retinal tissue underneath the RNFL. For each selected bundle area, the mean reflectance of nearby gaps was calculated (Figure 4.5). Figure 4.7 shows the average reflectance of the gap

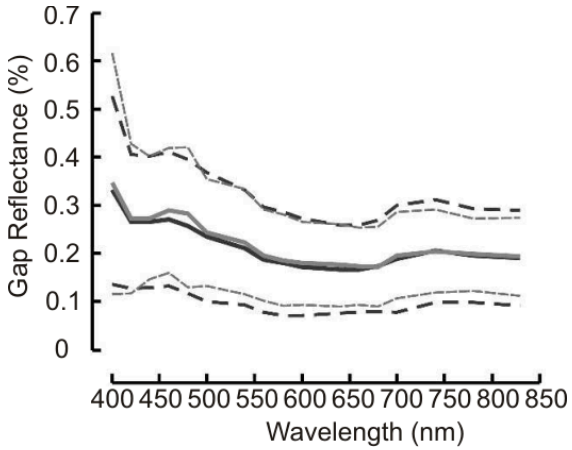

Figure 4.7. Reflectance spectra of gap areas are similar in normal (black line) and glaucomatous (gray line) retinas. Solid lines: average spectra of all gap areas defined for the bundles analyzed. Dashed lines: ± standard deviation. Reflectance value was calibrated with the diffuse white reflector.

areas change with wavelength for both normal and glaucomatous retinas. The spectra of gap reflectance in normal and treated retinas were similar. The reflectance of the gaps at any wavelength was not statistically different between the groups ($P > 0.5$).

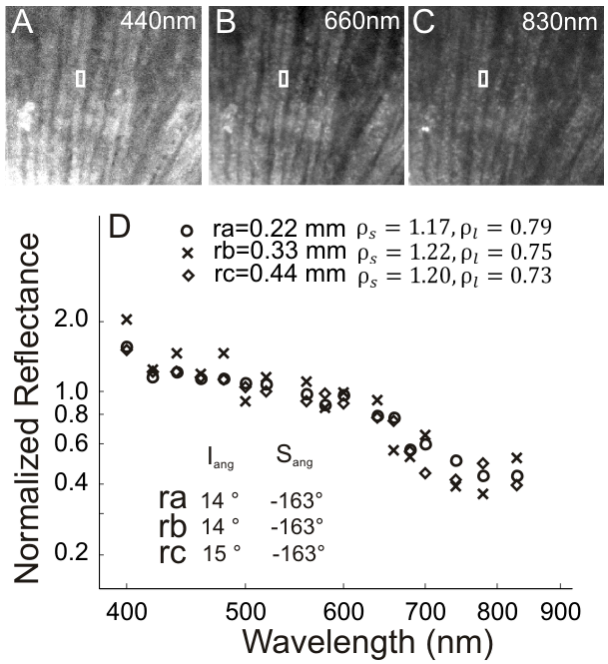

Figure 4.8. RNFL reflectance spectra in a normal retina. Reflectance of bundle areas was analyzed at radii of 0.22 (r_a), 0.33 (r_b), and 0.44 (r_c) mm from the center of the ONH. The reflectance decreases with increasing wavelength. The reflectance spectra are similar along the same bundle. I_{ang}, S_{ang}: incident and scattering angles.

Figures 4.8A-C show that RNFL reflectance appearance varies among wavelengths (at $r_c = 0.44mm$). At short wavelength (Figure 4.8A), bundles appeared smooth, and showed high intensity. With increasing wavelength (Figures 4.8B-C), the texture of bundles became less smooth. The intensity decreased compared to short wavelength, Figure 4.8D displays the RNFL reflectance spectra along the same bundle with the bundle areas defined at radii of 0.22 (r_a), 0.33 (r_b), and 0.44 (r_c) mm from the center of the ONH along the same bundle. To compare the patterns of RNFL reflectance spectra, each spectrum was normalized to its R500–560. The spectra were compared along the same bundle on 18 bundles; they have similar patterns along the bundle:

RNFL reflectance was high at short wavelengths and decreased with increasing wavelength.

To quantitatively compare patterns of RNFL reflectance spectra, reflectance ratios were calculated for each spectrum. Both ρ_s and ρ_l didn't change significantly along the bundles (P > 0.14) (ρ_s and ρ_l at different radii will be summarized later in Table 4.2.).

4.4.2 RNFL Reflectance and Spectrum in Glaucomatous Retinas

In retinas with mild glaucomatous damage, bundles still appeared as bright stripes against a dark background, but had lower contrast compared with normal bundles (Figures 4.9.A-B).

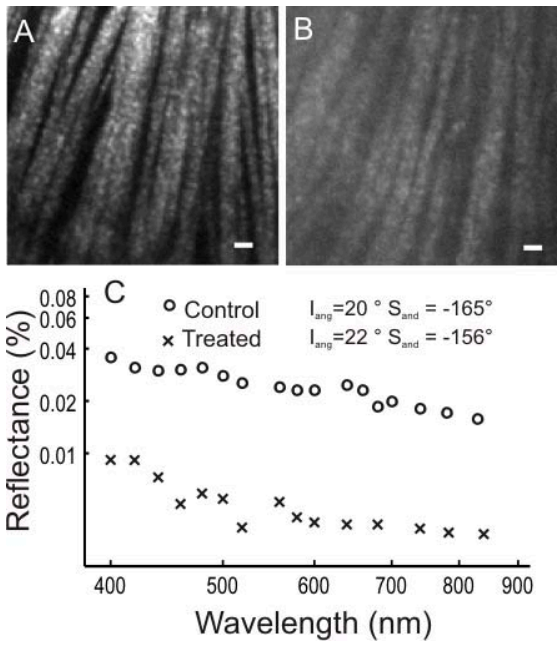

Figure 4.9. Reflectance images and spectra in control and treated retinas. (A-B): Reflectance image in control and treated retinas, respectively, at wavelength 660nm. (C): Reflectance spectra. Reflectance was derived from bundle areas near the ONH ($r_a = 0.22mm$) in control and treated retinas. Bundle reflectance of both retinas decreased with increasing wavelength. However, the reflectance of the treated retina was lower than the control at all wavelengths. Spectra were plotted on log-log coordinates. Scale bar: 20 um.

Glaucoma caused decrease of RNFL reflectance. Figure 4.9.C compares the reflectance spectra of bundles with similar thickness and similar geometric setting from control and treated retinas. The pattern of reflectance spectra was similar. However, the bundle reflectance in the treated retina was lower at all wavelengths.

Besides the lowered reflectance in the treated retinas, spectrum pattern was found changed differently in different retinas or even in the same retina. Figure 4.10 shows the reflectance spectra at different areas along the same bundle,

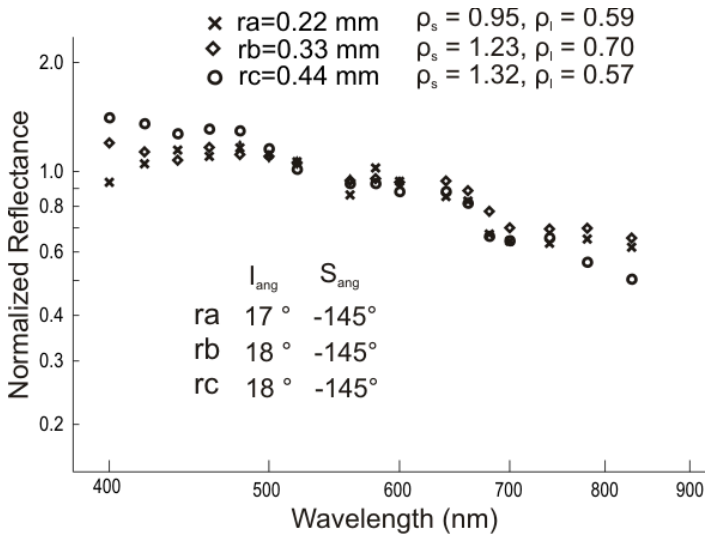

Figure 4.10. RNFL reflectance spectra along one bundle in a glaucomatous retina with normal-looking cytoskeleton. The slope of reflectance decrease at short wavelengths becomes shallower as the bundle area approaches the ONH. Reflectance spectra are normalized to the average reflectance at 500 to 560 nm and plotted on log-log coordinates. I_{ang} , S_{ang} : incident and scattering angles.

which had no apparent distortion of the cytoskeleton (G1). As the bundle area approached the ONH, the decline of reflectance with increasing wavelength became less steep. Such spectral change was often found in the bundles with normal-looking and slightly distorted cytoskeletons.

Changes in RNFL reflectance spectra were also found different in retinas with different degrees of cytoskeletal distortion. Figure 4.11 shows typical patterns of RNFL reflectance spectra in different damage degrees. For the bundle with normal-looking cytoskeletons (G1, Figure 4.11A), the reflectance spectrum had a similar pattern as in the control. For the bundle with F-actin

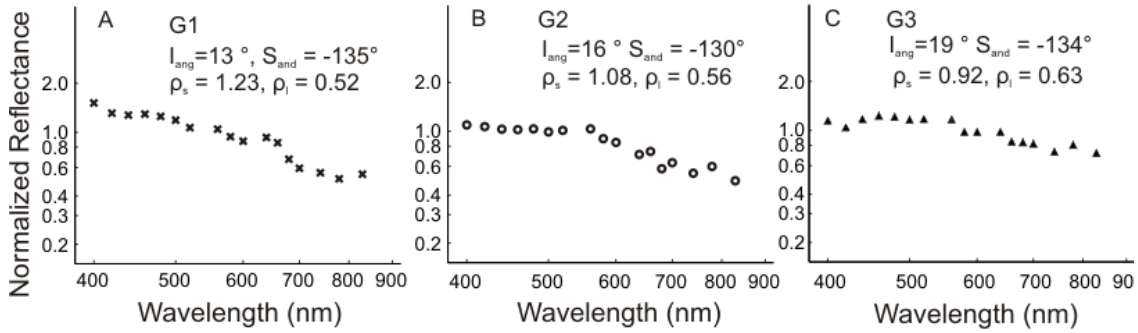

Figure 4.11. RNFL reflectance spectra of bundles with different degrees of cytoskeleton damage. (A) Normal-looking cytoskeleton. The spectrum is similar to the control. (B) Distorted F-actin. The spectrum has apparent change at short wavelengths. (C) Severely distorted cytoskeleton. The whole spectrum becomes flat. Symbols: measured reflectance. I_{ang} and S_{ang}: incident and scattering angles, respectively. ρ_s and ρ_l: reflectance ratios calculated from measured data points. Reflectance spectra are normalized to the average reflectance at 500 to 560 nm and plotted on log-log coordinates.

distortion (G2, Figure 4.11B), the reflectance spectrum was flatter in the short wavelength range compared with the control and Figure 4.11A. In the bundle with distortion of all cytoskeletal components (G3, Figure 4.11C), the entire spectrum flattened across all wavelengths. It is important to note, however, that bundles with distortion of all components were still visible in reflectance images and their reflectance was still directional.

4.4.3 Comparison of RNFL Reflectance Spectra in Normal and Glaucomatous Retinas

Quantitative comparison of reflectance spectra in retinas with different degrees of cytoskeletal distortion at different radii was summarized in Table 4.2.

Comparison of reflectance ratio along bundles shows that in retinas with normal appearance (G1), ρ_s is significantly higher at r_c than at r_b and r_a, and the ρ_s at r_c is similar to that in control group. However, ρ_s and ρ_l didn't change significantly with the distance to ONH center in G2 and G3 groups.

Viewed from another perspective, at near ONH (r_a), both ρ_s and ρ_l significantly changed in all glaucomatous groups comparing to control group ($P < 0.02$). At r_b and r_c, ρ_s and ρ_l in G1 group were similar to the one from control group while they significantly decreased in G2 and/or G3 groups ($P < 0.05$). The data also shows overall decreases of ρ_s with increasing cytostructural damage.

Table 4.2. RNFL Reflectance Ratios Comparison between Normal and glaucomatous Retinas at Different Radii

$\rho_s = R_{400-440} / R_{500-560}$	**Control**	**G1**	**G2**	**G3**
	1.27 ± 0.16	1.17 ± 0.14*	1.08 ± 0.14*	1.01 ± 0.23*
	1.27 ± 0.14	1.20 ± 0.17	1.11 ± 0.22*	1.10 ± 0.17*
	1.34 ± 0.22	1.28 ± 0.17	1.17 ± 0.25*	1.12 ± 0.19*
$\rho_l = R_{740-830} / R_{500-560}$	**Control**	**G1**	**G2**	**G3**
	0.61 ± 0.12	0.66 ± 0.08*	0.66 ± 0.13*	0.69 ± 0.10*
	0.62 ± 0.12	0.65 ± 0.11	0.62 ± 0.14	0.67 ± 0.11*
	0.58 ± 0.11	0.65 ± 0.09	0.69 ± 0.09*	0.66 ± 0.10*

* indicates statistically different from normal RNFL reflectance.

4.4.4 Relation between RNFL Reflectance and Thickness

The relation between RNFL reflectance and thickness was also studied at different radii of retinas. The bundle reflectance increases with increasing thickness for both control and treated retinas (Figure 4.12). But linear fitting of the data shows that the proportionality constant , which represented an average reflectance per micrometer thickness of the RNFL, of the treated group was significantly lower than that of the control ($P = 0.005$) at r_a = 0.22 mm, while the

fitted m is similar in control and treated group for r_b = 0.33 mm and r_c = 0.44 mm (P > 0.05).

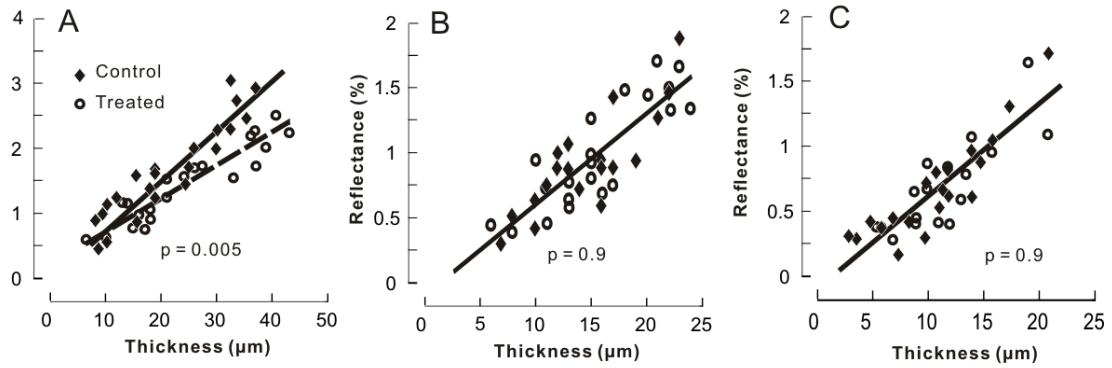

Figure 4.12. Relation between average RNFL reflectance at 500 to 560 nm and thickness. A) at $r_a = 0.22mm$; B) at $r_b = 0.33mm$; and C) at $r_c = 0.44mm$. The RNFL reflectance increased with increasing thickness. Linear regression parameters (± SE): A) $m = 0.07\% \pm 0.01\%/\mu m$ and $b = 0.04\% \pm 0.17\%$ with $R^2 = 0.85$ for the control group; $m = 0.05\% \pm 0.01\%/\mu m$ and $b = 0.21\% \pm 0.13\%$ with $R^2 = 0.84$ for the treated group. B) $m = 0.07\% \pm 0.01\%/\mu m$ and $b = 0.11\% \pm 0.17\%$ with $R^2 = 0.69$ for the control group; $m = 0.07\% \pm 0.01\%/\mu m$ and $b = -0.21\% \pm 0.16\%$ with $R^2 = 0.73$ for the treated group. C) $\mathrm{m} = 0.07\% \pm 0.02\%/\mu m$ and $\mathrm{b} = -0.19\% \pm 0.34\%$ with $\mathrm{R}^2 = 0.88$ for the control group; $\mathrm{m} = 0.07\% \pm 0.01\%/\mu m$ and $\mathrm{b} = -0.12\% \pm 0.14\%$ with $\mathrm{R}^2 = 0.77$ for the treated group.

Figure 4.13 summarizes fitted at different radii for different wavelengths. For the control retinas m was similar along bundles at any wavelength (P > 0.7). For treated retinas, the fitted m at bundle areas near the ONH was significantly lower than that of the corresponding control retinas at all wavelengths (P = 0.003, 0.005, and 0.02 for measured at 400–440, 500–560, and 740–830 nm, respectively). In contrast, in the peripheral regions (r_b and r_c) of the treated retinas was similar to that of the control at all wavelengths (P > 0.5).

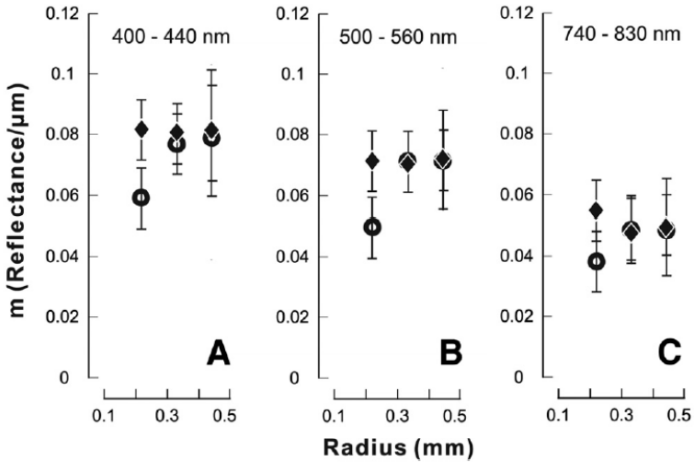

Figure 4.13. Proportionality constant m at different retinal locations and wavelengths. For the bundles near the ONH m decreased significantly in the treated retinas at all wavelengths. Diamonds: normal, circles: glaucoma. Vertical bars: ± SE of the fitting.

4.5 Conclusion and Discussion

The RNFL reflectance is very directional, so that the reflectance values of the RNFL depends on the geometric settings of reflectance measurements. On-peak measurements showed that RNFL reflectance was high at visible wavelengths and declined with increasing wavelengths. Reflectance spectra of the normal RNFL were similar along bundles. Similarity of spectra along bundles suggests that the underlying structure contributing to RNFL reflectance does not change very much along bundles in normal retina. We also found that RNFL reflectance was proportional to thickness, consistent with previous finding [3]. In normal retinas, it was also found that the proportionality constant did not change significantly along bundles, suggesting that the linear relation between reflectance and bundle thickness are similar along bundles.

RNFL reflectance spectra were changed in glaucomatous retinas. Reflectance ratios at the short wavelengths changed significantly along bundles

in early stage of glaucoma (G1). This could be explained as that structures that contribute to RNFL reflectance at short wavelength respond early to glaucomatous damage. With gradually increased damage in retinas, reflectance decreases were detected at any wavelength. These results indicate that change of RNFL reflectance at short wavelength is more sensitive to detect early glaucomatous damage. The finding also provides a possible explanation for the clinical observations that subtle RNFL defects can be identified by red-free fundus photography but not infrared OCT, which measures RNFL reflectance at 830 nm [42-47].

We also found that the decrease of bundle reflectance occurred early on bundle regions near the ONH but not the bundles farther from the ONH. The result suggests that nerve fiber bundles near the ONH are more vulnerable to damage caused by elevated IOP. The finding is consistent with the concept that the site of primary damage in glaucoma is at the ONH, one of the most often suspected sites damaged by IOP elevation. Measuring RNFL reflectance near the ONH may provide detection of glaucomatous damage at a time during which damage of ganglion cell axons is reversible.

Changes of RNFL reflectance spectra were found different in bundles with different degrees of cytoskeletal damage. Among treated groups, decrease of became more evident with increases in cytostructural distortion (Figure 4.11, Table 4.2). These results suggest that RNFL reflectance change is correlated with the degree of cytostructural damage. Hence, change of RNFL reflectance

measured by optical methods can reflect degrees of RNFL structural damage caused by glaucoma.

Glaucomatous damage causes decrease of RNFL reflectance. However, the reflectance of gaps did not change with the damage (Figure 4.7), which suggests that glaucomatous damage does not significantly change the scattering structure of retinal layers other than the RNFL. This result is consistent with the results reported by other groups that no apparent morphological changes in outer retinal layers of glaucomatous retina were found [60,115-117].

One of the goals of this study was to investigate reflectance change at early stage of glaucomatous damage. The bundles with no apparent distortion in any of these cytoskeletal components and thickness comparable to control groups were selected. The decrease of RNFL reflectance in treated group suggests that a change in RNFL reflectance occurred before the apparent change in axonal cytoskeleton and detectable thinning of the RNFL. This seems to conflict with the statement that reflectance arises from cytostructure, thus a change in bundle reflectance should relate to change in axonal cytoskeleton. Because reflectance of RNFL are determined by the distribution and relative refractive index of the RNFL ultrastructure, one possibility is that early glaucomatous damage changes the optical properties of extracellular and/or cytoplasmic constituents before distorting the cytoskeleton [118].

In summary, in glaucomatous retinas change of RNFL reflectance was wavelength dependent. Change of RNFL reflectance spectra varied along the bundle and with different degrees of glaucomatous damage. RNFL reflectance

decreases before cytoskeletal structural change and thinning of the RNFL. Measuring reflectance change in bundles near the ONH with shorter wavelength is a sensitive way to detect early glaucomatous damage, which may open a therapeutic window during which damage of axonal structure may be prevented.

4.6 Summary

In this study, we used an imaging microreflectometer (IMR) and in vitro retinas to study the reflectance of RNFL at different wavelengths and their changes in retinas with different degrees of glaucomatous damage. We also investigated the relation between the RNFL reflectance and thickness at early stages of glaucoma. The in vitro retinal preparations allow reflectance geometry being carefully controlled, and eliminate optical complications that cornea or lens may introduce.

We discovered that RNFL reflectance decreased in glaucomatous retinas and such change in RNFL reflectance was wavelength dependent. Early change of RNFL reflectance spectra happened in bundles near ONH and decrease of RNFL reflectance occurred first at short wavelengths. The results suggest that measurements of RNFL reflectance at short wavelengths and on bundles near the ONH provide early detection of glaucomatous damage. Moreover, we discovered that decrease of RNFL reflectance occurred prior to RNFL thinning and apparent cytoskeletal change. Hence, direct assessment of RNFL reflectance will provide more sensitive detection of glaucomatous damage.

Current clinical assessment of the RNFL is to measure RNFL thickness by detecting its reflectance at near infrared wavelengths. Our discoveries provide

important information to aid to develop a sensitive way to detect early glaucomatous damage and open a therapeutic window during which damage of axonal structure may be prevented.

The contribution of Ye Spector to this study was as follows:

- Improved tissue preparation method;
- Developed a procedure to register confocal images onto optical images;

Chapter 5. Reflectance Speckle of RNFL: a Reflection of Axonal Activity

5.1 Background

Retinal nerve fiber bundles are assembled axons of RGCs. In fundus images, bundles appear as smooth, highly reflecting stripes. In high resolution imaging, however, bundles are not smooth in reflectance images. Observed texture on bundles may be related to an optical phenomenon, called speckle. In this study, we investigated RNFL reflectance speckle and explore its relation to axonal dynamic activity.

5.1.1 Bio-Speckle

Speckles are caused by interference of coherent light scattered by particles in a medium [48,49]. A speckle pattern appears as randomly varied intensity distributing across an image plane (Figure 5.1). Biological materials are filled with

Figure 5.1. A speckle pattern. From C. Weber: Laser technique to screen embryo activity in barley seeds. http://wheat.pw.usda.gov/ggpages/BarleyNewsletter/50/ARGBNL50.htm

scattering particles, so speckled textures are often observed in biological tissues. Speckle produced from biological materials is called bio-speckle.

Biological tissues are usually dynamical structures. Movement of scattering particles within tissues will cause fluctuations in interference and thus change the interference pattern, producing temporal and spatial variations in the speckle

pattern [48,49,119]. The temporal change of bio-speckles is supposed to provide information about the physiological activity of living tissues. Currently, flowmetry based on temporal change of speckle has been developed to measure blood flow [48,120-123].

5.1.2 RNFL reflectance speckle

Often retinal nerve fiber bundles in reflectance images appear smooth structure. With high resolution and contrast imaging, bundles are not smooth looking. Drs. Knighton and Huang have discovered that the nerve fiber bundles had a speckled texture. They addressed the speckle as a variation source to optical methods that are used in clinical imaging of the RNFL [9]. Currently the speckle effect on the RNFL reflectance measurements is treated as a noise source and many numerical algorithms have been developed to remove speckle and improve image quality.

In our early studies of RNFL reflectance, RNFL reflectance was calculated as average intensity over bundle areas much larger than speckle size and, therefore, it eliminates spatial variation of intensity due to speckle. In contrast, to study RNFL reflectance speckle small bundle areas that include a few speckle patterns were defined as discussed later in this Chapter.

RNFL reflectance arises from light scattering of axonal ultrastructure [1,8]. Axons are dynamic structures. Interference of coherent light scattering by axonal ultrastructures should cause change of RNFL reflectance speckle. In this study, we studied temporal change of RNFL reflectance speckle and related change of RNFL speckle to axonal dynamic activity.

5.1.3 Axonal Transport

Axons are dynamic structures. They transport molecules, vesicles and organelles in both anterograde (towards axon terminal) and retrograde directions (towards cell body). It is achieved by binding the so-called cargo (molecules, vesicles and organelles) to molecular motors. The cargo and motor form a motor-cargo complex, which generate movement along axons [53,124]. Most of motor-cargo complexes use MTs as the track to move bi-directionally.

Anterograde transport is subtyped into fast and slow transport with the fast transport occurring at a rate of 0.58 – 4.63 μm/seconds and slow transport at a rate of 0.0035 – 0.09 μm/seconds. Retragrade transport is achieved by cargo-motor complexes moving along either MTs or actin-spectrin meshwork with a rate ranging from 2.31 μm/seconds to 4.62 μm/seconds [125,126].

Table 5.1 Summary of Axonal Transport

Axonal Transport	**Fast (μm/seconds)**	**Slow (μm/seconds)**	**Mechanisms**
Anterograde	0.58 – 4.6	0.0035 – 0.035 0.02 – 0.09	Kinesins as a molecular motor generate movement along the microbulues running down the axon
Retrograde	2.3 – 4.6		It uses dymein as the molecular motor. The faster retrograde transport uses MTs. For the slower retrograde transport, the dynein is associated with actin-spectrin meshwork within the axon, rather than the MTs.

5.2 Purpose and Hypothesis

Currently the reflectance of the RNFL is often used to assess RNFL structure, such as RNFL thickness. Reflectance measurements are implemented with static imaging of the RNFL. Interference of coherent light scattering by particles in axons results in the phenomenon of speckle. The axons of RGCs are dynamic structures. The movement of scattering particles within axons would cause fluctuations in interference and thus change the interference pattern, producing temporal and spatial variations in the speckle pattern. We hypothesized that dynamic activity of axons causes change of RNFL reflectance speckle. In this study, we investigated speckle phenomenon in RNFL reflectance and explored the possibility of assessing axonal dynamic activity by measuring temporal change of the RNFL reflectance speckle.

5.3 Formation of Reflectance Speckle and Imaging Microreflectometry

Speckle happens when the difference of the optical path of scattered light is greater than the coherence length of an incident beam. Under monochromatic illumination, there is a coherence volume from within which scattered rays can interfere at any given point. With quasi-monochromatic illumination, the coherence length of the light source determines the volume of coherence while the spatial coherence is not important. The coherence length is calculated as

$$L = \frac{2\ln(2)}{\pi n}\frac{\lambda^2}{\Delta\lambda} \qquad (5.1)$$

with λ as illumination wavelength, n as refractive index , $\Delta\lambda$ as the wavelength bandwidth . The diameter of the coherence disc is calculated as

$$d \approx 0.16\,\lambda/\alpha \qquad (5.2)$$

with α as the divergence angle of the illumination beam.

Speckle size, which solely depends on an imaging system, is calculated as [49]

$$S = 2.44\,\lambda\,(1+M)\,F \tag{5.3}$$

where M is the camera's magnification in air and F is the f-number of an objective lens.

The IMR described in Chapter 4 has the CCD chip of the camera that has 1024 × 1024 pixels with each pixel size of 13 ×13 μm. The camera with an f-number of 3.6 provides a magnification of 8 in aqueous medium and 6 in air, and has a full field of view of 2.3 × 2.3 mm on the retina with a digital resolution of 2.2 μm/pixel. The interference filter with 10 nm bandwidth was used to filter the light from a tungsten-halogen lamp and provide mono-chromatic illumination with divergence angle of 2.86°.

Figure 5.2 shows a schematic drawing of coherence volumes in the RNFL.

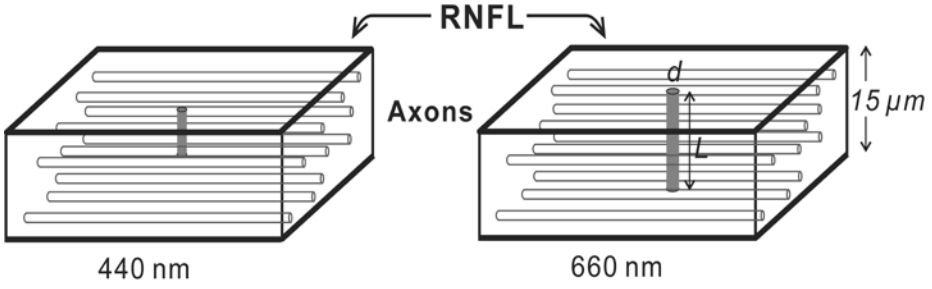

Figure 5.2. Coherence volumes at different wavelength in the RNFL. Rays scattered at points within a coherence volume (gray cylinder) can produce interference effects. The size of a coherence volume increases with increasing wavelength.

The refractive index of the retina n is 1.35. The coherence length at each wavelength was calculated by Eq. 5.1 and given in Table 5.2. In normal rat retinas, RNFL thickness ranges from 5 μm to 40 μm. In our studies, the thickness

of selected bundles for the optical study was around 15 μm. The calculation in Table 5.2 shows that the coherence length increases with wavelength. For wavelengths from 400 nm to 520nm, the coherence length is shorter than the thickness of thick bundles, resulting in speckles superimposed on the average reflectance; for wavelengths from 660nm to 830nm, rays from approximate the whole bundle thickness contribute to the bundle speckle.

Table 5.2 Coherence Lengths at Each Wavelength

λ (nm)	$L = \frac{2\ln(2)}{\pi n}\frac{\lambda^2}{\Delta\lambda}$ (μm)
400	5.2
440	6.3
520	8.8
660	14
780	20
830	22

Speckle size varies with wavelength (Eq. 5.3). Table 5.3 lists speckle sizes, at each wavelength for the IMR. For λ at 660 nm, the IMR provides a speckle size of 41 μm in free space, or a speckle of about 3 pixels wide (7 μm) in an image. Considering the speckle size on image and coherent length relative to the RNFL thickness, wavelengths from 660nm to 830 nm are ideal for RNFL speckle measurement with the IMR.

Table 5.3 Speckle Sizes in Each Wavelength for IMR

λ (nm)	S in free space (μm)	S in an image (μm)	speckle size as # of pixel width
400	25	4.2	1.9
440	27	4.6	2.1
520	32	5.5	2.5
660	41	6.8	3.1
780	48	8.1	3.7
830	51	8.6	3.9

M = 6 and F = 3.6 for the IMR.

5.4 Experimental Materials and Methods

5.4.1 Tissue Preparation

Speckle phenomenon on RNFL reflectance is a new research idea and there was no experiment or study been done according to the author's best knowledge. The effects of other ocular tissues, such as cornea and lens, on the optical properties of RNFL are still unknown. To eliminate these complications, isolated retinas were used. To maintain its normal physiological activity, retina was kept in warm oxygenated physiological solution. Tissue preparation followed the developed procedures described in Chapter 2 and Chapter 4.

5.4.2 Experimental Design

In this study, experiments were designed to achieve two goals:

Goal 1: To investigate physical factors that may affect measurement of RNFL reflectance speckle. These physical factors include: imaging system geometric settings, exposure duration and wavelengths.

RNFL reflectance is very directional and is confined in a conical sheet concentric with the bundle axis. Speckled texture observed in RNFL reflectance images could depend on the geometric settings of the light source and camera. Effect of imaging geometric settings on speckle measurement was studied by changing camera's azimuth and light source's azimuth and elevation as described in Chapter IV.

Change of speckle pattern is associated with the dynamic activity of axons. To catch the activity without losing information, camera's exposure time is important to be set in a reasonable range. Different exposure durations were tested in studying temporal change of RNFL speckle.

We have observed speckled textures on RNFL reflectance images at long wavelengths. With decreasing of wavelength, the appearance of speckle becomes less apparent. We investigated if temporal change of RNFL speckle also depended on wavelength.

Goal 2: To test the hypothesis that temporal change of RNFL reflectance speckle is associated with axonal dynamic activities.

To achieve this goal, we used experimental manipulation to alter physiologic conditions of the retina and compared temporal changes of RNFL speckle before and after the manipulation. Retinas with known physiologic conditions include: normally prepared living retina, fixed retina, retina perfused at lower temperatures and retina treated with colchicine, a microtubule (MT) depolymerizing agent.

In fixed tissues, axonal activities were stopped, and scattering structures were expected to remain stationary, thus speckle pattern was supposed to not change with time.

Because low temperature slows axonal transport [127] and other physiological processes, the temporal change of RNFL speckle was predicted to be slower than in normally prepared living retinas.

MTs are a key cytostructure for transferring proteins and cellular components along the axons [124-126], it is postulated that depolymerization of MTs would hamper axonal transport and thereby reduce temporal change of RNFL reflectance speckle.

5.4.3 Measurement of RNFL Reflectance Speckle

i. General Measurement Settings:

In normally prepared retinas, nerve fiber bundles were oriented approximately vertically, and the camera and light source were adjusted to the positions that give maximum (on-peak) reflectance of the nerve fiber bundles, with a dark and uniform background. To study temporal changes of a speckle pattern, a series of reflectance images at 660nm are collected every five seconds for about 15 minutes. Exposure duration was set to 2 seconds. The selection of wavelength 660nm have been discussed in Section 5.3, the reason for selecting exposure duration of 2 seconds will be discussed later in this section. Black images taken with the same exposure duration, but with the light source off, were subtracted from each image, to compensate for the dark current and bias level of the CCD. To compensate for possible tissue shift during the measurement, the entire set of images was registered by horizontal and vertical translation.

ii. Measurement Settings for **Goal 1**

To study the effects of geometric setting of the system on the measurements of RNFL reflectance speckle, image series were taken at 660 nm with 2 seconds exposure duration. The first image series was taken when the camera and light source were set to give near maximum (on-peak) reflectance measurement for the studied bundles. Then the light source probe was adjusted until noticeable reduction of reflectance and image contrast on studied bundles happened (partially off-peak). Note that at this setting, bundles were still perceivable. At the last setting, image series was taken when the studied bundles were just disappeared and appeared similar to background (off-peak). Between

the image series, the camera and tissue positions were not changed to ensure that bundles in images were not shifted.

According to Table 5.1, fast axonal transport rate ranges from 0.58 – 4.6 μm/seconds and slow one ranges from 0.0035 – 0.09 μm/seconds. The motor-cargoes moving along axons take 0.5 seconds to 3.8 seconds for fast transport and 25 seconds to 629 seconds for slow transport to cross a pixel which is 2.2 μm in the IMR. With the hypothesis that change of speckle pattern is consistent with the rate of axonal transport, speckle texture measured with different exposure durations may reveal the roles of fast and/or slow axonal transports. With exposure duration shorter than 0.5 seconds, the temporal change of speckles should reveal both fast and slow axonal transport.

To keep the measurement in a reasonable period of time, long exposure duration was not favored in this study (such as 25 second). We have chosen compromised exposure duration of 2 seconds. The temporal change of speckle reflects the mechanisms of axonal transport slower than 1.1 μm/seconds while rapidly changed texture that is associated with faster activities is averaged out.

In this study, we tested exposure duration of 0.5 sec and 2.0 sec for the effect of exposure duration on temporal change of RNFL speckle. The IMR was set to measure on-peak reflectance at 660 nm. An image series was taken with 2 sec exposure followed by another series with 0.5 sec exposure.

To study the effect of wavelength on the measurement of reflectance speckle, the reflectance speckle was measured at 520nm, 660nm, and 830nm, with on-peak reflectance measurements and exposure set to 2 sec.

iii. Measurement Settings for **Goal 2**

For all studies with tissue manipulation, reflectance image series were taken at 660nm with on-peak reflectance and 2 seconds exposure every five seconds for about 15 minutes.

In experiments with normally prepared retinas, mounted retina was kept in a chamber perfused with an oxygenated physiological solution with temperature maintained at 34°C to keep the tissue alive. Three image series were taken at around 30 min, 60 min and 90 min after the optical nerve was cut off from the eyeball.

In an experiment with a fixed retina, a mounted retina was fixed with 3% paraformaldyhyde for 40 minutes at 34°C and thoroughly rinsed with physiologic solution. The retina was then placed in the chamber and speckle measurements followed the procedures identical to that for a normal living retina.

For living retina treated with lower temperature, a retina was prepared as usual and placed in chamber perfused with normal oxygenated warm (34°C) physiological solution. Image series at 660nm with 2 seconds exposure were taken every five seconds for about 15 minutes. Then the temperature of the physiological solution was gradually lowered from 34°C to 24°C and then maintained at 24°C. A second image series was taken immediately with 24°C physiological solution temperature.

For retina treated with colchicine, an experiment included a baseline period during which the chamber was perfused with a solution containing no colchicine. The solution was then switched to a solution containing 10mM colchicine. The regular solution was gradually replaced with the colchicine solution. The retina

was then fully perfused and treated with the colchicine solution. The baseline, switching and treatment periods last about 30 min, 15 min and 40 min, respectively. Two to three sets of image series were taken in both baseline period and treatment period with wavelength of 660 nm and exposure of 2 sec.

5.4.4 Quantification of Dynamics of RNFL Speckle and Bundle Selection

Speckles are a random pattern of light interference; in RNFL reflectance images, speckles appear as clusters of bright and dark pixels with sizes given by Equation (5.1) (Figure 5.3). The speckle texture did not stay in the same place rather changed with time. To quantify the time variation of textured speckle, image series was taken every five seconds for about 15 minutes. A correlation function was used to analyze dynamic change of speckle patterns on bundles. In this method, a rectangular area was defined containing speckled texture on bundle and treated as a subimage. A series of such subimages were derived from the original full image series. Correlation coefficients (CC) between the first subimage and each consecutive subimage in the entire image series were calculated as

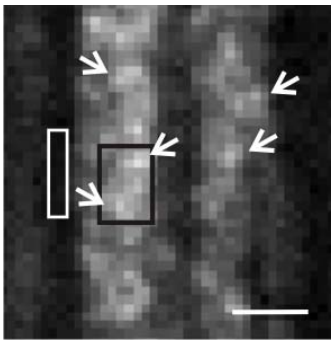

Figure 5.3. Reflectance Speckle of RNFL. Wavelength: 660nm. Arrows show individual speckles. Black box: defined bundle area; white box: defined gap area. Scale bars: 20 μm.

$$CC_I = \frac{\sum_m \sum_n \left(A_{mn} - \bar{A} \right)(I_{mn} - \bar{I})}{\sqrt{\left[\sum_m \sum_n (A_{mn} - \bar{A})^2 \right] \left[\sum_m \sum_n (I_{mn} - \bar{I})^2 \right]}} \quad (5.4)$$

where A_{mn} was the intensity of the m th row and n th column element in the reference subimage with a typical value of seven to nine for m and n, $\bar{A}$ was the mean intensity of the A_{mn}, and I represented the I th subimage in the image series [128]. A high CC indicates high similarity between two images (i.e. selected speckle patterns). CC equals one for identical images. CC_I was calculated for each subimage and plotted verse time. The time course was then fitted with an exponential function, and the time constant of the function was used as a measure of dynamic change of speckle. The same analysis was also applied to a nearby gap area (white box in Figure 5.3).

To compare the time courses among bundles, bundle areas were defined at several different bundles with on-peak measurements. To compare the time course along bundles, several bundle areas were defined along the same bundle, with on-peak reflectance. To compare time courses measured at different times, time courses of the same bundle area were obtained.

For retinas treated with lower temperature or colchicine, time courses from the same bundle area with on-peak measurement were compared; time constants were statistically compared with paired T-test for means between before and after treatments.

For any paired experiments, the fitted time constants were statistically compared with paired T-test for means. The significance level was set at $P < 0.05$.

5.5 Results

5.5.1 Speckle Phenomena in RNFL Reflectance

To appreciate speckle phenomena in RNFL reflectance, isolated rat retinas were used. Reflectance images were collected at wavelengths of 440, 520, 660nm, and 780 and 830nm with exposure fixed at 2 seconds.

In RNFL reflectance images, retinal nerve fiber bundles appeared as bright stripes against a darker background. Figure 5.4A is an in vitro living retina image taken at 660 nm. With magnified view of the bundles (Figure 5.4B), the bundles show speckled texture, which is randomly distributed within the bundles with a speckle size of approximately 3 pixels wide.

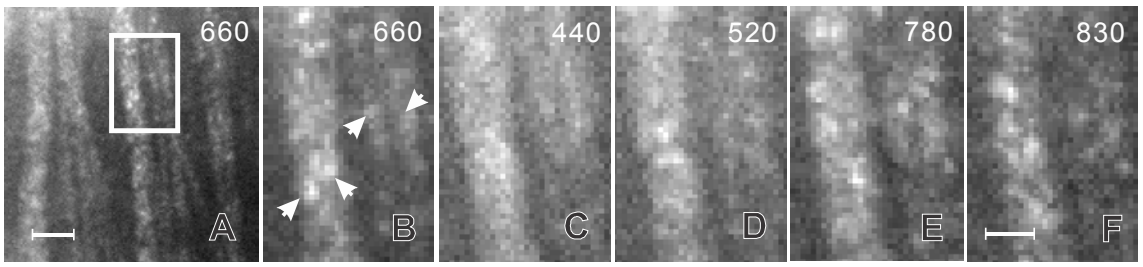

Figure 5.4. Reflectance Speckle of RNFL at different wavelengths (A) Reflectance image taken at 660 nm; (B – F) magnified view of the bundles outlined in (A). Arrows in (B) show individual speckles. Scale bars: 50 μm (A) and 20 μm (B – F).

As calculated by Eq. 5.1 and 5.3, the coherence length and speckle size vary with wavelength. The appearance of speckle is also dependent on wavelength [9,49,123]. Figures 5.4C – F show the same bundles in Figure 5.4B imaged at different wavelengths. With increase of wavelength, the speckled texture became more apparent with increasing contrast; Figure 5.4F shows that

at 830 nm bright pixels clustered to form high-contrast speckles. Note that all images in Figure 5.4 had the same exposure duration of two seconds.

5.5.2 Temporal Change of RNFL Reflectance Speckle

In living retina the speckle pattern was not stationary. With the lapse of time, RNFL speckles in an image series appeared and faded but did not move along

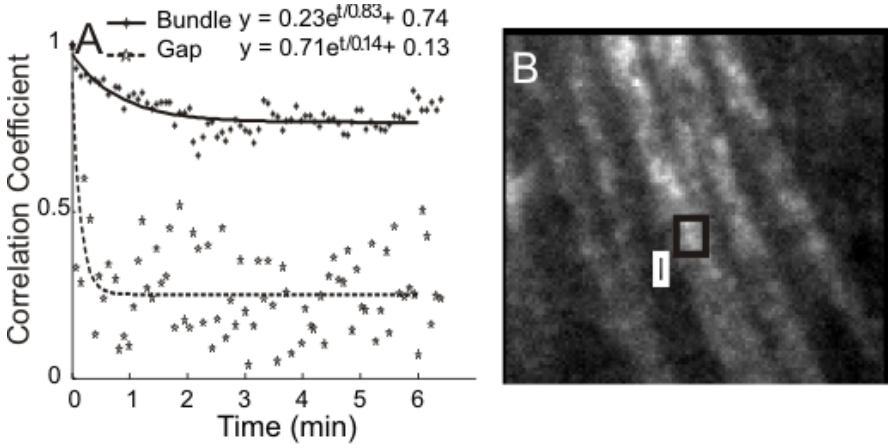

Figure 5.5. Correlation coefficient (CC) time courses of living retina. (A) CC of bundle and gap areas defined in (B) in a living retina. The time courses of bundle and gap are fitted with an exponential function. Black and white boxes: bundle and gap areas for the plots in (A). Scale bar: 20 μm.

bundles. To compare the similarity of a speckled pattern over time, a correlation function analysis was applied to an image series. Figure 5.5A shows a correlation coefficient (CC) time course of a series of subimages, which sampled two speckles in a normal living bundle. The CC was high at the beginning of the image series, but decreased gradually with time and after about two min reached a plateau. In contrast, the CC time course of a nearby gap area shows that CC decreased immediately and varied around a value over the entire time period. An exponential function fitting gave $\tau = 0.83$ and $\tau = 0.14$ min for the bundle and gap areas, respectively. Thirty-six bundles from thirteen living retinas show similar

results with τ = 1.29 ± 0.53 min (mean ± s.d.) and ranging from 0.49 to 2.43 min. For the corresponding gap areas τ = 0.09 ± 0.11 min.

To rule out that the change observed in our experiments was due to circulation of the physiological solution, image series were taken with the circulation halted. The gradual change of speckle pattern persisted.

5.5.3 Effect of Physical Factors on Measurement of Reflectance of Speckle

i. Effect of Geometric Setting of Imaging System on RNFL Speckle Measurement

To study the effect of geometric setting on RNFL reflectance speckle, the reflectance speckle was measured on-peak and off-peak at the same bundle areas with 2 seconds exposure duration. Figure 5.6 shows CC time courses of speckle measured on-peak, slightly off-peak and totally off-peak. With on-peak reflectance, CC decreased with time and reached a constant in about 3 min

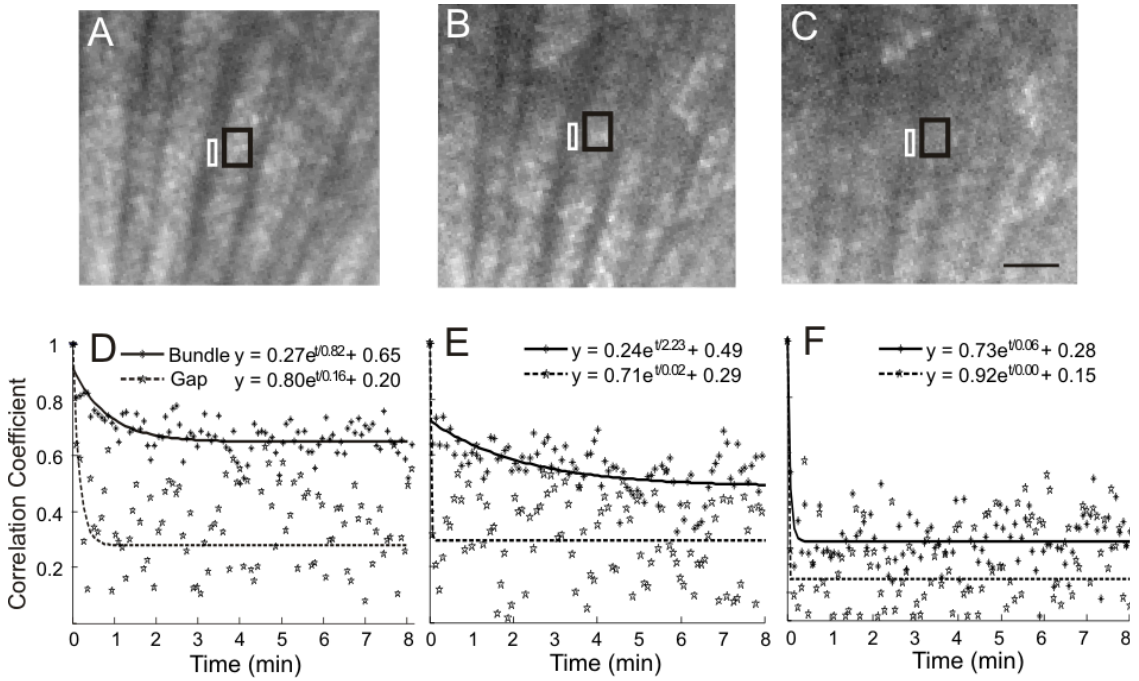

Figure 5.6. Correlation coefficient (CC) time courses of on-peak (A, D), slightly off-peak (B, E) and totally off-peak (C, F) measurements. (D-F) CCs of the same bundle area (black box)) and gap area (white box) defined in (A-C) and fitted with exponential function. Iang and Sang: A) 23°, -177° B) 20°, -179° C) 16°, -178°. Scale bar: 20 μm.

(Figure 5.6D). The time course of speckle measured slightly off-peak (Figure 5.6B, E) also shows high CC at the beginning, then gradually decrease to a plateau, similar to that of on-peak measurement (Fig 5.6A, D). However, the change of CC became much slower with τ = 2.23 min, comparing to the on-peak measurement with τ = 0.82 min. When measured totally off-peak (Figure 5.6C), CC dropped immediately with the CC time course of bundle similar to that of nearby gap (Figure 5.6F).

This experiment shows that CC time course measurement of RNFL speckle is dependent on imaging system geometric settings. Due to different orientation and possible tissue tilt, not all bundles in an image were in on-peak measurements. In all the RNFL speckle studies presented hereafter bundles with on-peak measurements were selected and used in data analysis.

ii. Effect of Wavelength on RNFL Speckle Measurement

Speckle appearance is dependent on wavelength as shown in Figure 5.4. However, the dynamics underlying temporal change of RNFL speckle should not depend on wavelength. Normally prepared retinas were used and bundles with on-peak measurements were selected for data analysis. Figure 5.7 show the CC time courses of the same bundles measured at 520 nm, 660 nm, and 830 nm. The CC time courses at all wavelengths showed high CC at the beginning, then gradually decreased to a plateau and varied around it hereafter. The time constants from exponential function fitting were different at measured wavelengths in this retina. However time constants measured from 4 retinas shows that there is no significant difference among wavelengths by paired T-test

for means. The mean τ at 520 nm, 660 nm, and 830 nm were 1.23 ± 0.2, 1.36 ± 0.41, and 1.12 ± 0.5, respectively.

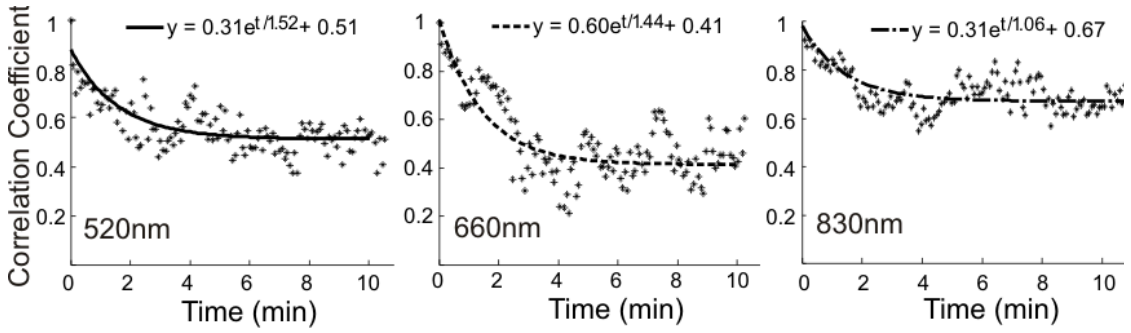

Figure 5.7. Correlation coefficient (CC) time courses at wavelength of 520 nm (A), 660nm (B) and 830 nm (C).

This result shows that the measurement of RNFL did not depend on wavelength. Considering the speckle size on image and coherent length relative to the RNFL thickness, we used wavelength of 660 nm in all the RNFL speckle studies presented hereafter.

iii. Effect of Exposure Duration on Measurement of RNFL Speckle

To investigate the effect of exposure duration on measurement of RNFL speckle, 0.5 seconds exposure was used to take image series at the same bundle area following the 2 second exposure image series, with on-peak reflectance measurement. The speckled texture measured with 0.5 seconds exposure (Figure 5.8B) shows more noise than the one with 2 seconds exposure (Figure 5.8A). CC time courses with both exposures showed decrease of CC with time. However, CC decreased faster in image series with 0.5 sec exposure as shown in Figure 5.8C-D. Exponential function fitting gave a shorter τ =0.43 min for 0.5 seconds exposure (Figure 5.8D) than the one with 2 seconds exposure (τ =1.27 min) (Figure5.8C). Paired measurements were taken on 5 retinas, and paired T-test for means shows that time constant with 0.5 seconds exposure (τ =

0.43 ± 0.4 min) is significantly shorter than the one with 2 seconds exposure (τ = 1.03 ± 0.75 min) ($p < 0.05$).

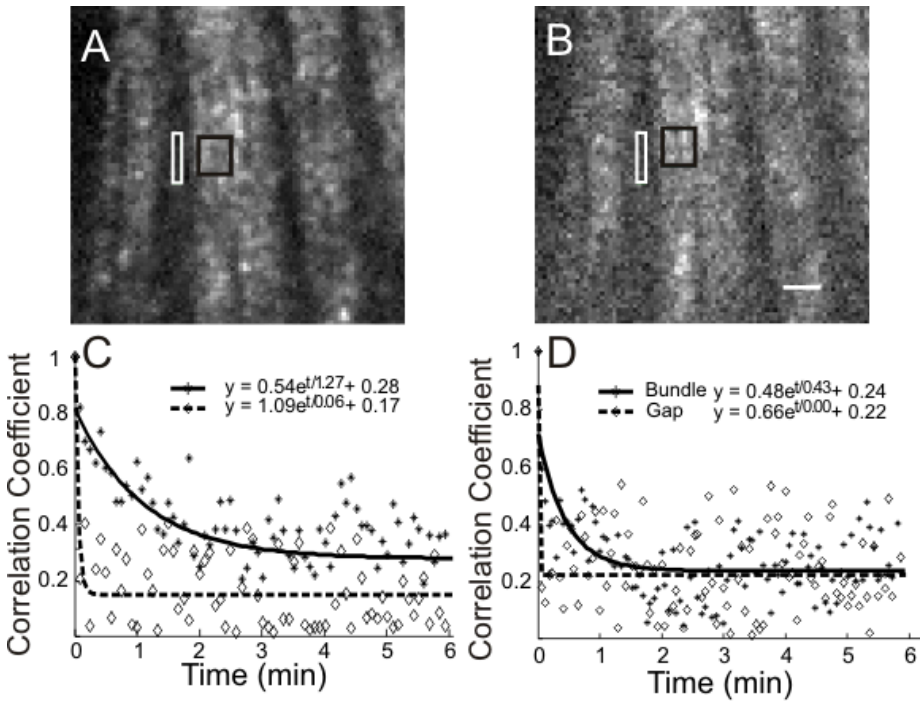

Figure 5.8. Correlation coefficient (CC) time courses of speckle measured with 2 seconds exposure (A, C) and 0.5 seconds exposure (B, D) with fitting. (A-B) Speckle measured with 2 seconds and 0.5 seconds exposure of the same retina, respectively. (C-D) CCs of a bundle area and a gap area defined in (A-B) and fitted with exponential function. Black and white boxes: bundle and gap areas for the plots in (C-D), respectively. Scale bar: 20 μm.

This result indicates that speckle patterns decorrelated faster with exposure of 0.5 seconds than with exposure of 2 seconds. This may be explained by that in dynamic activities caught by 0.5 seconds exposure, scattering particles move out of the defined bundle area faster than the one by 2 seconds exposure. The result suggests that temporal change of RNFL reflectance speckle measured with different exposure duration may reveal different axonal dynamic activities.

The purpose of this study was not to study different activities, rather to explore the concept that RNFL reflectance speckle was associated to axonal activity. Hence only one exposure duration was used for all the studies presented

thereafter. The CCD camera in our IMR has non-linear response when exposure duration is short than 0.7 sec and therefore, exposure duration of 2 second was used.

iv. Effect of Tissue Preparation on Measurement of RNFL Speckle

In this study, in vitro retinas with optical nerve cut off were placed in a chamber perfused with an oxygenated warm physiological solution to maintain the tissue alive. The mechanic injury may alter the physical activities of axons. However, we expected that such alteration was stable in the condition of well-maintained tissue perfusion. To test the stability of tissue preparation during the time period RNFL speckle were measured, three to six image series were taken in separated time points over a period of 100 min. Figure 5.9 shows time courses of the same bundle area taken at 25 min (Figure 5.9A), 70 min (Figure 5.9B) and

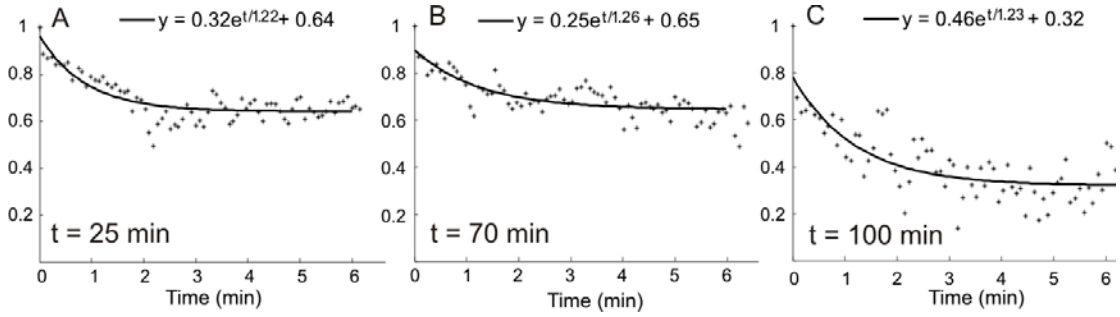

Figure 5.9. Correlation coefficient (CC) time courses of speckle of the same bundle area at different times with fitting. (A-B) Speckle measured at 25 min, 70 min and 100 min after the optical nerve was cut off from the rat, respectively. The correlation coefficients were lower in (C), however the fitted time constant was similar to (A) and (B).

100 min (Figure 5.9C) after the optical nerve was cut off from the rat, respectively. The fitted time constants were similar at different time points; however, the CC value of the image series taken 100 min after the optical nerve was cut off, decreased to a lower plateau comparing to the ones of 25 min and 70 min after.

The value of plateau in CC time course was related to average intensity of the image [129]. A lower plateau indicates scattering particles may have changed 100 min after optical nerve cut off. Therefore, our experiments measured speckle image series within 70 min of the tissues prepared.

In summary, we have determined that the measurement of CC time course of RNFL speckle does not dependent on wavelength, but does vary with geometric setting of imaging system, and imaging exposure. We also showed that the dynamic activities were still stable after 70 min of tissue preparation.

To test the hypothesis that temporal change of RNFL reflectance speckle was associated with axonal dynamic activity, we used 660 nm and 2 sec exposure to take images. Image series were taken within 70 min of tissue preparation. Bundles measured with on-peak reflectance were selected for data analysis.

5.5.4 RNFL Speckle in Retinas Treated With Low Temperature and MT Depolymerization

To confirm that measured decrease of CC of bundle speckles associates with axonal dynamic activity, image series were taken on fixed retinas yet perfused with a warm physiologic solution as used for a normal living retina. Speckled texture of fixed nerve fiber bundles was also apparent in its reflectance images (Figure 5.10B); however, the speckle patterns did not vary with time as Figure 5.10A shows high values of CC over the entire time period. In contrast, the correlation of nearby gaps was similar to that of living tissues (Figure 5.10A).

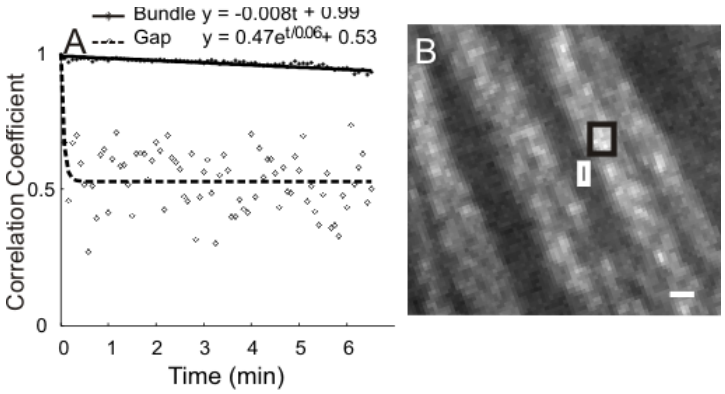

Figure 5.10. Correlation coefficient (CC) time courses of fixed retina. (A) CC of bundle and gap areas defined in (B) in a fixed retina. The time course of bundle is fitted with a linear function and time course of gap is fitted with an exponential function. Black and white boxes: bundle and gap areas for the plots in (A). Scale bar: 20 μm.

To further confirm that the measured temporal change of RNFL reflectance speckle was associated with axonal dynamic activity, the temperature of the physiologic solution was lowered from 34°C to 24°C, with the expectation that lower temperature would slow axonal transport [127]. Three retinas were used in this experiment. Image series of the same bundle area were analyzed at 34°C and the followed 24°C. The results from one of these retinas are shown in Figure 5.11. At 34°C the change in speckle was similar to other retinas, with τ = 1.61

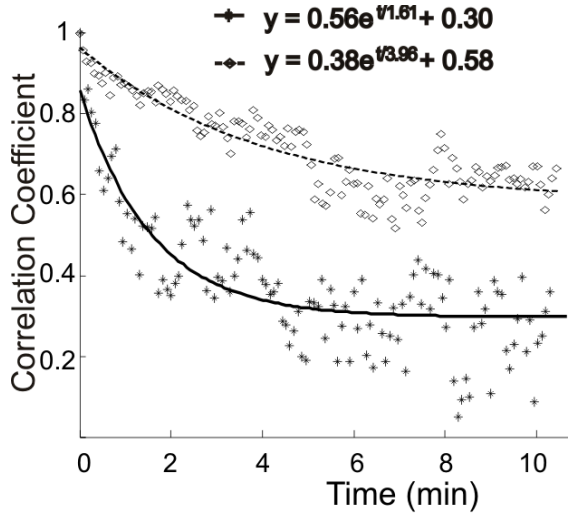

Figure 5.11. Effect of temperature on temporal change of RNFL speckle. star: a typical CC time course of a retina perfused at 34°C; diamond: a CC time course of a living retina perfused at 24°C.

min. At 24°C, however, the change in speckle slowed by a factor of nearly 2.5 to τ = 3.96 min. A paired T-test for means analysis showed that τ of the fifteen bundles from the three retinas measured at 24°C (2.79 ± 1.14) was significantly higher than that measured at 34°C (1.47 ± 0.69) ($p < 0.03$).

This is another test to further confirm that the measured temporal change of RNFL reflectance speckle was associated with axonal dynamic activity. In this test colchicine was used to depolymerize MTs. Figure 5.12A demonstrates a CC time course before colchicine treatment, and exponential fitting gave a time constant of 0.97 min. After 15 min of treatment the decrease of CC became

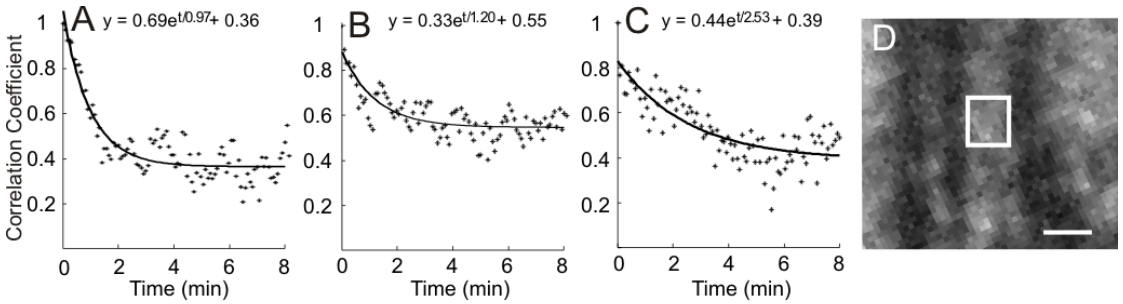

Figure 5.12. Effect of MT depolymerization on temporal change of RNFL reflectance speckle. (A) 20 min before colchicine treatment; (B, C) with colchicine treatment of 15 and 50 min, respectively. (D) Reflectance image of the time point in (C). White boxes: bundle area. Scale bar: 20 μm.

slower with τ = 1.20 min (Figure 5.12B); while with 50 min of treatment the decrease became much slower (τ = 2.53 min; Figure 5.12C). However, at this time point speckles were still apparent in the reflectance image (Figure 5.12D). Note that these time courses were from the same bundle area defined in Figure 5.12D. The CC time course of nearby gaps was similar over the entire treatment period. Twelve bundles in four treated retinas showed that τ increased from 1.16 ± 0.32 min at the baseline period to 1.97 ± 0.43 min after colchicine treatment of about 40 – 50 min ($p < 0.05$ for paired T-test for means).

In summary, we used fixed retina, retina perfused at lower temperatures and retina treated with colchicine to compare the measured CC time courses with that of normally prepared living retina. The three experiments well demonstrated that temporal change of RNFL reflectance speckle is associated with axonal dynamic activity.

5.5.5 RNFL Speckle among Bundles and along Bundles

As our study (Chapter III) shows that the contents of cytoskeletal components vary among axons, the dynamic activities may, therefore, vary among bundles. To study speckle dynamics across the retina, we measured reflectance speckle of different bundles and along the same bundles. Image series was taken with 660nm wavelength and 2 seconds exposure duration. Bundles with on-peak measurement were selected for study.

Figure 5.13 shows CC time courses of areas defined along the same bundle. The time courses appeared similar along bundle, the exponential function fitting gave τ for each area of 1.02 min and 1.32 min, respectively.

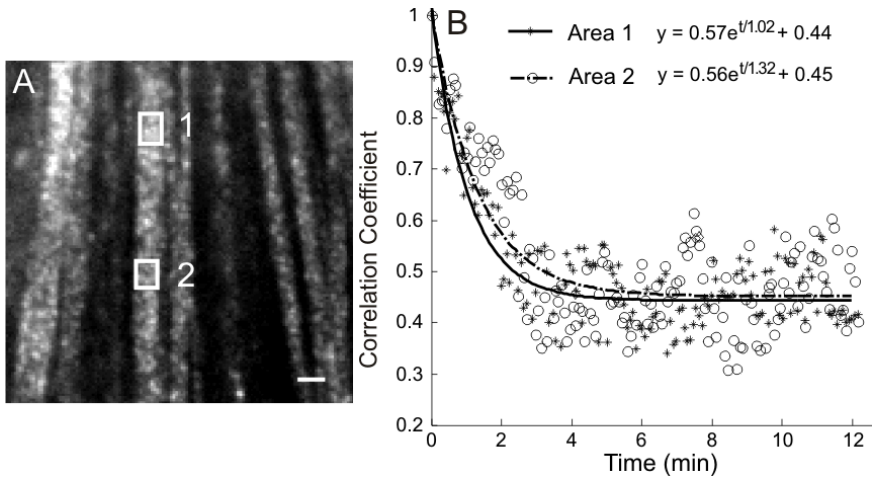

Figure 5.13. Correlation coefficient (CC) time courses of speckle along the same bundle with fitting. Scale bar: 20 μm.

This result indicates that axonal dynamic activities do not change along the bundle over a certain range, which agrees with the findings in Chapter III that the contents of cytoskeletal components don't change along the bundle at central retina area.

To compare temporal change of RNFL speckle at different bundles, three on-peak measured bundles which have similar incident and scattering angle,

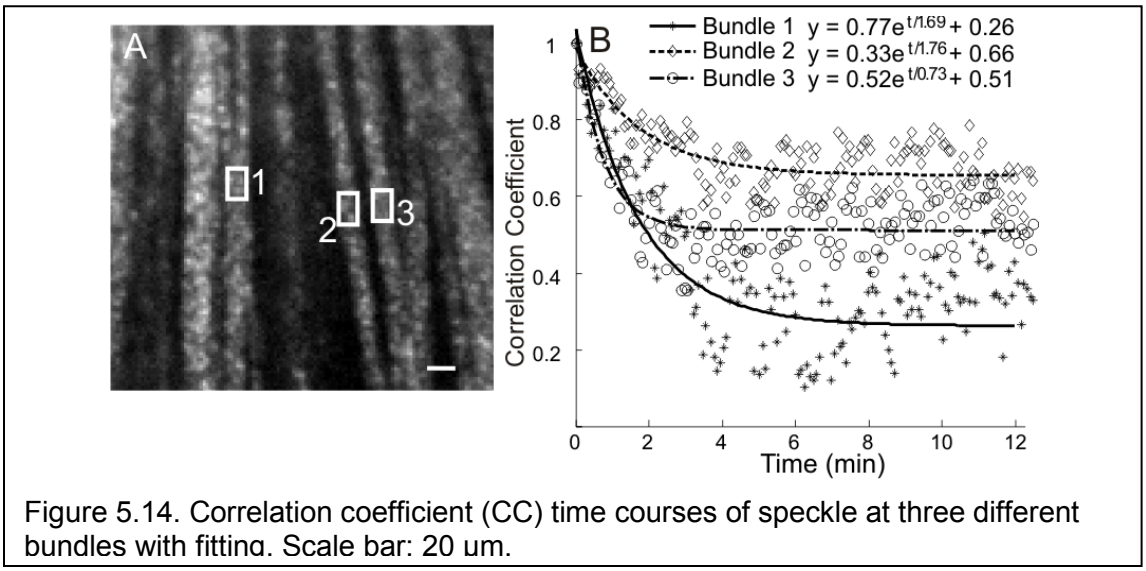

Figure 5.14. Correlation coefficient (CC) time courses of speckle at three different bundles with fitting. Scale bar: 20 um.

similar distances to the ONH, and similar bundle sizes were selected in the same retina as shown in Figure 5.14A. Figure 5.14B shows that the time courses differ from each other and exponential function fitting gave τ =1.69 min, 1.76 min, and 0.73 min, respectively (Figure 5.14B). The result shows that CC time courses are not the same among bundles even in the same retinas.

As discussed in Chapter III, the detailed contents of each axon are different and therefore, physiological functions are expected to vary among axons. The result that time course of RNFL reflectance speckle vary among bundles may indicates different axonal dynamic activities in different bundles.

5.5.6 A Preliminary Test: RNFL Speckle in Retinas with Glaucoma

Our experiments have demonstrated that temporal change of RNFL reflectance speckle is associated with axonal dynamic activity. This finding may provide a new means to detect axonal degeneration caused by neuropathic diseases, such as, glaucoma. As our studies described in Chapter II, glaucoma causes distortion of axonal cytoskeleton. Change of cytoskeleton should necessarily cause change of axonal activity, and hence, we expected that the CC time courses in glaucomatous retina should be different from the ones in normal retinas. To demonstrate temporal change of RNFL speckle in glaucomatous retina, reflectance image series were taken at 660nm with 2 seconds exposure every five seconds for about 15 minutes, as in normal retinas. Bundles with on-peak measurement were selected for analysis.

We took a preliminary test on retinas with mild glaucomatous damage. The bundles in glaucomatous retina (Figure 5.15B) appeared dimmer comparing to

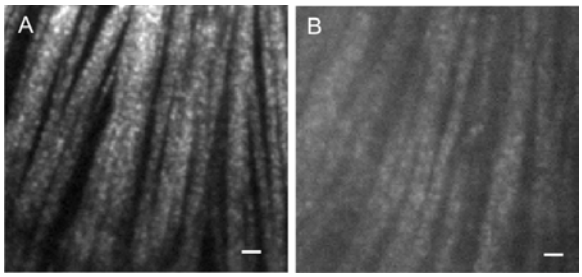

Figure 5.15. RNFL speckle appearance in normal (A) and glaucomatous (B) retinas. The bundles in (A) and (B) are the same distance from the ONH, and both images have the same contrast. (C) CC time course of speckle in different appearance bundle areas define in (B). Bundles in (B) appeared dimmer comparing to the ones in (A). The speckles in (B) were not as sharp as in (A). Scale bars: 20 μm.

normal bundles (Figure 5.15A). The speckles in glaucomatous retina were not as sharp as in normal retinas; yet thickness was similar to the normal tissue.

Figure 5.16 shows the CC time courses of two bundles in retinas with glaucoma. One was with fitted τ around 0.2 min (Figure 5.16A) which was

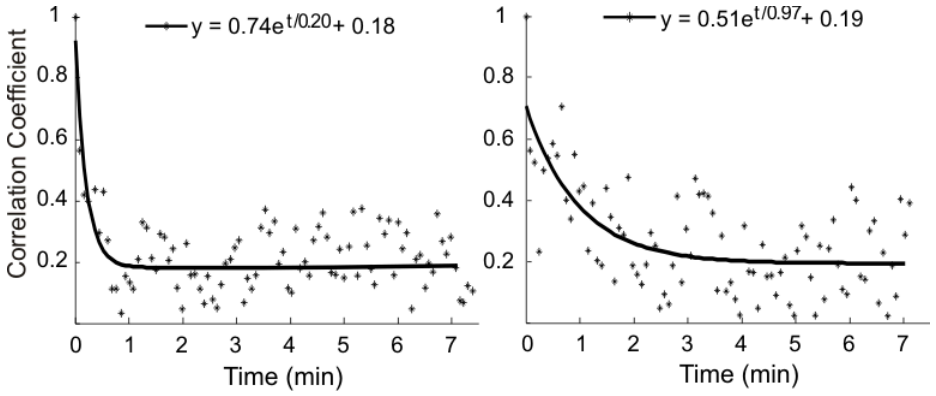

Figure 5.16. CC time courses of RNFL speckle in glaucomatous retinas.

significantly smaller than that of normal retinas, and the other one with τ around 1 min (Figure 5.16B), similar to the control. The time courses from six bundles on two retinas with glaucoma were analyzed. The average of fitted τ was 0.48 ± 0.32 min ranging from 0.14 to 0.97 min.

This preliminary experiment shows that the CC time course has been changed in glaucomatous retinas comparing to normal retinas. In the mildly damaged retinas, the time constant appeared less than that of normal. The result may suggest that hyperactive dynamic activities occur at early stage of glaucomatous damage. Further studies should provide a thorough investigation of temporal change of RNFL speckle at different degrees of glaucomatous damage.

5.6 Conclusion and Discussion

Measurements of optical properties in diagnostic methods such as SLP, OCT and cSLO have been implemented with static imaging of the RNFL. However, axons of RGCs are dynamic structures. The speckle pattern of RNFL

reflectance may change with the movement of scattering particles. Thus, measuring temporal change of RNFL speckle may provide information about the physiological activity of axons. In this study, we explored the concept of assessing axonal dynamic activity by measuring temporal change of the RNFL reflectance speckle, and investigated physical factors that may affect the measurement of RNFL reflectance speckle. The gained knowledge will help to develop a new method to detect physiological activity of axons.

We used monochromatic illumination and high resolution reflectance IMR to measure RNFL reflectance speckle in vitro prepared retinas. Monochromatic illumination provides prerequisite of speckle formation. In vitro preparation of retina eliminates the confounding effects of other ocular tissues on measurements.

i. The appearance of speckle is wavelength dependent.

We have observed that a speckled texture shown on RNFL reflectance images at different wavelengths. With decreasing of wavelength, the appearance of speckle becomes less apparent (Figure 5.4). This may be explained by the size of a coherence volume relative to the RNFL thickness. With quasi-monochromatic illumination, reflectance speckle arises mostly from temporal interference, i.e., interference between scattered components of a wave and the wave itself but delayed in depth. The cylindrical coherence volumes produced by the IMR could be calculated with Equations 5.1 and 5.2, as shown in Table 5.2, 5.3 and Figure 5.2. The coherence length increases with increasing of wavelength, resulting in that rays scattered from more bundle thickness contribute to the speckled texture. For example, the coherence length at 660 nm

is comparable to the thickness of a typical nerve fiber bundle (~15 lm), thus rays from the whole bundle thickness interfere with each other to contribute to the RNFL speckle. At 440 nm, however, the coherence length is only a fraction of the bundle thickness and the resulting speckles from different depths are superimposed on the average reflectance. Short wavelength speckles, therefore, have lower contrast, as seen in Figure 5.4C. This also confirms that RNFL reflectance speckle originated from its internal structure.

ii. The speckle pattern changes over time.

Image series at 660nm playing with time showed that the speckles appeared and faded but did not move along bundles for a few minutes. The speckle pattern change in a series of subimages was quantified with CCs between the reference and subsequent speckle patterns, which provided a measure of their similarity.

The CC was high at the beginning of an image series for normally prepared retinas, indicating high similarity between the speckle patterns. With the lapse of time, the CC decreased gradually until after a few minutes it varied around a plateau. The time constant (τ) of an exponential fit to the decrease was used to quantify how fast the change of CCs was.

Tissue fixed with paraformaldehyde was used to confirm speckle dynamics resulted from temporal change of reflecting structures. In fixed tissues, axonal activities were stopped, thus speckle pattern was supposed to not change with time. The results validated this hypothesis that there is no difference of the qualitative appearance of the RNFL speckle, but temporal change over time was eliminated.

The CC of gap areas decreased abruptly to a plateau. The average $\tau = 0.09$ minute was approximately the interval used for collecting an image series. This suggests that the reflectance of gap areas was not correlated between two consecutive images, and reflectance at each pixel changed randomly. The CC time courses of gaps were similar in normal and fixed retinas, suggesting that the random change of gap reflectance was due to the noise of the optical measurements.

iii. The measurement of RNFL speckle is sensitive to physical factors.

Physical factors effecting measurement of reflectance of speckle were investigated. The dependence of CC time course of measured RNFL speckle on imaging system geometric settings requires that the speckle phenomenon should always be quantified with on-peak measurement.

We have discussed above that at longer wavelengths (such as 660nm and 830nm), speckles result from the whole bundle thickness whereas at shorter wavelengths , speckles from a portion of bundles. The temporal change of scattering particles depends axonal functions, the independence of time course of RNFL speckle on wavelength may be explained as that measured speckle change reflects averaged axonal dynamic activity within the RNFL.

The time constant from exponential function fitting of the CC time course depends on the exposure duration. This indicates that temporal change measured with different exposure duration reflects different axonal activities.

iv. Temporal change of RNFL reflectance speckle is associated with axonal dynamic activity

To test the hypothesis that temporal change of RNFL reflectance speckle is associated with axonal dynamic activity, three experiments were performed to interfere this activity. The first experiment was tissue fixation. As mentioned above, the scattering structures were expected to remain stationary. The results showed that the speckled texture of the RNFL in fixed retina did not show apparent change with the lapse of time, time course of CCs also showed that the speckle pattern highly correlated over time (Figure 5.5C). The second experiment used normally prepared retinas perfused with a physiologic solution at a lower temperature. Because low temperature slows axonal transport [127] and other physiological processes, the slower decay of the CC measured at 24°C (Figure 5.5) demonstrates a link between change of speckle and axonal dynamic activity. The third experiment attempted to relate temporal change of RNFL speckle to axonal transport by depolymerizing MTs with colchicine. MT depolymerization was expected to disrupt axonal transport [130]. The CC time courses (Figure 5.6) obtained with different durations of MT depolymerization confirmed this expectation; the decay of CC became slower with the colchicine treatment and the time constant increased with the duration of treatment.

v. Significance of Measuring Temporal Change of RNFL Speckle and Future Study

A preliminary test of RNFL speckle in retinas with glaucoma has shown that the temporal change of RNFL speckle in glaucomatous retina is different from that of normal retinas. The limited data gave smaller fitted time constants. This may seem conflict with the concept that glaucoma damages axons which may

result in slower axonal transport, but there is one possibility that we have measured at a damage period during which the initial neuroprotection mechanism is to increase dynamic activity. Future study should study temporal changes on retinas with different degree of glaucoma.

This study demonstrates that measurement of RNFL reflectance can provides functional information of the RNFL. It may provide a new means to detect axonal dynamic activities. For example, monitoring patients with temporal change of RNFL speckle maybe a method to trace possible glaucomatous damage over the years.

Recently reported RNFL images obtained with adaptive optics scanning laser ophthalmoscopy (AOSLO) reveal a similar speckled texture of RNFL reflectance in human eyes (Scoles DH, et al. IOVS 2012;53:ARVO E-Abstract 6954)[131]. If it can be demonstrated that the apparent AOSLO speckle also arises from interference, it may be possible to adapt AOSLO technology for non-invasive assessment of axonal dynamic activity in clinical practice.

5.7 Summary

With monochromatic illumination and high resolution imaging, RNFL reflectance demonstrates speckle phenomena. Textured speckles of nerve fiber bundles change with time. We hypothesized that the temporal variation of RNFL speckle was associated with axonal dynamic activity.

In this study, we have investigated physical factors that affect the measurements of RNFL speckles. We have developed a method, CC time course, to quantify temporal change of RNFL speckle. With experimental

interference of axonal dynamic activity, we have demonstrated that the temporal change of RNFL speckle was associated with axonal dynamic activity.

This study provides a new concept of non-invasive detection of physiological activity of axons, which may precede loss of axonal structure in glaucoma.

In this study, Ye Spector contributed to experimental design of Goal 1 and also did animal experiments, collecting data and data analysis.

Chapter 6. Significance and Future Work

6.1 Significance

Glaucoma is the second leading cause of blindness in the world [132]. Statistics gathered by WHO in 2002 reported that about 37 million people worldwide were blind, and glaucoma impacts one in 200 people aged 50 and younger, and one in 10 over the age of eighty [133]. The progressive glaucomatous damage is irreversible, and the resultant vision loss is irredeemable. Thus, early diagnosis of glaucoma is very important for early intervention and preventing further deterioration.

Glaucomatous damage to the RNFL usually precedes detectable visual field loss; clinical assessment of the RNFL is valuable in diagnosis of glaucoma and other neuropathic diseases. Various quantitative methods, such as OCT and cSLO, have been developed to measure the RNFL thickness by exanimate the reflectance of RNFL. However, knowledge about the changes of RNFL reflectance and its underlying ultrastructure under the development of glaucoma is limited.

This dissertation presents the work we have done to improve the understanding of the relationship between change of RNFL reflectance and glaucomatous damage. We have found that the decrease of RNFL reflectance in glaucomatous retina occurred first at short wavelength and the change of RNFL reflectance spectra happened early in bundles near the ONH. Moreover, the decrease of RNFL reflectance occurred prior to RNFL thinning and apparent cytoskeletal change. These findings have significant impact on improvement of

early and sensitive detection of glaucomatous damage in clinical practice. To provide sensitive detection of early glaucomatous damage our findings give the following suggestions: 1) measuring RNFL reflectance, instead of thickness, 2) using short wavelength for reflectance measurement, and 3) detecting glaucomatous damage near the ONH.

This dissertation also explored a new idea that measurement of RNFL reflectance speckle may provide assessment of axonal function. Currently, measurement of RNFL reflectance is limited to assess RNFL structure. Our experiments have demonstrated that temporal change of RNFL speckle associates with axonal dynamic activities. The results suggest that RNFL reflectance measured with monochromatic illumination and high resolution imaging gives both structural and functional assessment of RNFL bundles.

RNFL reflectance arises from light scattering by axonal ultrastructures. Change of RNFL reflectance should directly reflect underlying structure change. To study the relationship between RNFL optical properties and axonal ultrastructures, this dissertation also investigated cytoskeletal damages in retinas with different degree of glaucoma. We have related change of RNFL reflectance to the degrees of cytoskeletal damage. Hence, measurement of RNFL reflectance can provide non-invasive assessment of ultrastructure or tissue diagnosis.

Classification of RGCs helps understanding damage mechanisms of RGCs in the context of ocular neuropathic diseases. In this dissertation, we have developed a new method to classify RGCs based on the content of each

cytoskeletal component in axons. We have found axonal subtypes that contain different proportions of cytoskeletal components. This classification method provides enhanced understanding of selective damage mechanisms in glaucoma and other ocular neuropathic diseases.

6.2 Future Work

Our studies have demonstrated that F-actin is the most sensitive cytoskeleton to respond to glaucomatous insult. However, the role of F-actin in the optical properties of the RNFL is unknown. Future study may be focused on determining the contribution of F-actin to RNFL optical properties. Gained knowledge may help to develop new optical methods for sensitive assessment of RNFL change in glaucomatous retinas.

Currently optical methods for RNFL assessment use near-infrared wavelengths. Our studies show that RNFL reflectance measured at short wavelength is more sensitive to detect early glaucomatous damage. Recently developed dual-wavelength OCT also demonstrates the feasibility to measure RNFL reflectance at 415 nm and 808nm in rat retinas. Optical techniques with multiple wavelengths are preferred to be developed for early detection of glaucomatous damage.

Our experiments have proved that temporal change of RNFL speckle is associated with axonal dynamic activity. Measuring temporal change of RNFL speckle provides function information of axons. Our preliminary study has shown that the temporal change of RNFL speckle in retinas with glaucoma is different from that of normal retinas. Future study should focus on a complete

investigation of RNFL speckle temporal change in glaucomatous retinas and understand its underlying mechanisms. This may have profound impact on the diagnosis of glaucoma because many studies have showed that physiological function change proceeds axonal structural change in glaucomatous retinas [29-32].

Appendix. Calibration of the IMR System

i. Coordinate system in the IMR system

Before calibration, we defined the coordinate system in IMR system (Figure A1). The origin of the coordinate system was defined on the sample surface where the optical axes of the camera and light source coincide. The camera's

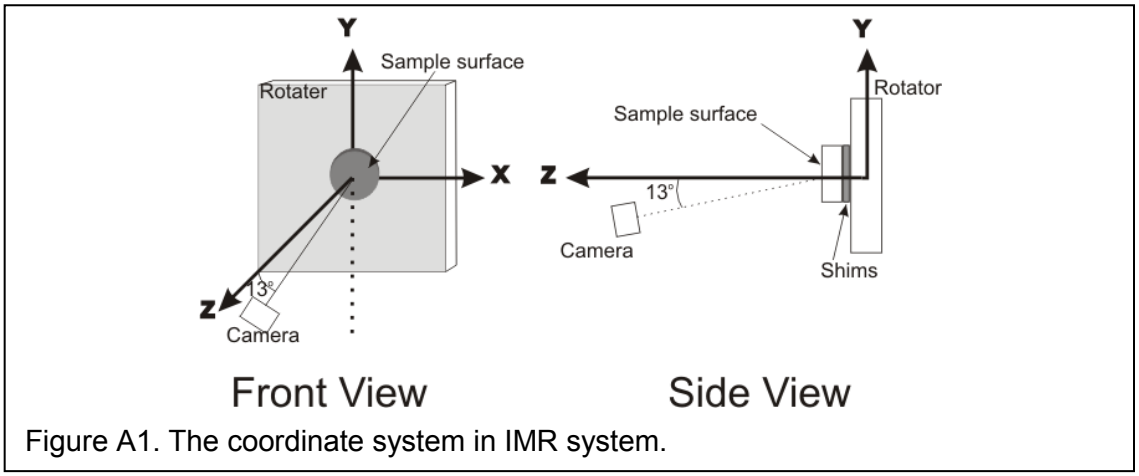

Figure A1. The coordinate system in IMR system.

azimuth rotation axis was defined as Y axis, the rotator's rotation axis was long the Z axis, and X axis was defined perpendicular to the defined YZ plane and forming XYZ coordinate system with defined Y and Z axes. The sample surface was located in XY plane. The camera could be moved along a circle with fixed elevation of -13° (to XZ plane) around the Y axis, and the light source could be adjusted both around Y axis (azimuth) and around X axis (elevation). We defined camera azimuth as 0° when it's located in YZ plane, -90° when it's located in left side and 90° when it's located in right side of the XY plane viewing from front. The azimuth of light source was defined similarly. The elevation of light source was defined as 0° when it's located in XZ plane, -90° when it's located in bottom and 90° when it's located in upper side of the XYZ coordinate system viewing from front.

ii. Camera setting calibration

To get the magnification in X,Y direction: Rx and Ry (μm/pixel), azimuth of camera (AZcam) was set to 0°. The sample was moved μm and μm along the X and Y axes and images were taken before and after the move (Figure A2).

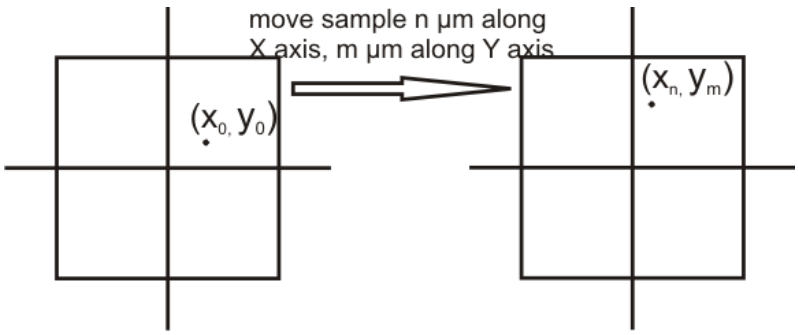

Figure A2. Schematic drawing of magnification calculation.

The (x, y) coordinates of a selected feature in the images were measured. Thus Rx and Ry could be calculated as: $Rx = \frac{n}{x_n - x_0}, \quad Ry = \frac{m}{y_m - y_0}$ (μm/pixel). Note that magnification varies with wavelength and magnifications at different wavelength were measured.

To make sure the camera azimuth measurement was true to the ideal system, i.e. AZcam = 0° is located in YZ plane, image was taken when the sample was rotated very fast. The image was again taken when rotated very fast after adding shims with thickness and changing focus accordingly. The (x, y) coordinates of the rotation center in images were recorded. The camera inclination were calculated as: dAZ = arctan(dx *Rx/df); dEL = arctan(dy * Ry/df) (Figure A3). Ideally, dAZ should be 0°, and dEL should be -13°. If not, set AZcam = 0° to dAZ, and adjust camera mount bar until measured dEL be -13°.

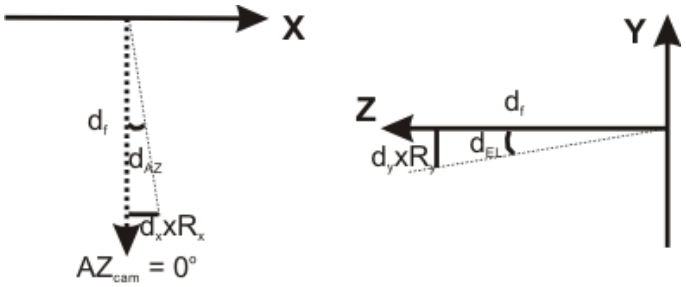

Figure A3. Schematic drawing of camera inclination calculation.

To make sure the camera pivot axis in the XY plane, or make sure sample surface located in the XY plane, so that there is no change in the imaged area of the sample when camera is changed in azimuth, images were taken when

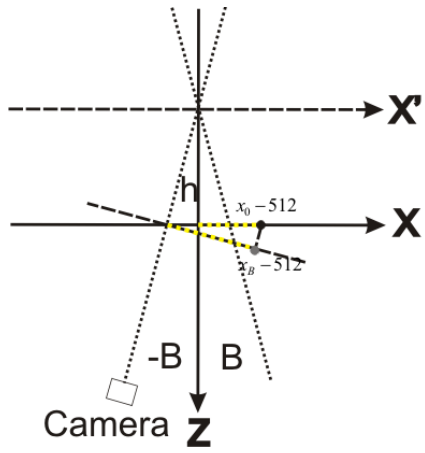

Figure A4. Schematic drawing of shims thickness needed to add to or remove from the rotator.

AZcam = 0°, and AZcam = 0° ± B, without change of focus. The thickness of shims needed could be calculated as _____ (Figure A4). Note that shims were added if h is positive and removed if h is negative.

iii. Light source (LS) calibration

We used the camera setting as system's reference to calibrate light source (LS), i.e. we assumed that the camera setting in the system was ideal.

To set LS axis pararall to camera axis, or set the LS rotation center at the spherical system center, AZcam was set to -90°, AZls was set to 90° and ELls was set to 13° to make LS approximately parallel to camera probe. Images were taken at two different focus value f1 and f2 (around the focus where optical fiber (OF) was well focused). After getting the OF centers in the images, the inclination of LS could be calculated as ————, ————. The azimuth and elevation of LS should be changed by and to make . Then the AZLS dials was set as 90° and ELLS was set as -ELcam.

List of Publications

Journal:

Ye Z. Spector, Qi Zhao, Xiaopeng Zhao, William J. Feuer,Portia Lynn Maravich, Xiang-Run Huang. Classification of Axonal Subtypes Based on Cytoskeletal Components. Cell Health and Cytoskeleton. Accepted.

Xiang-Run Huang, Robert W. Knighton, Ye Zhou and Xiao-Peng Zhao. Reflectance Speckle of Retinal Nerve Fiber Layer Reveals Axonal Activity. Invest. Ophthalmol. Vis. Sci.April, 2013 vol. 54 no. 4 2616-2623.

Xiang-Run Huang, Ye Zhou, Robert W. Knighton, Wei Kong and William J. Feuer. Wavelength-Dependent Change of Retinal Nerve Fiber Layer Reflectance in Glaucomatous Retinas. Invest. Ophthalmol. Vis. Sci.August, 2012 vol. 53 no. 9 5869-5876.

Xiangrun Huang, Wei Kong, Ye Zhou and Giovanni Gregori. Distortion of Axonal Cytoskeleton: An Early Sign of Glaucomatous Damage. Invest. Ophthalmol. Vis. Sci.May, 2011 vol. 52 no. 62879-2888.

Xiang-Run Huang, Ye Zhou, Wei Kong and Robert W. Knighton. Reflectance Decreases before Thickness Changes in the Retinal Nerve Fiber Layer in Glaucomatous Retinas. Invest. Ophthalmol. Vis. Sci.August, 2011 vol. 52no. 9 6737-6742.

Abstract:

Ye Zhou, Xiaopeng Zhao, Xiang-Run Huang. Relationship between Axonal Subtypes and Size of Retinal Nerve Fiber Bundles. Invest. Ophthalmol. Vis. Sci.2013; 43: ARVO E-abstract 2289.

Xiang-Run Huang, Ye Zhou, Siobhan Williams, XiaoPeng Zhao, Robert W. Knighton. Does Reflectance Speckle of Retinal Nerve Fiber Layer Relate to Axonal Activity? Invest. Ophthalmol. Vis. Sci.2012; 43: ARVO E-abstract 1746.

Ye Zhou, Xiaopeng Zhao, Siobhan Williams, Wei Kong, Xiangrun Huang. Axonal Subtypes in Normal and Glaucomatous Retinas. Invest. Ophthalmol. Vis. Sci.2012; 43: ARVO E-abstract 6608.

Xiang-Run Huang, Ye Zhou, Wei Kong, Robert W. Knighton. Change of Retinal Nerve Fiber Layer Reflectance Correlated with Cytostructural Change in Glaucoma. Invest. Ophthalmol. Vis. Sci.2011; 43: ARVO E-abstract 2442.

Ye Zhou, Xiangrun Huang, Wei Kong, Robert W. Knighton. Reflectance Decrease Prior to Thinning of Retinal Nerve Fiber Layer in Glaucomatous Retinas. Invest. Ophthalmol. Vis. Sci.2011; 43: ARVO E-abstract 2443.

Xiang-Run Huang, Wei Kong, Ye Zhou, Robert W. Knighton. Decrease of Retinal Nerve Fiber Layer Reflectance: Early Sign of Glaucomatous Damage? Invest. Ophthalmol. Vis. Sci.2010; 43: ARVO E-abstract 4808.

Wei Kong, Xiang-Run Huang, Ye Zhou. Distortion of Axonal Cytoskeleton in Glaucomatous Retina. Invest. Ophthalmol. Vis. Sci.2010; 43: ARVO E-abstract 2119.

References

1. Knighton RW, Huang X-R (1999) Directional and spectral reflectance of the rat retinal nerve fiber layer. Invest Ophthalmol Vis Sci 40: 639-647.

2. Huang X-R, Knighton RW, Cavuoto LN (2006) Microtubule contribution to the reflectance of the retinal nerve fiber layer. Invest Ophthalmol Vis Sci 47: 5363-5367.

3. Knighton R, Zhou Q (1995) The relation between reflectance and thickness of the retinal nerve fiber layer. J Glaucoma 4: 117-123.

4. Dowling JE (1987) Retinal cells and information processing. The Retina: An Approachable Part of the Brain 1st ed: Belknap Press of Harvard University Press.

5. Purves D, Augustine GJ, Fitzpatrick D, Hall WC, LaMantia A-S, et al. (2001) The retina. Neuroscience. 5th ed. Sunderland, MA: Sinauer Associates.

6. Knighton RW, Jacobson SG, Kemp CM (1989) Spectral reflectance of the retinal nerve fiber layer in macaques. Invest Ophthalmol Vis Sci 30: 2392-2402.

7. RW RWK, Baverez C, Bhattacharya A (1992) The directional reflectance of the retinal nerve fiber layer of the toad. Invest Ophthalmol Vis Sci 33: 2603-2611.

8. Zhou Q, Knighton RW (1997) Light scattering and form birefringence of parallel cylindrical arrays that represent cellular organelles of the retinal nerve fiber layer. Appl Opt 36: 2273-2285.

9. Knighton RW, Huang X-R (1999) Visible and near-infrared imaging of the nerve fiber layer of the isolated rat retina. J Glaucoma 8: 31-37.

10. Knighton RW, Huang X-R, Zhou Q (1998) Microtubule contribution to the reflectance of the retinal nerve fiber layer. Invest Ophthalmol Vis Sci 39: 189-193.

11. Huang X-R, Knighton RW, Shestopalov V (2006) Quantifying retinal nerve fiber layer thickness in whole-mounted retina. Exp Eye Res 83: 1096-1101.

12. McKerracher L, Essagian C, Aguayo AJ (1993) Temporal changes in betatubulin and neurofilament mRNA levels after transection of adult rat retinal ganglion cell axons in the optic nerve. J Neurosci 13: 2617-2626.

13. Villegas-Perez MP, Vidal-Sam M, Bray GM, Aguayo AJ (1988) Influences of peripheral nerve grafts on the survival and regrowth of axotomized retinal ganglion cells in adult rats. J Neurosci 8: 265-280.

14. Balaratnasingam C, Morgan WH, Bass L, Cringle SJ, Yu D-Y (2008) Time-dependent effects of elevated intraocular pressure on optic nerve head axonal transport and cytoskeleton proteins. Invest Ophthalmol Vis Sci 49: 986-999.

15. Schuman JS, Hee MR, Arya AV, al e (1995) Optical coherence tomography: a new tool for glaucoma diagnosis. Curr Opin Ophthalmol 6: 89-95.

16. Medeiros FA, Bowd C, Zangwill LM, Patel C, Weinreb RN (2007) Detection of glaucoma using scanning laser polarimetry with enhanced corneal compensation. Invest Ophthalmol Vis Sci 48: 3146-3153.

17. Alexandrescu C, Dascalu A, Panca A, al e (2010) Confocal scanning laser ophthalmoscopy in glaucoma diagnosis and management. J Med Life 3: 229-234.

18. Casson RJ, Chidlow G, Wood JP, Crowston JG, Goldberg I (2012) Definition of glaucoma: clinical and experimental concepts. Clin Exp Ophthalmol 40: 341-349.

19. Goel M, Picciani RG, Lee RK, Bhattacharya SK (2010) Aqueous humor dynamics: a review. Open Ophthalmol J 4: 52-59.

20. Ahn JK, Kang JH, Park KH (2004) Correlation between a disc hemorrhage and peripapillary atrophy in glaucoma patients with a unilateral disc hemorrhage. J Glaucoma 13: 9-14.

21. Armaly M (1967) Genetic determination of cup/disc ratio of the optic nerve. Arch Ophthalmol 78: 35-43.

22. Marjanovic I (2011) The Optic Nerve in Glaucoma. In: Kubena T, editor. The mystery of glaucoma: InTech.

23. Hoffman PN, Cleveland DW, Griffin JW, Landes PW, Cowan NJ, et al. (1987) Neurofilament gene expression: a major determinant of axonal caliber. Proc Natl Acad Sci U S A 84: 3472-3476.

24. Vickersa JC, Schumer RA, Podos SM, Wang RF, Riederer BM, et al. (1995) Differential vulnerability of neurochemically identified subpopulations of retinal neurons in a monkey model of glaucoma. Brain Res 680: 23-35.

25. Jakobs TC, Libby RT, Ben Y, John SW, Masland RH (2005) Retinal ganglion cell degeneration is topological but not cell type specific in DBA/2J mice. J Cell Biol 171: 313-325.

26. Fu CT, Sretavan D (2010) Laser-induced ocular hypertension in albino CD-1 mice. Invest Ophthalmol Vis Sci 51: 980-990.

27. Ou B, Ohno S, Tsukahara S (1998) Ultrastructural changes and immunocytochemical localization of microtubule-associated protein 1 in guinea pig optic nerves after acute increase in intraocular pressure. Invest Ophthalmol Vis Sci 39: 963-971.

28. Huang X-R, Knighton RW (2009) Altered F-actin distribution in retinal nerve fiber layer of a rat model of glaucoma. Exp Eye Res 88: 1107-1114.

29. Bull ND, Guidi A, Goedert M, mail KRM, Spillantini MG (2012) Reduced Axonal Transport and Increased Excitotoxic Retinal Ganglion Cell Degeneration in Mice Transgenic for Human Mutant P301S Tau. PLoS ONE 7: e34724.

30. Pease ME, McKinnon SJ, Quigley HA, Kerrigan–Baumrind LA, Zack DJ (2000) Obstructed axonal transport of BDNF and its receptor TrkB in experimental glaucoma. Invest Ophthalmol Vis Sci 41: 764-774.

31. Bourges-Abella N, Raymond-Letron I, Diquelou A, Guillot E, Regnier A, et al. (2007) Retrograde axonal transport obstruction of brain-derived neurotrophic factor (BDNF) and its TrkB receptor in the retina and optic nerve of American Cocker Spaniel dogs with spontaneous glaucoma. Vet Ophthalmol 10: 12-18.

32. Chidlow G, Wood JPM, Ebneter A, Casson RJ (2012) Interleukin-6 is an efficacious marker of axonal transport disruption during experimental glaucoma and stimulates neuritogenesis in cultured retinal ganglion cells. Neurobiol Dis 48: 568-581.

33. Chidlow G, Ebneter A, Wood JPM, Casson RJ (2011) The optic nerve head is the site of axonal transport disruption, axonal cytoskeleton damage and putative axonal regeneration failure in a rat model of glaucoma. Acta Neuropathol 121: 737-751.

34. Van Der Zypen E (1977) Experimental morphological study on structure and function of the filtration angle of the rat eye. Ophthalmologica 174: 285-298.

35. Daimon T, Kazama M, Miyajima Y, Nakano M (1997) Immunocytochemical localization of thrombomodulin in the aqueous humor passage of the rat eye. Histochem Cell Biol 108: 121-131.

36. Reme Ch, Aeberhard B, Urner U (1983) The development of the chamber angle in the rat eye. Morphological characteristics of developmental stages. Graefe's Archive for Clinical and Experimental Ophthalmology 220: 139-153.

37. Nucci P, Tredici G, Manitto MP, Pizzini G, Brancato R (1992) Neuron-specific enolase and embryology of the trabecular meshwork of the rat eye: an immunohistochemical study. International Journal of Biological Markers 7: 253-255.

38. Bouhenni RA, Dunmire J, Sewell A, Edward DP (2012) Animal models of glaucoma. J Biomed Biotechnol 2012.

39. Rudzinski M, Saragovi HU (2005) Glaucoma: validated and facile in vivo experimental models of a chronic neurodegenerative disease for drug development. Curr Med Chem 5: 43-49.

40. March WF, Gherezghiher T, Koss M, Nordquist R (1984) Ultrastructural and pharmacologic studies on laser-induced glaucoma in primates and rabbits. Lasers Surg Med 4: 329-335.

41. Radius RL, Pederson JE (1984) Laser-induced primate glaucoma. II. Histopathology. Arch Ophthalmol 102: 1693-1698.

42. Hwang J-M, Kim T-W, Park KH, Kim DM, Kim H (2006) Correlation between topographic profiles of localized retinal nerve fiber layer defects as determined by optical coherence tomography and red-free fundus photography. J Glaucoma 15: 223-228.

43. Teesalu P, A AT, Airaksinen PJ (2000) Optical coherence tomography and localized defects of the retinal nerve fiber layer. Acta Ophthalmol Scand 78: 49-52.

44. Kim T-W, Park U-C, Park KH, Kim DM (2007) Ability of Stratus OCT to identify localized retinal nerve fiber layer defects in patients with normal standard automated perimetry results. Invest Ophthalmol Vis Sci 48: 1635-1641.

45. Soliman MAE, Berg TJTPvd, Ismaeil A-AA, Jong LAMSd, Smet MDd (2002) Retinal nerve fiber layer analysis: relationship between optical coherence tomography and red-free photography. Am J Ophthalmol 133: 187-195.

46. Greaney MJ, Hoffman DC, Garway-Heath DF, Nakla M, Coleman AL, et al. (2002) Comparison of optic nerve imaging methods to distinguish normal eyes from those with glaucoma. Invest Ophthalmol Vis Sci 43: 140-145.

47. Nukada M, Hangai M, Mori S, al e (2011) Detection of localized retinal nerve fiber layer defects in glaucoma using enhanced spectral-domain optical coherence tomography. Ophthalmol 118: 1038-1048.

48. Aizu Y, Asakura T (1991) Bio-speckle phenomena and their application to the evaluation of blood flow. Optics and Laser Technology 23: 205-219.

49. Boas DA, Dunn AK (2010) Laser speckle contrast imaging in biomedical optics. J Biomed Opt 15: 1-12.

50. Lodish H, Berk A, Zipursky SL, Matsudaira P, Baltimore D, et al. (2000) Overview of neuron structure and function. Molecular Cell Biology. 4th ed. New York: W. H. Freeman.

51. Hildebrand C, Waxman SG (1983) Regional node-like membrane specializations in non-myelinated axons of rat retinal nerve fiber layer. Brain Res 258: 23-32.

52. Cooper GM (2000) Structure and organization of actin filaments. The Cell: A Molecular Approach. 2nd ed. Sunderland (MA): Sinauer Associates.

53. Darnell J, Lodish H, Baltimore D (1990) Molecular Cell Biology. New York: Scientific American Books.

54. Sato M, Leimbach G, Schwarz WH, Pollard TD (1985) Mechanical properties of actin. J Biol Chem 260: 8585-8592.

55. Fath KR, Lasek RJ (1988) Two classes of actin microfilaments are associated with the inner cytoskeleton of axons. J Cell Biol 107: 613-621.

56. Goode BL, Drubin DG, Barnes G (2000) Functional cooperation between the microtubule and actin cytoskeletons. Curr Opin Cell Biol 12: 63-71.

57. Zhou F-Q, Waterman-Storer CM, Cohan CS (2002) Focal loss of actin bundles causes microtubule redistribution and growth cone turning. J Cell Biol 157: 839-849.

58. Hasaka TP, Myers KA, Baas PW (2004) Role of actin filaments in the axonal transport of microtubules. J Neurosci 24: 11291-11301.

59. Hoffman PN (1995) Review: the synthesis, axonal transport, and phosphorylation of neurofilaments determine axonal caliber in myelinated nerve fibers. The Neuroscientist 1: 76-83.

60. Levkovitch-Verbin H, Quigley HA, Martin KRG, Valenta D, Baumrind LA, et al. (2002) Translimbal laser photocoagulation to the trabecular meshwork as a model of glaucoma in rats. Invest Ophthalmol Vis Sci 43: 402-410.

61. Cole RW, Jinadasa T, Brown CM (2011) Measuring and interpreting point spread functions to determine confocal microscope resolution and ensure quality control. Nat Protoc 6: 1929-1941.

62. Gonzalez RC, Woods RE, Eddins SL (2009) Digital image processing using MATLAB. Knoxville, TN: Gatesmark Publishing.

63. Materka A, Strzelecki M (1998) Texture analysis methods – a review. Technical University of Lodz, Institute of Electronics, COST B11 report.

64. Balaratnasingam C, Morgan WH, Johnstone V, Cringle SJ, Yu DY (2009) Heterogeneous distribution of axonal cytoskeleton proteins in the human optic nerve. Invest Ophthalmol Vis Sci 50: 2824-2838.

65. Lodish H, Berk A, Zipursky SL, Matsudaira P, Baltimore D, et al. (2000) The actin cytoskeleton. Molecular Cell Biology. 4th ed. New York: W. H. Freeman.

66. Price RL, Lasek RJ, Katz MJ. Neurofilaments pack differently in different parts of the same axon. In: Bailey GW, editor; 1988; San Francisco. pp. 270-271.

67. Price RL, Lasek RJ, Katz MJ (1990) Internal axonal cytoarchitecture is shaped locally by external compressive forces. Brain Res 530: 205-214.

68. Naskar R, Wissing M, Thanos S (2002) Detection of early neuron degeneration and accompanying microglial responses in the retina of a rat model of glaucoma. Invest Ophthalmol Vis Sci 43: 2962-2968.

69. Water BVd, Kruidering M, Nagelkerke JF (1996) F-actin disorganization in apoptotic cell death of cultured rat renal proximal tubular cells. Am J Physiol 270: F593-603.

70. Okada T, Otani H, Wu Y, Kyoi S, Enoki C, et al. (2005) Role of F-actin organization in p38 MAP kinase-mediated apoptosis and necrosis in neonatal rat cardiomyocytes subjected to simulated ischemia and reoxygenation. Am J Physiol Heart Circ Physiol 289: H2310-2318.

71. Schliwa M (1986) The cytoskeleton. Vienna: Springer-Verlag.

72. Danias J, Shen F, Kavalarakis M, Chen B, Goldblum D, et al. (2006) Characterization of retinal damage in the episcleral vein cauterization rat glaucoma model. Exp Eye Res 82: 219-228.

73. Soto I, Pease ME, Son JL, Shi X, Quigley HA, et al. (2011) Retinal ganglion cell loss in a rat ocular hypertension model is sectorial and involves early optic nerve axon loss. Invest Ophthalmol Vis Sci 52: 434-441.

74. Danias J, Shen F, Goldblum D, Chen B, Ramos-Esteban J, et al. (2002) Cytoarchitecture of the retinal ganglion cells in the rat. Invest Ophthalmol Vis Sci 43: 587-594.

75. Nadal-Nicolás FM, Jiménez-López M, Sobrado-Calvo P, Nieto-López L, Cánovas-Martínez I, et al. (2009) Brn3a as a marker of retinal ganglion cells: qualitative and quantitative time course studies in naive and optic nerve-injured retinas. Invest Ophthalmol Vis Sci 50: 3860-3868.

76. Schlamp CL, Li Y, Dietz JA, Janssen KT, Nickells RW (2006) Progressive ganglion cell loss and optic nerve degeneration in DBA/2J mice is variable and asymmetric. BMC Neurosci 7: 66.

77. Filippopoulos T, Danias J, Chen B, Podos SM, Mittag TW (2006) Topographic and morphologic analyses of retinal ganglion cell loss in old DBA/2NNia mice. Invest Ophthalmol Vis Sci 47: 1968-1974.

78. Reichsteina D, Rena L, Filippopoulos T, Mittag T, Danias J (2007) Apoptotic retinal ganglion cell death in the DBA/2 mouse model of glaucoma. Exp Eye Res 84: 13-21.

79. Gunn DJ, Gole GA, Barnett NL (2011) Specific amacrine cell changes in an induced mouse model of glaucoma. Clin Exp Ophthalmol 39: 555-563.

80. Tezel G, Group tFAPORICW (2009) The role of glia, mitochondria, and the immune system in glaucoma. Invest Ophthalmol Vis Sci 50: 1001-1012.

81. Sernagor E, Eglen SJ, Wong ROL (2001) Development of retinal ganglion cell structure and function. Prog Retin Eye Res 20: 139-174.

82. Wassle H, Boycott BB (1991) Functional architecture of the mammalian retina. Physiol Rev 71: 447-480.

83. Rodieck RW (1998) The first steps in seeing. Sunderland, MA: Sinauer Associates.

84. Friedlander MJ, Tootle JS (1990) Postnatal anatomical and physiological development of the visual system. Development of sensory systems in mammals. New York: Wiley, Inc.

85. Garraghty PE, Sur M (1998) Competitive interactions influencing the development of retinal axonal arbors in cat lateral geniculate nucleus. Physiol Rev 73: 529-545.

86. Yamagata M, Sanes JR (1995) Lamina-specific cues guide outgrowth and arborization of retinal axons in the optic tectum. Development 121: 189-200.

87. Boycott BB, Dowling JE, Kolb H (1969) Organization of the primate retina: light microscopy. Philosophical Transactions: Biological Sciences. London: Royal Society. pp. 109-184.

88. Cajal Ry (1892) la retine des vertebres. La cellule 9: 119-257.

89. Polyak SL (1941) The retina. Chicago: University of Chicago Press.

90. Polyak SL (1957) The vertebrate visual system. Chicago: University of Chicago Press.

91. Dacey DM (1999) Primate retina: cell types, circuits and color opponency. Prog Retin Eye Res 18: 737-763.

92. Cook JE (1998) Getting to grips with neuronal diversity. In: Chalupa LM, Finlay BL, editors. Development and Organization of the Retina. New York: Springer US. pp. 91-120.

93. Friede RL, Samorajski T (1970) Axon caliber related to neurofilaments and microtubules in sciatic nerve fibers of rats and mice. Anat Rec 167: 379-388.

94. Peters A, Vaughn JE (1967) microtubules and filaments in the axons and astrocytes of early postnatal rat optic nerves. J Cell Biol 32: 113-119.

95. Dent EW, Kalil K (2001) Axon branching requires interactions between dynamic microtubules and actin filaments. J Neurosci 21: 9757-9769.

96. Etienne-Manneville S (2013) Microtubules in cell migration. Annu Rev Cell Dev Biol: In press.

97. Wehrle-Haller B, Imhof BA (2003) Actin, microtubules and focal adhesion dynamics during cell migration. Int J Biochem Cell Biol 35: 39-50.

98. Fukuda Y, Watanabe M, Wakakuwa K, Sawai H, Morigiwa K (1988) Intraretinal axons of ganglion cells in the Japanese monkey (Macaca fuscata): conduction velocity and diameter distribution. Neurosci Res 6: 53-71.

99. Sugimoto T, Fukuda Y, Wakakuwa K (1984) Quantitative analysis of a cross-sectional area of the optic nerve: a comparison between albino and pigmented rats. Exp Brain Res 54: 266-274.

100. O'connor TM, Houston LL, Samson F (1974) Stability of neuronal microtubules to high pressure in vivo and in vitro. Proc Natl Acad Sci 71: 4198-4202.

101. Balaratnasingam C, Morgan WH, Bass L, Matich G, Cringle SJ, et al. (2007) Axonal transport and cytoskeletal changes in the laminar regions after elevated intraocular pressure. Invest Ophthalmol Vis Sci 48: 3632-3644.

102. Lee MK, Cleverland DW (1996) Neuronal intermediate filaments. Annu Rev Neurosci 19: 187-217.

103. Ruiz-Ederra J, García M, Hicks D, Vecino E (2004) Comparative study of the three neurofilament subunits within pig and human retinal ganglion cells. Mol Vis 10: 83-92.

104. William R, Chalupa L (1983) An analysis of axon caliber within the optic nerve of the cat: Evidence of size groupings and regional organization. J Neurosci 3: 1554-1564.

105. Fitzgibbon T, Reese B (1996) Organization of retinal ganglion cell axons in the optic fiber layer and nerve of fetal ferrets. Vis Neurosci 13: 847-861.

106. Münch M, Kawasaki A (2013) Intrinsically photosensitive retinal ganglion cells: classification, function and clinical implications. Curr Opin Neurobiol 26: 45-51.

107. Kim T-J, Jeon C-J (2006) Morphological classification of parvalbumin-containing retinal ganglion cells in mouse: single-cell injection after immunocytochemistry. Invest Ophthalmol Vis Sci 47: 2757-2764.

108. Fletcher LN, Coimbra JP, Rodger J, Potter IC, Gill HS, et al. (2013) Classification of retinal ganglion cells in the southern hemisphere lamprey Geotria australis (Cyclostomata). J Comp Neurol: In press.

109. Fukuda Y (1977) A three-group classification of rat retinal ganglion cells: histological and physiological studies. Brain Res 119: 327-334.

110. Huang X, Kong W, Zhou Y, Gregori G (2011) Distortion of axonal cytoskeleton: an early sign of glaucomatous damage. Invest Ophthalmol Vis Sci 52: 2879-2888.

111. Knighton RW, Baverez C, Bhattacharya A (1992) The directional reflectance of the retinal nerve fiber layer of the toad. Invest Ophthalmol Vis Sci 33: 2603-2611.

112. Kerker M (1969) The scattering of light and other electromagnetic radiation. Orlando, FL: Academic Press.

113. Bohren CF, Huffman DR (1983) Absorption and Scattering of Light by Small Particles. USA: John Wiley & Sons. Inc.

114. Buckingham BP ID, Lambert W, Oglesby E, Calkins DJ, Steele MR, Vetter ML, Marsh-Armstrong N, Horner PJ (2008) Progressive ganglion cell degeneration precedes neuronal loss in a mouse model of glaucoma. J Neurosci 28: 2735-2744.

115. Kendell KR, Quigley HA, Kerrigan LA, Pease ME, Quigley EN (1995) Primary open-angle glaucoma is not associated with photoreceptor loss. Invest Ophthalmol Vis Sci 36: 200-205.

116. Yu S, Tanabe T, Yoshimura N (2006) A rat model of glaucoma induced by episcleral vein ligation. Exp Eye Res 83: 758-770.

117. Hare WA, Ton H, Ruiz G, Feldmann B, Wijono M, et al. (2001) Characterization of retinal injury using ERG measures obtained with both conventional and multifocal methods in chronic ocular hypertensive primates. Invest Ophthalmol Vis Sci 42: 127-136.

118. Guo L, Moss SE, Alexander RA, Ali RR, Fitzke FW, et al. (2005) Retinal ganglion cell apoptosis in glaucoma is related to intraocular pressure and IOP-induced effects on extracellular matrix. Invest Ophthalmol Vis Sci 46: 175-182.

119. Schmitt JM, Xiang SH, Yung KM (1999) Speckle in optical coherence tomography. J Biomed Opt 4: 95-105.

120. M MN, Tamaki Y, Tomidokoro A, Araie M (2011) In Vivo measurement of blood velocity in human major retinal vessels using the laser speckle method. Invest Ophthalmol Vis Sci 52: 87-92.

121. Qiu J, Li P, Luo W, Wang J, Zhang H, et al. (2010) Spatiotemporal laser speckle contrast analysis for blood flow imaging with maximized speckle contrast. J Biomed Opt 15: 0160031 - 0160035.

122. Briers JD, Fercher AF (1982) Retinal blood-flow visualization by means of laser speckle photography. Invest Ophthalmol Vis Sci 22: 255-259.

123. Briers JD (2001) Laser doppler, speckle and related techniques for blood perfusion mapping and imaging. Physiol Measur 22.

124. Susalka SJ, Pfister KK (2000) Cytoplasmic dynein subunit heterogeneity: implications for axonal transport. J of Neurocyto 29: 819-829.

125. Morgan JE (2004) Circulation and axonal transport in the optic nerve. Eye 18: 1089-1095.

126. Muresan V (2000) One axon, many kinesins: What's the logic? . J of Neurocyto 29: 799-818.

127. Edstrom A HM (1973) Temperature effects on fast axonal transport of proteins in vitro in frog sciatic nerves. Brain Research 58: 345-354.

128. (2012) MatLab Image Processing Toolbox Documentation.

129. (2009) MATLAB and Image Processing Toolbox Release 2009b. Natick, Massachusetts, United States: The MathWorks, Inc.

130. Tang-Schomer MD, Johnson VE, Baas PW, Stewart W, Smith DH (2012) Partial interruption of axonal transport due to microtubule breakage accounts for the formation of periodic varicosities after traumatic axonal injury. Exp Neuro 233: 364-372.

131. Takayama K, Ooto S, Hangai M, Arakawa N, Oshima S, et al. (2012) High-resolution imaging of the retinal nerve fiber layer in normal eyes using adaptive optics scanning laser ophthalmoscopy. PLoS ONE 7: e33158.

132. Kingman S (November, 2004) Glaucoma is second leading cause of blindness globally. Bulletin of the World Health Organization 82 887-888.

133. Resnikoff S, Pascolini D, Etya'ale D, Kocur I, Pararajasegaram R, et al. (Nov. 2004) Global data on visual impairment in the year 2002. Bulletin of the World Health Organization 82: 844-851.